AFRL-AFOSR-VA-TR-2016-0030

Cyber-physical systems to understand the dynamics of nonlinear aeroelastic systems for flexible MAVs and energy harvesting applications

Kenneth Breuer
BROWN UNIVERSITY IN PROVIDENCE IN STATE OF RI AND PROVIDENCE PLANTATIONS

09/28/2015
Final Report

DISTRIBUTION A: Distribution approved for public release.

Air Force Research Laboratory
AF Office Of Scientific Research (AFOSR)/ RTB1
Arlington, Virginia 22203
Air Force Materiel Command

REPORT DOCUMENTATION PAGE	*Form Approved* *OMB No. 0704-0188*

The public reporting burden for this collection of information is estimated to average 1 hour per response, including the time for reviewing instructions, searching existing data sources, gathering and maintaining the data needed, and completing and reviewing the collection of information. Send comments regarding this burden estimate or any other aspect of this collection of information, including suggestions for reducing the burden, to the Department of Defense, Executive Service Directorate (0704-0188). Respondents should be aware that notwithstanding any other provision of law, no person shall be subject to any penalty for failing to comply with a collection of information if it does not display a currently valid OMB control number.

PLEASE DO NOT RETURN YOUR FORM TO THE ABOVE ORGANIZATION.

1. REPORT DATE *(DD-MM-YYYY)* 09-11-2015	**2. REPORT TYPE** Final Report	**3. DATES COVERED** *(From - To)*

4. TITLE AND SUBTITLE Cyber-Physical systems to understand the dynamics of nonlinear aeroelastic systems for flexible MAVs and energy-harvesting applications.	**5a. CONTRACT NUMBER**
	5b. GRANT NUMBER FA9550-12-1-0099
	5c. PROGRAM ELEMENT NUMBER
6. AUTHOR(S) Kenneth S Breuer & Shreyas Mandre	**5d. PROJECT NUMBER**
	5e. TASK NUMBER
	5f. WORK UNIT NUMBER
7. PERFORMING ORGANIZATION NAME(S) AND ADDRESS(ES) Brown University School of Engineering, Box D Providence RI 02912	**8. PERFORMING ORGANIZATION REPORT NUMBER**
9. SPONSORING/MONITORING AGENCY NAME(S) AND ADDRESS(ES) AF Office of Scientific Research 875 North Randolph St., Rm 3112 Arlington, VA 22203	**10. SPONSOR/MONITOR'S ACRONYM(S)**
	11. SPONSOR/MONITOR'S REPORT NUMBER(S)

12. DISTRIBUTION/AVAILABILITY STATEMENT

Approved for public release; distribution is unlimited

13. SUPPLEMENTARY NOTES

14. ABSTRACT

We report on the approach taken and progress made during the three year research program. The goals of the program were to develop parallel experimental and theoretical approaches to study the dynamics of high-amplitude aeroelastic instabilities dominated by unsteady vortex shedding. Current approaches, both experimental and theoretical fall short in their abilities to simulate a wide range of operating conditions and to simulate them in a reasonable time- frame. We demonstrate the successful development of a cyper-physical experimental system, capable of close-to arbitrary definition of the structural characteristics of an aerodynamic structure (stiffness, damping and mass) and demonstrate a complex stability landscape and a complex, but universal vortex formation scaling. We also demonstrate how an asymptotic method based on classical boundary layer theory can be used to develop a feasible numerical model for the rapid simulation of these complex systems.

15. SUBJECT TERMS

Aerodynamics, Vortex Shedding, Fluid-Structure interactions

16. SECURITY CLASSIFICATION OF:			**17. LIMITATION OF ABSTRACT**	**18. NUMBER OF PAGES**	**19a. NAME OF RESPONSIBLE PERSON**
a. REPORT	**b. ABSTRACT**	**c. THIS PAGE**			Kenneth Breuer
unclassified	unclassified	unclassified	UU	56	**19b. TELEPHONE NUMBER** *(Include area code)* 401.863.2870

Reset

DISTRIBUTION A: Distribution approved for public release.

Final Report:
CYBER-PHYSICAL SYSTEMS TO UNDERSTAND THE DYNAMICS OF NONLINEAR AEROELASTIC SYSTEMS FOR FLEXIBLE MAVS AND ENERGY HARVESTING APPLICATIONS.

AFOSR GRANT: FA9550-12-1-0099

Profs. Kenneth Breuer (PI) & Shreyas Mandre
School of Engineering, Brown University, Providence RI 02912

Contact email: kbreuer@brown.edu
Tel: 401.863.2870; Fax: 401.863.9028

Submitted to:

Dr. Douglas Smith,
Dynamical Systems and Control Division: Flow Interactions and Control
AFOSR, Arlington VA.
Tel: (703) 696-6219; DSN 426-6219; FAX (703) 588-1003
E-mail: Flow.Control@afosr.af.mil

Summary

We report on the approach taken and progress made during the three year research program. The goals of the program were to develop parallel experimental and theoretical approaches to study the dynamics of high-amplitude aeroelastic instabilities dominated by unsteady vortex shedding. Current approaches, both experimental and theoretical fall short in their abilities to simulate a wide range of operating conditions and to simulate them in a reasonable time-frame. We demonstrate the successful development of a cyper-physical experimental system, capable of close-to arbitrary definition of the structural characteristics of an aerodynamic structure (stiffness, damping and mass) and demonstrate a complex stability landscape and a complex, but universal vortex formation scaling. We also demonstrate how an asymptotic method based on classical boundary layer theory can be used to develop a feasible numerical model for the rapid simulation of these complex systems.

DISTRIBUTION A: Distribution approved for public release.

Contents

DISTRIBUTION A: Distribution approved for public release.

1 Introduction

Highly flexible aerodynamic systems are ubiquitous in nature and many engineered applications and there is increasing evidence that compliance can confer aerodynamic advantages in stall and unsteady gusts, and can extend system benefits due to the reduced structural weight. Furthermore, with increased interest in highly maneuverable flight vehicles, understanding and modeling the behavior of flexible systems during high angle-of-attack and/or high rate-of-change flight conditions has become a compelling technical priority.

Aeroelastic vibration, or “flutter” has been studied since the dawn of powered flight, and a significant body of research and understanding has been assembled [1–3]. Flutter occurs when aerodynamic forces induce structural motion. In many cases, either aerodynamic or structural damping is sufficient to limit these vibrations. However, in certain situations the damping is insufficient and unstable structural vibrations occur, leading either to a stable finite amplitude limit cycle oscillation (LCO), or unstable failure of the system.

While the theoretical modeling of small aerodynamic perturbations is reasonably well understood, there are several areas that still demand improved understanding, and additional research. These areas include systems in which there is vortex shedding, and hence significant aerodynamical loading from the free wake. In these situations, the modeling of the aerodynamical loads are highly nonlinear, due to the complex evolution of the vorticity in the wake. A second area where considerable research is required is in which the aerodynamic structure has degrees of freedom that are more complex than simple pitch or heave. Examples of this include membrane wings and wings operating with significant motion (such as flapping flight). In all of these cases there are few theoretical frameworks to guide modeling and design.

One of the challenges in developing design tools and dynamical models is that there are not many extensive experimental results with which to compare. While there have been some excellent measurements reported on the behavior of flexible aerodynamic systems (e.g. [4, 5]) and several on unsteady vibrations of flexible MAV wings (e.g. [6]), the drawback of many of these studies that while they can serve as a validation of computational simulations, there are few experiments have been conducted over a wide range of parameters that isolate different physical phenomena, and can be used to develop a fundamental understanding of aerodynamic interactions with flexible structures.

Furthermore, analytical and numerical methods are sorely lacking in their ability to predict vortex growth and formation due to large amplitude structural motions. Simple models such as unsteady Kutta conditions are ad hoc, while full numerical simluations are prohibitively expensive to run over a wide range of parameters. An intermediate, moderate-order quasi-analytical approach is called for to bridge the gap.

1.1 Outline of AFOSR program, and this report

The two demands - for high precision experiments and good-fidelity, moderate cost numerical techniques motived our AFOSR program, and this report outlines the progress made during the past three years. In the next few pages, we outline the technical approach and achievements in both experimental and theoretical domains. We end with an administrative summary describing the various people who worked on this program, and the conference

DISTRIBUTION A: Distribution approved for public release.

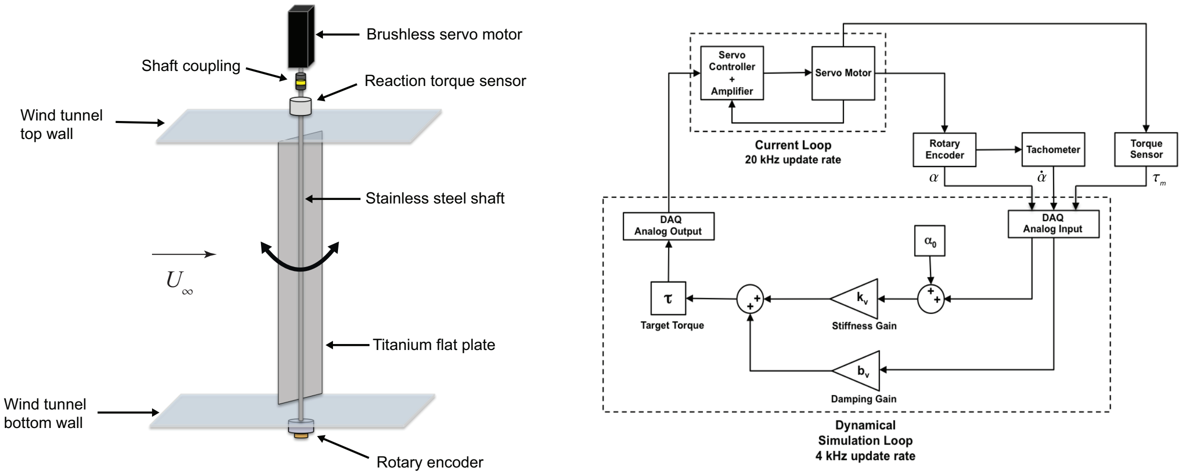

Figure 1: *Schematic of 1-D cyber-physical system (left), along with the control system (right). This system has been successfully employed to explore the dynamics of systems with arbitrary mass, stiffness and damping, including systems with highly nonlinear properties, non-physical properties and to experimentally characterize virtual systems with the correct dynamics of those at a dramatically different physical scale [7].*

papers and presentations that resulted from the AFOSR support. Two archival journal manuscripts (the first in print, the second in review) are attached at the end of the report.

2 Experimental approach and accomplishments

2.1 Cyber-Physical Systems

Despite the interest in these nonlinear aeroelastic systems, extensive study is hard due to (i) the difficulty in matching the relevant non-dimensional parameters in a lab environment, (ii) the expense and complexity of necessary computational simulations whose fidelity is often uncertain, (iii) the time and effort necessary to change the physical system to fine-tune its operation and optimize the objective. An ideal blend that combines experimental and numerical approaches is the use of "cyber-physical" systems - the combination of a physical experiment with a real-time feedback control system which has become technically feasible in recent years. The feedback control system provides a means by which a laboratory-scale experiment can allow for a detailed experiment that mimics the dynamics of a different model (i.e. one with different mass, stiffness or damping), or even a model that obeys a fictitious set of dynamical constraints.

Although cyberphysical systems have been demonstrated for low-speed system operating in water [8, 9], Under the support of this program we designed, constructed, validated and extensively used a Cyberphysical system for use in large amplitude aeroelastic systems operating in air. *This is the first time this has been achieved.* Figure 1 shows a schematic of the experimental configuration used in the current work, illustrating the flat plate mounted to a virtual spring-damper system in the wind tunnel test section.

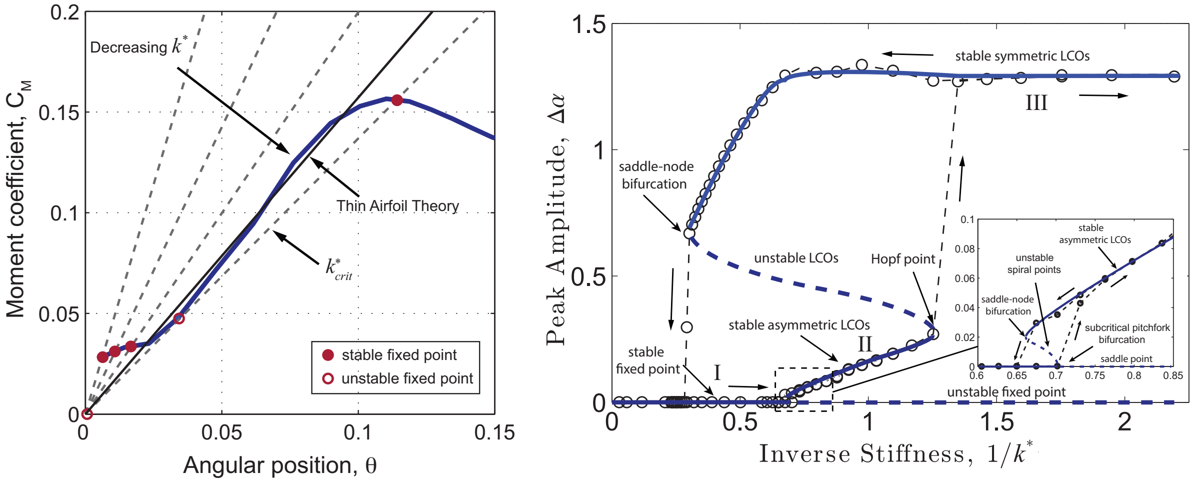

Figure 2: *Coefficient of Moment, C_M as a function of angle of attack (left) and Instability phase map (right). The static coefficient of moment deviates from the linear thin-airfoil solution leading to in intricate series of bifurcations close to the traditional static divergence limit.*

Rather than using a physical torsional spring and damper, the structural stiffness and damping characteristics of the pitching plate are controlled using a cyber-physical system consisting of a servomotor, rotary encoder and torque sensor coupled to a real-time digital control system (Fig. 1). The position, α, velocity, $\dot{\alpha}$, and torque,τ, are multiplied by user-selected stiffness and damping coefficients, k_v and b_v respectively. These are combined with the measured torque and are fed back to the servo motor providing virtual stiffness and damping and inertia, thus simulating arbitrary structural dynamics. The practical benefits of the Cyber-Physical system are chiefly that:

1. The structural dynamics can be modified "on the fly" allowing for rapid and extensive exploration of the structural parameter space. This allows for fast measurements over a wide parameter range.

2. We can change structural and fluid parameters independently, allowing for complete freedom in isolating specific physical phenomena and varying different non-dimensional ratios. For example the non-dimensional stiffness, $k^* = 2k/(\rho U_\infty^2 c^2 h)$, can be kept constant even if the wind speed, U_∞, chord, c, and span, h, are changed. This allows for detailed explorations of Reynolds number effects while keeping structural parameter unchanged.

2.2 Onset of large-amplitude aeroelastic instabilities

The onset of flutter has been well documented [1, 10] and in our work we have detailed the stability boundaries for a real system (i.e. idealized, but still with the full complexities of the physical world), and find a rich and detailed map of the aeroelastic instability. it is well-known that the classic Theordorson static divergence occurs when the restoring stiffness of the torsional spring can no longer contain the aerodynamic torque as the plate pitches up.

However, for the case of a thin flat plate, the aerodynamic coefficient of moment, C_m is not the straight line produced by Thin Airfoil Theory. Rather the $C_M(\alpha)$ curve has some complexity (2b) due to the presence of a small separation bubble at the sharp leading edge, even at very small angles of incidence. As the stiffness reduces, this leads to a rich sub-critical pitchfork bifurcation (at $1/k^* \approx 0.7$) jumping to the familiar low-amplitude limit-cycle-oscillations (LCO) that is familiar from many classical aeroelasticity studies [11–13]. For aerodynamic flight systems, this LCO is to be avoided. However, in our case, we further reduce the stiffness (or, alternatively, increase the inverse stiffness, $1/k^*$), and observe a higher-order Hopf bifurcation, leading to very large amplitude stable limit cycle oscillations, with pitching amplitudes of order ±90°. Complete details of this phase behavior are documented in [7].

2.3 Pitching kinematics and vorticity dynamics

One key achievement during the past three years has been to use the Cyber-Physical system, in concert with high resolution PIV measurements, to understand the large amplitude LCO regime (Region III in Fig. 2). Here, the plate oscillates a a very violent manner: at high frequency ($\mathcal{O}(20)$ Hz) and high amplitude ($\approx \pm 90°$). PIV measurements coupled with the torque-angle phase portrait (Fig 3) help to understand the cycle.

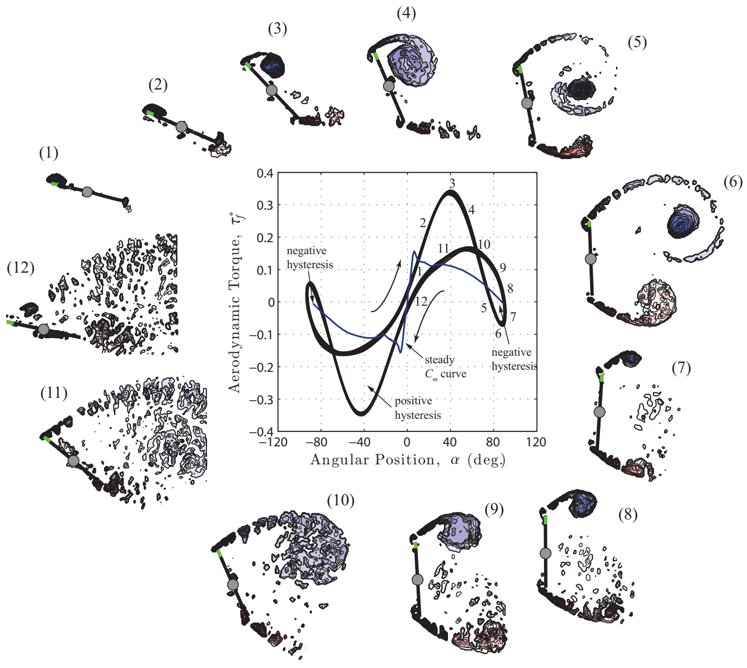

Figure 3: *Dynamics of large-amplitude aeroelastic oscillations. The angle-torque phase portrait is shown in the center illustrating a characteristic oscillation cycle. Each phase of the cycle has a corresponding phase-averaged swirl field, illustrating the growth and detachment of the leading- and trailing-edge vortices.*

As the plate begins to rise from its equilibrium position (figure 3: (1)), the aerodynamic torque increases. The torque is *lower* than that predicted by the steady moment coefficient curve [7] due to the presence of dynamically-generated vortex, located on the lower side of the plate, that has survived from the previous cycle, and is resisting the positive rotation of the plate. As the angle of attack increases, the aerodynamic torque continues to grow well beyond the static stall angle finally reaching a maximum value nearly 2.5 times greater than its static counterpart (figure 3: (1)–(3)). This is a classic example of "dynamic stall" wherein the force and torque on the plate is significantly augmented by the formation and growth of a strong LEV on the suction side of the plate, [14]. The LEV core continues to grow in size and strength as it entrains circulation of the small eddies generated at the leading edge. At the same time, a train of opposite-signed vortices is continuously shed from the trailing edge. The formation of these discrete eddies has been commonly attributed to a Kelvin-Helmholtz-like instability inherent in the separated shear layer by numerous investigators [15, 16]. The velocity shear arising from the high velocity of the impinging flow and the relatively low velocity of the separated free shear layer at the sharp-edges promotes instability in the shear layer, and therefore leads to the generation of the small-scale eddies. Moreover, the shedding frequency associated with the small eddies is much higher than that of the primary vortices which is comparable with the pitching frequency.

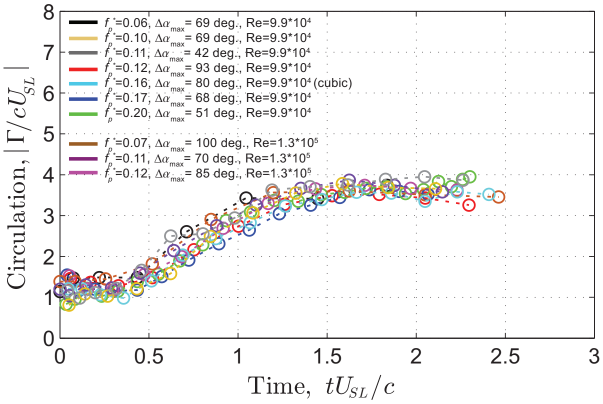

Figure 4: *Universal scaling of the vortex dynamics is achieved using the local shear layer velocity rather than the free stream. Note that the circulation grows at a universal rate, and reaches a saturated stage, consistent with a vortex formation time of approximately 4.*

The aerodynamic torque attains a maximum at $\alpha \approx 40°$ after which it immediately begins a precipitous decrease (figure 3-(4)). This torque decrement is not due to vortex leaving the plate, given that the attached LEV is evident at $\alpha \approx 62°$ (figure 3: (5)). Rather, we hypothesize that the saturation of the LEV circulation, and the movement of the vortex core closer to the mid-chord point are responsible for the decrease in the aerodynamic torque. Despite this sharp drop in the aerodynamic torque, the plate continues to rotate (due to its inertia) until it comes to rest at a maximum pitch angle, in this particular, case, approximately 90 degrees to the free stream direction. The shear-layer from the trailing edge begins to roll up and forms a trailing-edge vortex (TEV) (figure 3: (6)–(7)). This roll-up of the shear layer is presumably due to a global instability of the wake which includes the influence of the LEV passing just overhead. Upon reaching a maximum angle of rotation, we observe a second increase in the aerodynamic torque owing to the development of a secondary vortex in the close proximity of the leading edge (figure 3: (8)–(10)). This secondary vortex is analogous to that observed by [17], who examined the LEV formation on a flat plate undergoing a translating motion perpendicular to the incoming flow.

2.4 Circulation growth and Reynolds number scaling

During the pitch reversal, a region of negative hysteresis is observed due to the fact that the plate's return motion is hampered by the counter torque induced by the secondary vortex. For applications interested in energy harvesting, the negative hysteresis implies that the energy is being transferred from the system into the wake. and represents a drop in harvesting efficiency. We also note that the secondary TEV develops as the shear layer emanating from the trailing edge curls up in the wake. Finally, the elastic restoring toque of the torsional spring pulls the plate back to its equilibrium angle of attack (figure 3:

DISTRIBUTION A: Distribution approved for public release.

(11)–(13)). Even at very small angle, the flow over the pressure side of the plate does not completely reattach. This in turn hampers the growth of the aerodynamic torque at the beginning of the second-half of the cycle, resulting in a smaller torque value relative to the quasi-steady prediction. By symmetry, the pattern repeats during the second-half of the cycle.

From the PIV measurements we can calculate the Leading Edge Vortex (LEV) growth and position. Figure 4 shows the growth of the circulation contained in the LEV, measured over a wide variety of pitching amplitudes, pitch rates (controlled by varying the stiffness and damping of the structure) and Reynolds numbers (controlled via the chord and free stream velocity). The non-dimensionalization is obtained using the *feeding velocity* of the shear layer [18]:

$$U_{SL} = 2\pi f c/2 + U_\infty \sin(\alpha(t)).$$

which takes into account not only the local free stream, but also the speed and direction of the leading edge. The data collapse is impressive, suggesting that this feeding velocity is the appropriate scaling parameter. However, the movement of the vortex, and its position with respect to the lifting surface is critical in determining the lift, drag and pitching moment associated with the LEV. Again the cyberphysical system's ability to explore a wide parameter space indicates that the pitching moment is independent of pitch rate (Fig 4b).

2.5 Implications for energy harvesting

The ability to effectively harvest energy from the free stream using this system is limited due to its single degree of freedom. The mechanical energy harvested by the pitching plate is simply the area enclosed by the torque-angle phase portrait (Fig. 3), and this is easily found from the experimental data. Note that there is an area of positive energy capture, as the plate is pulled up by the LEV, but there is also a region of negative hysteresis associated with the development of a second LEV that resists the return of the plate to zero incidence angle. The Cyber-Physical control can be used to eliminate this region of inefficiency by optimizing the nonlinear stiffness of the system so that the plate snaps back more quickly at high incidence angles. Optimizing the nonlinearity yields a second torque-angle trace (Fig 5) which eliminates the region of negative hysteresis and improves the power coefficient by 54% over the baseline condition.

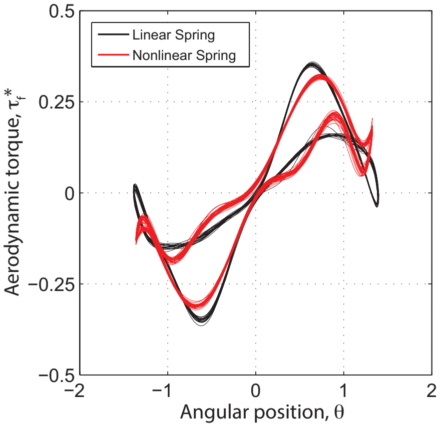

Figure 5: *Aerodynamic torque versus angular position phase portrait for linear (black) and cubic (red) springs. Re=9.9·10⁴. The nonlinear spring eliminates the negative hysteresis region and increases the cycle frequency, resulting in a 54% increase in the power coefficent, C_P.*

Energy harvesting using only pitching dynamics is destined to be inefficient, and several groups have proposed systems that include both pitching and heaving kinematics as efficient mechanisms for energy harvesting (e.g. [19–22]). Key to the success of these techniques is the ability to form and grow an LEV which gives additional lifting force to the foil, and to shed it from the foil at the optimal moment.

DISTRIBUTION A: Distribution approved for public release.

All of the schemes proposed by other groups have defined the kinematics and measured the energy harvesting efficiency. The example given here illustrates how we can achieve optimal performance *passively* using just the one degree of freedom, but the concept applies equally well to systems with both pitch and heave motions and a key advantage of the cyberphysical system is the prospect of designing a purely passive structural system that has optimal energy harvesting characteristics - this will be a focus of the next phase of research.

3 Theoretical approach and accomplishments

This section outlines and summarizes the mathematical modeling approach we pursued to develop a framework, which is extensible beyond the particular phenomenon of interest. Our model uses an approximation of the Navier-Stokes equations inspired by matched asymptotic methods to derive a reduced order model. Because of the high Reynolds number of the flow, the viscous terms in the Navier-Stokes equations may be ignored away from solid walls. Near the solid walls, where the no-slip boundary condition is imposed, the viscous effects may not be ignored – these effects define a thin region where Prandtl's boundary layer approximation is possible Matching of the flow variables between the two approximations naturally implies a vorticity flux shed from the boundary layer. We found the approach effective. However, the flow that develops in the boundary layer is not described adequately by Prandtl's boundary layer equations; even moderately high curvatures cause the approximation to fail. We hypothesize a simple fix for the boundary layer approximation.

This approach was motivated by our attempt to use fluid dynamical models for the control and optimization of cyber-physical systems. Such models must satisfy the opposing requirements of retaining the complexity of flow, while eliminating the unnecessary details for rapid computation. We found no existing frameworks suitable of this task.

Numerically solving the governing Navier-Stokes equations using primitive variables is prohibitively expensive from the perspective of flow optimization and control. The primary expense arises from resolving the boundary layer; its thickness dictates the number of grid points to be used for spatial discretization, and the time step through the CFL condition. On modern desktop computers one flow solution in 2D takes at least hours, and in 3D takes at least days. Calculating the adjoint variables and implementing a gradient based optimization algorithm [23] increases the computational time to at least months for 2D problems (years for 3D). Methods like Large Eddy Simulations model sub-grid scale eddies, but still have to resolve the boundary layer to accurately predict the shed vorticity, and hence are not exempt from this estimate. Parallel computing on a cluster of processors can reduce the 2D computational time to few days and modern supercomputers may be able to reduce the computational time for 3D to several hours, if the algorithms are effectively parallelized, but it is uncertain how data dependencies can be addressed for parallelization. In conclusion, optimization, state estimation, and control are still out of range of computational fluid dynamics.

An hierarchy of reduced order models of fluid flow provide an alternative to avoid the computational effort for the solution of Navier-Stokes equations, at the expense of reduced (or sometimes uncertain) accuracy. All these models identify that viscous effects in the flow may be neglected except for the process of vorticity shedding from the body. The simplest of these models [24–29] apply to rigid wings. The recent advances on developing the leading edge separation parameter [30] also belong to this category. They assume the flow around the wings to be quasi-steady and model the fluid dynamic force on them in terms of the instantaneous orientation, velocity and acceleration of the wing. Versions of such models that incorporate unsteadiness [31, 32] are also available. The assumptions underlying these models make them unsuitable for large amplitude unsteady motion, where the flow can separate from multiple points on the body.

Models in the next level of the hierarchy also only apply to bodies with sharp edges, but model vorticity transport according to inviscid dynamics [33–40]. These models assume that vorticity is shed only from the sharp edges of the body and then evolves into a vortex sheet. The rate of the vorticity shed is chosen so as to eliminate a singularity of the flow at these sharp edges – the celebrated Kutta condition from aerodynamics. The shed vortex sheet is usually represented by an array of discrete point vortices obeying inviscid vortex dynamics or a single tightly rolled-up point vortex (governed by the Brown-Michael vortex dynamics). These methods are also very efficient. However, they do not allow for the possibility of separation at any point other than one of the sharp edges on the body. As a result, they cannot be used to model vorticity shed from a smooth body (e.g. an elliptical wing). Moreover, in practice, vorticity is not always shed from *all* sharp edges on a body, for example, the flow may not always separate from the leading edge of a wing. These methods cannot *a priori* predict the edges at which the flow separates. Because the optimal flows are suspected to correspond to a precise control of the instance vorticity shedding switches on or off from one of the edges, or of shedding from another point on the surface of body, these models appear to mis-represent or eliminate the effects underlying the enhanced unsteady performance.

The most accurate and computationally intensive methods in the hierarchy account for the vorticity in the boundary layer as vortex sheets of variable strength at or near the surface of the body. The vortex sheets are represented as arrays of point or blob vortices and function to enforce the no-slip condition [35, 41–48]. These vortices transport away from the boundary by advection and diffusion, and leave the boundary layer where the flow separates, thus accurately modeling vorticity shedding. The drawback of this method is that accurate description of flow requires computational effort comparable to direct solution of Navier-Stokes equations. It is so because the distance between the point or blob vortices should be comparable to a fraction of the boundary layer thickness, and plays a role analogous to grid spacing in direct solution of Navier-Stokes equations. These methods are not reduced order models in the strict sense, because they apply for all Re and do not take advantage of the large Re of the flow.

3.1 Our mathematical model

Following the usual procedure for matched asymptotic methods, the flow domain is decomposed into a boundary layer of thickness $\mathrm{Re}^{-1/2}$ close to the solid body, where viscous effects are important, and an outer region where they are negligible (see figure 6(a)). The separation of length scales in the boundary layer leads Prandtl's boundary layer equation, which accounts for generation and transport of vorticity in the boundary layer. As this vorticity flows out of the boundary layer, the method converts it to an array of point vortices as a

DISTRIBUTION A: Distribution approved for public release.

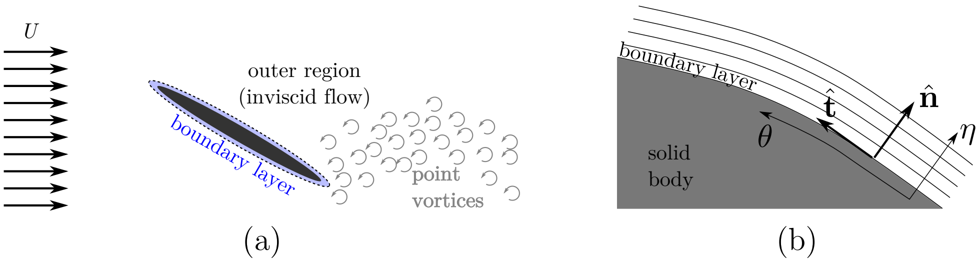

Figure 6: *Schematic showing domain decomposition into an outer region and a boundary layer. (a) The flow in the outer region is described in terms of point vortices. (b) The boundary layer coordinate systems.*

way of matching the velocity in the boundary layer with the outer flow. The point vortices re-entering the boundary layer imparts momentum to the fluid there, thus accounting for re-attachment. The solution automatically accounts for unsteady boundary layer separation, and thereby captures the details of mechanisms such as dynamic stall, leading edge vortex shedding, and vortex recapture. The method has a fixed computational cost as a function of Reynolds number, presented in subsection 3.1.4. This model was formulated in 2013.

3.1.1 Outer flow:

The state of the flow at time step n in the outer region is described using an array of point vortices of strength Γ_j at location $\boldsymbol{r}_j$, $j = 1, 2, 3, \ldots, N^n$, where N^n is the number of vortices at that time step. These vortices obey inviscid dynamics, and are introduced or removed as required to match with the dynamics in the boundary layer. The fluid velocity induced by these vortices at this time step is given by

$$\boldsymbol{u}_I^n(\boldsymbol{x}) = \sum_{j=1}^{N^n} \frac{\Gamma_j \hat{\boldsymbol{z}} \times (\boldsymbol{x} - \boldsymbol{r}_j^n)}{2\pi|\boldsymbol{x} - \boldsymbol{r}_j^n|^2}. \tag{1}$$

The total fluid velocity field is $\boldsymbol{u}_{\text{out}}^n(\boldsymbol{x}) = \boldsymbol{u}_I^n(\boldsymbol{x}) + \boldsymbol{\nabla}\phi^n(\boldsymbol{x})$, where the velocity potential ϕ^n satisfying $\nabla^2\phi^n = 0$, is added to satisfy far-field boundary conditions and matching with the boundary layer. The total velocity obeys the (discretized form of) Euler equations for inviscid fluids

$$\boldsymbol{u}_{\text{out}}^{n+1} = \boldsymbol{u}_{\text{out}}^n - \Delta t \left\{\boldsymbol{u}_{\text{out}}^n \cdot \boldsymbol{\nabla}\boldsymbol{u}_{\text{out}}^n + \boldsymbol{\nabla}p^{n+1}\right\} = \boldsymbol{u}_{\text{out}}^n - \Delta t \left\{\boldsymbol{u}_{\text{out}}^n \times \omega\hat{\boldsymbol{z}} + \boldsymbol{\nabla}\left[p^{n+1} + \frac{|\boldsymbol{u}_{\text{out}}^n|^2}{2}\right]\right\}, \tag{2}$$

in terms of the vorticity $\omega = \hat{\boldsymbol{z}} \cdot \boldsymbol{\nabla} \times \boldsymbol{u}^n$, where the gradient of pressure p^{n+1} imposes incompressibility. From (2), momentum transport [49] is seen to arise from the $\boldsymbol{u}_{\text{out}}^n \times \omega\hat{\boldsymbol{z}}$ term, along with the gradient of the Bernoulli term. The term $\boldsymbol{u}_{\text{out}}^n \times \omega\hat{\boldsymbol{z}}$ is related to the flux of vorticity, a fact used in the matching procedure.

DISTRIBUTION A: Distribution approved for public release.

3.1.2 Boundary layer:

The flow in the boundary layer is described using a body fitted coordinate system. The arc-length coordinate along the boundary layer is denoted θ and the wall normal coordinate translating normally with the body is η with the position vector $\boldsymbol{x}(\theta, \eta)$, as shown in figure 6(b). The solid body moves with velocity $\boldsymbol{u}_0(\theta) = u_0^n(\theta)\hat{\boldsymbol{t}}^n(\theta) + v_0^n(\theta)\hat{\boldsymbol{n}}^n(\theta)$, where $\hat{\boldsymbol{t}}^n$ and $\hat{\boldsymbol{n}}^n$ are unit basis vectors in the tangential and normal directions at time step n respectively. The functions u_0^n and v_0^n describe the motion of the body, which may themselves be prescribed or governed by the dynamics of the solid body. The computational method for calculating flow around rigidly moving bodies is described here; the generalization to flexible bodies needs to account for boundary layer coordinates that stretch; this detail poses no technical difficulty [50–52]. The fluid velocity $\boldsymbol{u}_{\text{bl}}$ is described by decomposing along the tangential and normal direction at time step n as $\boldsymbol{u}_{\text{bl}}^n(\theta, \eta) = u^n(\theta, \eta)\hat{\boldsymbol{t}}(\theta) + v^n(\theta, \eta)\hat{\boldsymbol{n}}(\theta)$. The radius of curvature of the boundary is assumed to be much larger than the boundary layer thickness, which leads to the simplified governing equations (the effect of leading order body curvature may be included without much difficulty in this formulation)

$$u_t + uu_\theta + vu_\eta + p_\theta = \nu u_{\eta\eta}, \quad p_\eta = 0, \quad u_\theta + v_\eta = 0, \tag{3}$$

where $\nu = \mathrm{Re}^{-1}$, and subscripts denote partial derivatives. The velocity components satisfy $u = u_0$ and $v = 0$ at the solid wall $\eta = 0$. Asymptotic matching with the outer region is imposed as $\eta \to \infty$. Matching of normal stress implies that pressure in the boundary layer is equal to the pressure in the outer region, whereas tangential stress leads to the shedding of vorticity as shown in §3.1.3. Vorticity $\omega = u_\eta^n - v_\theta^n$ in the boundary layer is approximated as $\omega \approx u_\eta$ and its flux in the normal direction is $v\omega - \nu\omega_\eta \approx vu_\eta - \nu u_{\eta\eta}$. A natural boundary condition to use is that the diffusive flux of vorticity be zero so that matching with the outer inviscid flow is possible, i.e. $u_{\eta\eta} = 0$ at $\eta = \eta_{\max}$.

The boundary layer equation is discretized in time as

$$u^{n+1} - u^n + \Delta t\left(u^n u_\theta^n + v^n u_\eta^n + p_\theta^{n+1} - \nu u_{\eta\eta}^{n+1}\right) = 0, \quad p_\eta^{n+1} = 0, \quad u_\theta^{n+1} + v_\eta^{n+1} = 0. \tag{4}$$

The viscous term being the stiffest term is treated implicitly for stability, and the implicit treatment of the pressure term is related to the outer pressure p^{n+1}. The advection terms are discretized spatially using upwind differences and the viscous term is treated using central difference; the precise form of this discretization is chosen so that matching is carried out to numerical precision.

3.1.3 Matching:

Assuming that the two flows agree exactly at the interface (between the outer region and the boundary layer) at time step n, i.e. $\boldsymbol{u}_{\text{out}}^n(\boldsymbol{x}(\theta, \eta_{\max})) = \boldsymbol{u}_{\text{bl}}^n(\theta, \eta_{\max}) = u^n\hat{\boldsymbol{t}} + v^n\hat{\boldsymbol{n}}$, the exact numerical matching at time step $n+1$ requires careful analysis of the corresponding terms in the equations governing the flow in both regions. The main difficulty is the consistent determination of the unknown pressure p^{n+1} to substitute in (4), because it depends on the outer velocity $n+1$, which in turn depends on the normal velocity in the boundary layer. However, this difficulty is solvable using a operator splitting technique presented in table 1.

DISTRIBUTION A: Distribution approved for public release.

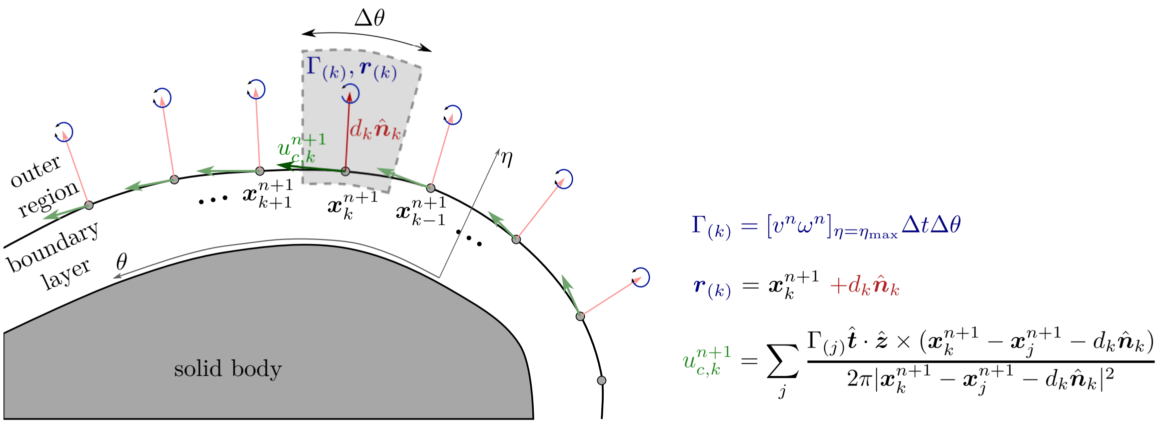

Figure 7: *A schematic describing the vortex shedding method in step 9 of table 1. The vorticity flowing out of the boundary layer at point $\boldsymbol{x}_k$ with flux $v\omega$ in time Δt through each element is converted to a point vortex of strength $\Gamma_{(k)}$ (top equation). These point vortices are placed along a curve just outside the boundary layer to simulate a vortex sheet shed from the boundary layer. The position of these point vortices $\boldsymbol{r}_{(k)}$ is determined by the distance d_k outside the boundary layer (middle equation). The distances d_k are chosen so that these vortices induce tangential velocity exactly equal to the change in the boundary layer velocity component u_c^{n+1} resulting from vorticity transport to the outer region (step 7 in table 1).*

Using this technique, the time stepping results in a numerically exact agreement between the outer and inner flow, and can be implemented using efficient computational techniques.

The outer velocity at time step $n+1$ is split as $\boldsymbol{u}_{\text{out}}^{n+1} = \tilde{\boldsymbol{u}}_I^{n+1} + \tilde{\boldsymbol{u}}_{\text{new}}^{n+1} + \boldsymbol{\nabla}\phi^{n+1}$, where $\tilde{\boldsymbol{u}}_I^{n+1}$ is the velocity induced by the N^n vortices from time step n (now moved to their new location), $\tilde{\boldsymbol{u}}_{\text{new}}^{n+1}$ is the velocity induced by the new vortices, and $\boldsymbol{\nabla}\phi^{n+1}$ is the potential flow part.

The unknown tangential boundary layer velocity at time step $n+1$ is also decomposed as $u^{n+1} = u_a^{n+1} + u_b^{n+1} + u_c^{n+1} + q(\theta)\, u_h^{n+1}$, with each part playing a specific role in matching.

Matching works by requiring that each part of the outer and boundary layer (see steps 2-9 coded by backgound color in table 1) velocity decomposition satisfy an update equation so that (i) the sum of these update equations gives (2) and (4) respectively, and (ii) at the matching interface each part of outer flow matches with a part of the boundary layer (see equations in steps 4, 6, 8, 9 and 12 in table 1 coded by background color). For complete details see table 1.

3.1.4 Computational complexity:

The computational effort for our method is significantly lower than direct numerical solution of Navier-Stokes equations, because only the boundary layer region needs to be discretized. The number of grid points in the boundary layer region is independent of Re because both the boundary layer thickness and grid spacing scale as $\text{Re}^{-1/2}$. The number of vortices shed per time step is a small fraction of grid points in the tangential direction because vorticity is shed only close to the outflow stagnation point. Most of the computational steps are broken down into computations that take either $O(N)$ or $O(N \log N)$ effort. Moreover, many procedures

DISTRIBUTION A: Distribution approved for public release.

in the time-stepping are embarrassingly parallelizable so that extension to multiprocessor, multicore, or graphical processor unit architectures should be beneficial.

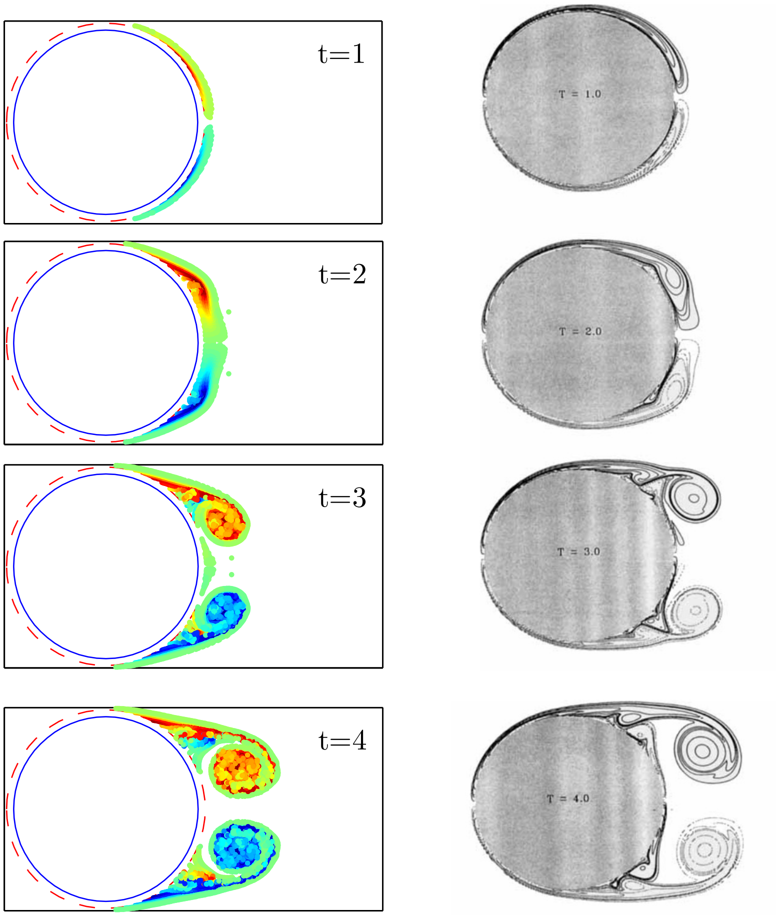

Figure 8: *Vorticity shed in an impulsively started flow around a cylinder at* $Re = 3000$. *(Left) The boundary layer equations* (3) *are solved in a region of thickness* $5Re^{-1/2}$ *around the cylinder, shown by the region between the red dashed line and the blue solid line. The point vortices shed from the boundary layer are color coded according to strength. The convective scale is used to non-dimensionalize time. (Right) Comparison with vorticity contour computed by Koumoutsakos and Leonard [53] (figure 21 therein). These results were presented in 2015.*

3.2 Test cases

To test the method, we applied it to impulsively started flow past a static and rotating cylinders, and stationary ellipses at an angle of attack to the impinging flow.

3.2.1 Impulsively started cylinder past a stationary cylinder:

A cylinder of unit radius is subject to a flow, which starts at $t = 0$ from zero to a unit uniform farfield velocity with $\mathrm{Re} = 3000$. The resulting flow is depicted in figure 8. We have verified that our results match the asymptotic [54] skin-friction and form drag for small t, and the drag coefficient and vorticity profiles [53] for large t. The vorticity field is compared with the the results of Koumoutsakos and Leonard [53] in figure 8. The flow and the force on the cylinder matches results obtained from CFD at a fraction of the computational expense.

DISTRIBUTION A: Distribution approved for public release.

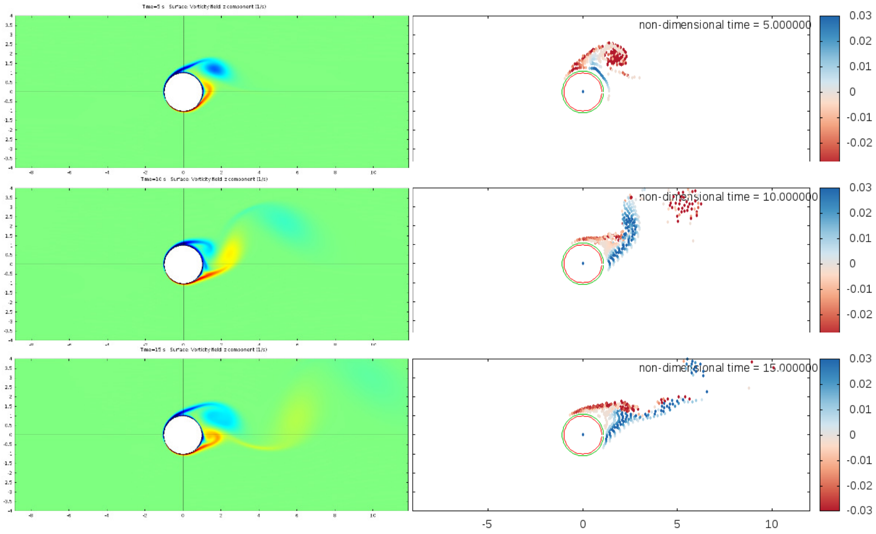

Figure 9: *Snapshots of shed vorticity using CFD (left) and shed point vortices using our method (right) for an impulsively started uniform flow past a rotating cylinder for a dimensionless rotation rate of* 2 *with* $Re = 1000$. *The snapshots agree qualitatively, but quantitative discrepancies in the patterns formed by the vorticity are clearly visible.*

3.2.2 Impulsively started flow past ellipses at angle of attack and rotating cylinders:

While the impulsively started flow past a stationary cylinder agreed well with direct numerical solution of the Navier-Stokes equations, the agreement is due to a special condition satisfied in this case but not shared by many other common cases of interest. The impulsively started flow past ellipses oriented at an angle of attack and rotating cylinders represent cases which show disagreement between results of our model and flow computed using direct solution of Navier-Stokes. We systematically investigate the source of the disagreement and determine the modification to Prandtl's boundary layer required for minimizing it.

First consider an impulsively started flow past a rotating cylinder. The flow computed using CFD agrees well with the flow computed using our model for slow rotation rates. However, for faster rotation rates, the results from our model disagree with the direct numerical solution of Navier-Stokes. Figure 9 shows snapshots of vorticity computed using CFD and distribution of point vortices computed using our model for Re = 1000 and a rotation rate of 2, which shows a case on the verge of this disagreement.

Since the only possible inaccurate component of the model is the boundary layer approximation (the vortex dynamics accurately represent Navier-Stokes equations in the region where viscosity is negligible), the only possible cause for the disagreement is the boundary layer approximation. We have separately verified from the early evolution of the flow, when the outer region is irrotational and therefore devoid of vorticity, that the evaluation of potential flow in the outer region forced by the boundary layer dynamics is accurate. Therefore, the only remaining possibility of the boundary layer approximation being inaccurate must be true.

A careful inspection of the boundary layer approximation, coupled with numerical experiments examining the failure of our model allows us to improve upon the boundary layer

DISTRIBUTION A: Distribution approved for public release.

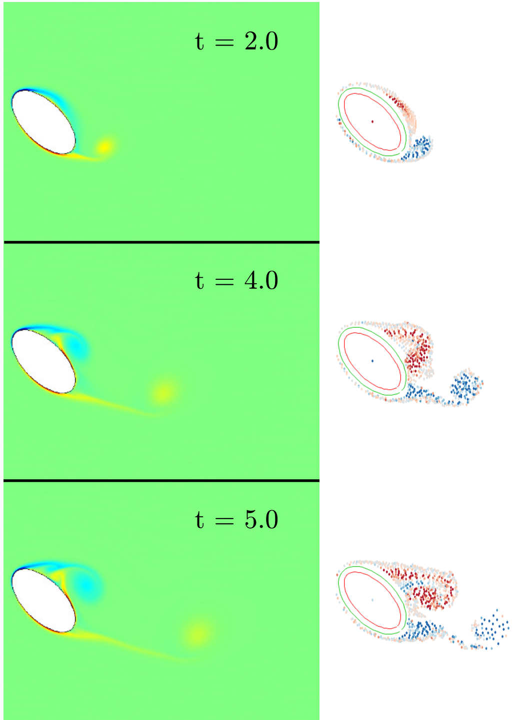

Figure 10: *Snapshots of vorticity field computed using CFD (left) and point vortex distribution computed using our model for impulsively started flow past an ellipse.*

approximation. Within the boundary layer approximation, the separation of length scale holds, and so does the neglect of the axial viscous stress term and the dominance of the tangential over normal velocity component. The least accurate approximation is the neglect of the pressure variation along the thickness of the boundary layer; the contribution of the centripetal acceleration to the normal pressure gradient may lead to noticeable errors. Thus we propose to modify the normal momentum balance equation the boundary layer approximation as

$$u_t + uu_\theta + vu_\eta + p_\theta = \nu u_{\eta\eta}, \quad p_\eta = u^2\kappa, \quad u_\theta + v_\eta = 0. \tag{5}$$

As an example consider the flow around an ellipse of aspect ratio ϵ at an angle of attack to the impinging flow. The maximum curvature on the ellipse surface scales as $1/\epsilon$ along the major axis, where the maximum velocity of $\mathrm{O}(1/\epsilon^{1/2})$. The magnitude of the normal pressure gradient scales as $1/\epsilon^2$, and therefore the difference in pressure across the boundary layer thickness scales as $O(\epsilon^{-2}\mathrm{Re}^{-1/2})$. Thus an aspect ratio as much as $\mathrm{Re}^{1/4}$ can violate the boundary layer approximation.

To test this hypothesis, we implemented our model for the case of an impulsively started ellipse. The point vortex distribution computed using our model with the boundary layer approximated by (3), is shown in figure 10, and is compared with results obtained from CFD. We have not yet implemented the modified boundary layer model (5), but comparison of flows computed using (3) and (5) provides a systematic way of comparing the effectiveness of our hypothesis. With this modification, the method retains the sparse structure of the model that facilitates rapid computation.

4 Summary of accomplishments

Understanding and optimizing coupled fluid-structure systems for different applications is challenging. Experiments capture the real physics, but are not easily employed over a wide range of scales, speeds, stiffness and damping. Computational efforts can "dial in" arbitrary parameter ranges, but are time-consuming and often don't capture realistic physics, often due to Re-effects. The key accomplishments achieved during the past three years of AFOSR funding are:

Implementation of Cyber-Physical system. We have implemented the Cyber-Physical system in air (previous implementations have been in water) operating at high frequency and with high accuracy. The dynamics of the system are well-characterized and robust.

Identification of Instability boundaries. The phase map delineating stable behavior as well as low- and high-amplitude limit cycle oscillations (LCOs) has been mapped out and carefully characterized.

Physics of high amplitude oscillations. The high-amplitude LCO regime has been carefully measured and each phase associated with the formation, growth and detachment of the leading edge vortex associated with the separation at the sharp leading edge.

Leading edge vortex growth and scaling. The dynamics of vortex growth have been characterized and scaled over a wide range of pitching behavior and a moderate range of Reynolds numbers. Although this is not complete, a consistent description has been identified, but still needs to be rigorously validated.

Development of new model for high-Re flows. Our model uses an approximation of the Navier-Stokes equations inspired by matched asymptotic methods to derive a reduced order model. Because of the high Reynolds number of the flow, the flow is assumed inviscid away from the walls, but near the walls, where the no-slip boundary condition is imposed, the viscous effects give rise to a thin boundary layer. Matching of the flow variables between the two approximations naturally implies a vorticity flux shed from the boundary layer.

4.1 Remaining questions and future work

Despite these successes, several questions remain, and the Cyber-Physical approach provides a unique opportunity to explore a wide range of unsteady aerodynamics and vortex-structure interactions. The key research questions that we identify are:

Scaling. the Cyber-Physical system allows us to separate structural and fluid parameters with unprecedented flexibility (for an experimental system). Some indications on scaling have been identified, but more needs to be done. What are the relevant roles of pitching amplitude, rate and acceleration as well as Reynolds number, and structural inertia?

DISTRIBUTION A: Distribution approved for public release.

Three-dimensional effects Current experiments have been deliberately restricted to two-dimensional phenomena that emphasize the LEV. What is the role of three-dimensional effects, particularly spanwise flows that are present in swept, rotating and flapping wings?

Energy harvesting. How can a passive structural characteristics be used to replace proscribed kinematic motion, and how can we optimize the vortex dynamics for energy capture.

Model development. The flow that develops in the boundary layer is not described adequately by Prandtl's boundary layer equations; even moderately high curvatures cause the approximation to fail. We hypothesize a simple modification for the boundary layer approximation by taking into account the component of centripetal acceleration in the normal direction, which can be implemented at minimum additional computational expense.

DISTRIBUTION A: Distribution approved for public release.

Outer velocity: $\boldsymbol{u}_{\text{out}}^{n+1} = \tilde{\boldsymbol{u}}_I^{n+1} + \tilde{\boldsymbol{u}}_{\text{new}}^{n+1} + \boldsymbol{\nabla}\phi^{n+1}$, $\quad p^{n+1} = p_1 + p_2$

1. Advect vortices ($k = 1, 2, \ldots, N^n$) according to

$$\boldsymbol{r}_k^{n+1} = \boldsymbol{r}_k^n + \Delta t \left[\boldsymbol{\nabla}\phi^n(\boldsymbol{r}_k^n) + \textstyle\sum_{j=1, j\neq k}^{N^n} \dfrac{\Gamma_j \hat{\boldsymbol{z}} \times (\boldsymbol{r}_k^n - \boldsymbol{r}_j^n)}{2\pi|\boldsymbol{r}_k^n - \boldsymbol{r}_j^n|^2} \right]$$

2. Define components of $\tilde{\boldsymbol{u}}_I^{n+1}$ at $\boldsymbol{x}$ on the interface:

$$\tilde{\boldsymbol{u}}_I^{n+1} = \textstyle\sum_{j=1}^{N^n} \dfrac{\Gamma_j \hat{\boldsymbol{z}} \times (\boldsymbol{x} - \boldsymbol{r}_j^{n+1})}{2\pi|\boldsymbol{x} - \boldsymbol{r}_j^{n+1}|^2} \quad \equiv \quad \tilde{u}_I^{n+1}\hat{\boldsymbol{t}} + \tilde{v}_I^{n+1}\hat{\boldsymbol{n}}$$

3. Calculate p_1 at the interface:

$$\frac{\tilde{u}_I^{n+1} - (u^n - \phi_\theta^n)}{\Delta t} + u^n u_\theta^n + v^n v_\theta^n + p_{1,\theta} = 0.$$

5. Define $\dfrac{\phi_\theta^{n+1} - \phi_\theta^n}{\Delta t} + p_{2,\theta} = 0$. p_2 and ϕ^{n+1} solved in step 12.

9. Introduce new vortices outside the boundary layer to match the shed vorticity and $\tilde{\boldsymbol{u}}_{\text{new}}^{n+1} \cdot \hat{\boldsymbol{t}} = u_c^{n+1}$ from this shed vorticity. See figure 3 for details. Formally, $\tilde{\boldsymbol{u}}_{\text{new}}^{n+1}/\Delta t + \boldsymbol{u} \times \omega\hat{\boldsymbol{z}} = 0$.

11. Calculate the total normal velocity component in terms of ϕ^{n+1}:

$$\boldsymbol{u}_{\text{out}}^{n+1} \cdot \hat{\boldsymbol{n}} = \phi_\eta^{n+1} + (\tilde{\boldsymbol{u}}_I^{n+1} + \tilde{\boldsymbol{u}}_{\text{new}}^{n+1}) \cdot \hat{\boldsymbol{n}}.$$

12. Solve $\nabla^2\phi^{n+1} = 0$ satisfying boundary condition that the normal velocities calculated in steps 10 and 11 match exactly, i.e. $\boldsymbol{u}_{\text{out}}^{n+1} \cdot \hat{\boldsymbol{n}} = v_0^{n+1} + v^{n+1}$. Update p_2 and u_b^{n+1} using ϕ^{n+1}.

Adding steps 3, 5 and 9 gives the tangential component of

$$\frac{\boldsymbol{u}_{\text{out}}^{n+1} - \boldsymbol{u}_{\text{out}}^n}{\Delta t} + \boldsymbol{u}^n \times \omega\hat{\boldsymbol{z}} + \boldsymbol{\nabla}\left(p^{n+1} + \frac{|\boldsymbol{u}_{\text{out}}^n|^2}{2}\right) = 0.$$

Boundary layer velocity: $u^{n+1} = u_a^{n+1} + u_b^{n+1} + u_c^{n+1} + q(\theta)\, u_h^{n+1}$

4. Compute u_a^{n+1} satisfying ($\omega^n = u_\eta^n - v_\theta^n$)

$$\frac{u_a^{n+1} - (u^n - \phi_\theta^n)}{\Delta t} + u^n u_\theta^n + v^n u_\eta^n + p_{1,\theta} - \nu u_{a,\eta\eta}^{n+1} = [v^n\omega^n]_{\eta=\eta_{\max}}$$

$$u_a^{n+1} = u_0^{n+1} \text{ at } \eta = 0, \quad u_{a,\eta\eta}^{n+1} = 0 \text{ at } \eta = \eta_{\max}.$$

p_1 is defined (in step 3) such that at $\eta = \eta_{\max}$, $u_a^{n+1} = \tilde{u}_I^{n+1}$.

6. Define $\dfrac{u_b^{n+1} - \phi_\theta^n}{\Delta t} + p_{2,\theta} = 0$. Note that $u_b^{n+1} = \phi_\theta^{n+1}$.

7. Define $\dfrac{u_c^{n+1}}{\Delta t} = -[v^n\omega^n]_{\eta=\eta_{\max}}$, to model shed vorticity.

8. u_h^{n+1} is used to satisfy no-slip boundary condition.

$$\frac{u_h^{n+1}}{\Delta t} = \nu u_{h,\eta\eta}^{n+1} \qquad \begin{cases} u_h^{n+1} = 1 \text{ at } \eta = 0 \\ u_h^{n+1} = 0 \text{ at } \eta = \eta_{\max} \end{cases}$$

$$\Rightarrow u_h^{n+1} = \frac{\sinh(\eta_{\max} - \eta/\sqrt{\nu\Delta t})}{\sinh(\eta_{\max}/\sqrt{\nu\Delta t})}.$$

Set $q = -u_b^{n+1} - u_c^{n+1}$ so that $u^{n+1} = u_0^{n+1}$ at $\eta = 0$.

10. Calculate the normal velocity component in terms of ϕ^{n+1} using $u_\theta^{n+1} + v_\eta^{n+1} = 0$. At the interface,

$$v^{n+1} = -\int_0^{\eta_{\max}} u_{a,\theta}^{n+1} + (\phi_{\theta\theta}^{n+1} + u_{c,\theta}^{n+1})(\eta_{\max} - \sqrt{\nu\Delta t}).$$

Adding steps 4, 6, 7 and 8 gives

$$\frac{u^{n+1} - u^n}{\Delta t} + u^n u_\theta^n + v^n u_\eta^n + p_\theta^{n+1} = \nu u_{\eta\eta}^{n+1}.$$

At $\eta = \eta_{\max}$, both components of velocity fields match exactly:

$\tilde{u}_I^{n+1} + \tilde{\boldsymbol{u}}_{\text{new}}^{n+1} \cdot \hat{\boldsymbol{t}} + \phi_\theta^{n+1} = u_a^{n+1} + u_c^{n+1} + u_b^{n+1} + q(\theta)\, u_h^{n+1}$ (steps 4, 6, 8 and 9) and $\boldsymbol{u}_{\text{out}}^{n+1} \cdot \hat{\boldsymbol{n}} = v_0^{n+1} + v^{n+1}$ (step 12).

Table 1: *Operator splitting time-stepping algorithm. The velocity and pressure are split in parts as shown on the first line, and the steps 1-12 are sequentially carried out. Left column denotes operations on the outer region, and right on boundary layer variables. The equations governing each of these parts are shown in Azure and Almond color backgrounds, and the relations between the boundary layer and outer variables are highlighted in other color backgrounds. The last line summarizes the matching of the velocity components at the interface* $\eta = \eta_{max}$.

DISTRIBUTION A: Distribution approved for public release.

5 Administrative report

5.1 Personnel

Faculty supported: Kenneth Breuer (experiment) and Shreyas Mandre (theory).

Post doctoral research fellows: Ponnulakshmi Kartheeswaran (theory).

Graduate students: Xinjun Guo (supervised by S. Mandre), Kyohei Onoue (supervised by K. Breuer)

5.2 Refereed conference proceedings and archival journal articles

1. S Mandre, X Guo and P Kartheeswaran. (2014). A reduced model for vortex shedding from a body using matched asymptotics, XXVI IUPAP Conference on Computational Physics.
2. K Onoue, A Song, BW Strom and KS Breuer. (2014). Cyber-physical energy harvesting through flow-induced oscillations of a rectangular plate, in 32nd ASME Wind Energy Symposium. American Institute of Aeronautics and Astronautics.
3. K Onoue, B Strom and KS Breuer. (2014). Vortex shedding and energy harvesting from a cyber-physical compliant flat plate. 17th US National Congress on Theoretical and Applied Mechanics, Michigan.
4. K Onoue, A Song, B Strom and KS Breuer. (2015). Large amplitude flow-induced oscillations and energy harvesting using a cyber-physical pitching plate. Journal of Fluids and Structures 55, 262-275 (*PDF attached to report*)
5. K Onoue and KS Breuer. (2015). Vortex formation and shedding from a cyber-physical pitching plate. Journal of Fluid Mechanics (in review). (*PDF attached to report*)

5.3 Non-refereed conference presentations

1. X Guo and S Mandre. (2012). Optimization of the airfoil stroke in a high Reynolds number flow for energy harvesting, 65th Annual Meeting of the APS Division of Fluid Dynamics.
2. K Onoue, B Strom, A Song, and KS Breuer. (2013). Vortex induced vibrations of a flexibly mounted cyber physical rectangular plate.Annual Meeting of the American Physical Society, Division of Fluid Dynamics. Pittsburgh PA.
3. X Guo and S Mandre. (2013). Vortex shedding in flow past an airfoil using boundary layer, 66th Annual Meeting of the American Physical Society Division of Fluid Dynamics. Pittsburgh PA.
4. S Mandre, X Guo, and P Kartheeswaran. (2014). A reduced model for vortex shedding from a body using matched asymptotics, 67th Annual Meeting of the American Physical Society Division of Fluid Dynamics.

DISTRIBUTION A: Distribution approved for public release.

5. X Guo and S Mandre (2014). Vortex shedding by matched asymptotic vortex method, 67th Annual Meeting of the American Physical Society Division of Fluid Dynamics. San Francisco CA.
6. P Kartheeswaran, X Guo and S Mandre. (2014). A reduced model for un- steady laminar flow past a solid body using matched asymptotics, 67th Annual Meeting of the American Physical Society Division of Fluid Dynamics. San Francisco CA.
7. K Onoue and KS Breuer. (2014). Vortex formation, shedding and energy harvesting from a cyber-physical pitching flat plate, volume 59. Annual Meeting of the American Physical Society, Division of Fluid Dynamics. San Francisco CA.

Additional publications are currently in preparation.

DISTRIBUTION A: Distribution approved for public release.

References

[1] R Bisplinghoff, H Ashley, and R Halfman. (1955), *Aeroelasticity*, Addison Wellesley (Reprinted, Dover Press).

[2] EH Dowell and KC Hall. (2001), Modeling of Fluid-Structure Interaction, *Ann. Rev. Fluid Mech.* **33**, 445–490.

[3] JR Wright and JE Cooper. (2007), *Introduction to aircraft aeroelasticity and loads*, Wiley.

[4] S Heathcote, Z Wang, and I Gursul. (2008), Effect of spanwise flexibility on flapping wing propulsion, *J. Fluids & Struct.* **24**, 183-199.

[5] KB Lua, KC Lai, TT Lim, and KS Yeo. (2010), On the aerodynamic characteristics of hovering rigid and flexible hawkmoth-like wings, *Expt. Fluids* **49**, 1263–1291.

[6] P Wu, BK Stanford, E Sällström, L Ukeiley, and PG Ifju. (2011), Structural dynamics and aerodynamics measurements of biologically inspired flexible flapping wings, *Bioinsp. & Biomim.* **6**, 6009.

[7] K Onoue, A Song, BW Strom, and KS Breuer. (2015), Cyber-physical energy harvesting through flow-induced oscillations of a rectangular plate, *J. Fluids & Struct.* **55**, 262-275.

[8] F Hover, S Miller, and M Triantafyllou. (1997), Vortex-induced vibration of marine cables: Experiments using force feedback, *J. Fluids & Struct.* **11**, 307-326.

[9] AW Mackowski and CHK Williamson. (2011), Developing a cyber-physical fluid dynamics facility for fluid-structure interaction studies, *J. Fluids & Struct.* **27**, 748-757.

[10] RD Blevins. (1990), *Flow-Induced Vibration*, Kreiger.

[11] NA Razak, T Andrianne, and G Dimitriadis. (2011), Flutter and stall flutter of a rectangular wing in a wind tunnel, *AIAA J.* **49**, 2258-2271.

[12] G Dimitriadis and J Li. (2009), Bifurcation behavior of airfoil undergoing stall flutter oscillations in low-speed wing tunnel, *AIAA J.* **47**, 2577-2596.

[13] X Amandolese, S Michelin, and M Choquel. (2013), Low speed flutter and limit cycle oscillations of a two-degree-of-freedom flat plate in a wind tunnel, *J. Fluids & Struct.* **43**, 244-255.

[14] WJ McCroskey. (1982), Unsteady airfoils, *Ann. Rev. Fluid Mech.* **14**, 285-311.

[15] Y Baik, L Bernal, K Granlund, and M Ol. (2012), Unsteady force generation and vortex dynamics of pitching and plunging aerofoils, *J. Fluid. Mech.* **709**, 37-68.

[16] AC DeVoria and MJ Ringuette. (2012), Vortex formation and saturation for low-aspect-ratio rotating flat-plate fins, *Expt. Fluids* **52**, 441-462.

[17] MJ Ringuette, M Milano, and M Gharib. (2007), Role of the tip vortex in the force generation of low-aspect-ratio normal flat plates, *J. Fluid. Mech.* **581**, 453.

[18] P Sattari, DE Rival, RJ Martinuzzi, and C Tropea. (2012), Growth and separation of a start-up vortex from a two-dimensional shear layer, *Phys. Fluids.* **24**, 107102.

[19] BJ Simpson, S Licht, F Hover, and MS Triantafyllou. (2008), Energy extraction through flapping foils, in *Proceedings of the 27th International Conference on Offshore Mechanics and Arctic Engineering.*

[20] Z Peng and Q Zhu. (2009), Energy harvesting through flow-induced oscillations of a foil, *Phys. Fluids.* **21**, 123602.

[21] Q Xiao and Q Zhu. (2014), A review on flow energy harvesters based on flapping foils, *J. Fluids & Struct.* **46**, 174-191.

[22] B Strom, D Kim, S Mandre, and K Breuer. (2014), Parametric dependence of energy harvesting performance with an oscillating hydrofoil, in *Bull. Am. Phys. Soc.* volume 59. APS.

[23] Q Wang, P Moin, and G Iaccarino. (2009), Minimal repetition dynamic checkpointing algorithm for unsteady adjoint calculation, *SIAM J Sci. Comp.* **31**, 2549–2567.

[24] Y Tanabe and K Kaneko. (1994), Behavior of a falling paper, *Phys Rev. Lett.* **73**, 1372–1375.

[25] L Mahadevan. (1996), Tumbling of a falling card, *Comptes rendus de l'Académie des sciences. Série II, Mécanique, physique, chimie, astronomie* **323**, 729–736.

[26] A Belmonte, H Eisenberg, and E Moses. (1998), From flutter to tumble: inertial drag and Froude similarity in falling paper, *Phys Rev. Lett.* **81**, 345.

[27] L Mahadevan, WS Ryu, and ADT Samuel. (1999), Tumbling cards, *Phys. Fluids.* **11**, 1.

[28] U Pesavento and ZJ Wang. (2004), Falling paper: Navier-Stokes solutions, model of fluid forces, and center of mass elevation, *Phys Rev. Lett.* **93**, 144501.

[29] A Andersen, U Pesavento, and Z Wang. (2005), Unsteady aerodynamics of fluttering and tumbling plates, *J. Fluid. Mech.* **541**, 65–90.

[30] K Ramesh, A Gopalarathnam, K Granlund, MV Ol, and JR Edwards. (2014), Discrete-vortex method with novel shedding criterion for unsteady aerofoil flows with intermittent leading-edge vortex shedding, *J. Fluid. Mech.* **751**, 500–538.

[31] MH Hansen, M Gaunaa, and H Aagaard Madsen. (2004), A Beddoes-Leishman type dynamic stall model in state-space and indicial formulations, Technical report. Riso National Laboratory. Roskilde, Denmark.

DISTRIBUTION A: Distribution approved for public release.

[32] SL Brunton and CW Rowley. (2013), Empirical state-space representations for Theodorsen's lift model, *J. Fluids & Struct.* **38**, 174-186.

[33] TJ Pedley and SJ Hill. (1999), Large-amplitude undulatory fish swimming: fluid mechanics coupled to internal mechanics, *Journal of Experimental Biology* **202**, 3431–3438.

[34] MA Jones and MJ Shelley. (2005), Falling cards, *J. Fluid. Mech.* **540**, 393–425.

[35] RK Shukla and JD Eldredge. (2007), An inviscid model for vortex shedding from a deforming body, *Theo. Comp. Fluid Dyn.* **21**, 343–368.

[36] K Singh and TJ Pedley. (2008), The hydrodynamics of flexible-body manoeuvres in swimming fish, *Physica D: Nonlinear Phenomena* **237**, 2234–2239.

[37] S Alben. (2009), Simulating the dynamics of flexible bodies and vortex sheets, *J. Comp. Phys.* **228**, 2587–2603.

[38] S Michelin and S Llewellyn Smith. (2009), An unsteady point vortex method for coupled fluid-solid problems, *Theo. Comp. Fluid Dyn.* **23**, 127-153.

[39] S Michelin and S Llewellyn Smith. (2010), Falling cards and flapping flags: understanding fluid–solid interactions using an unsteady point vortex model, *Theo. Comp. Fluid Dyn.* **24**, 195–200.

[40] JX Sheng, A Ysasi, D Kolomenskiy, E Kanso, M Nitsche, and K Schneider. (2012), Simulating vortex wakes of flapping plates, in *Natural Locomotion in Fluids and on Surfaces*. Springer. pp. 255–262.

[41] AJ Chorin. (1978), Vortex sheet approximation of boundary layers, *J. Comp. Phys.* **27**, 428–442.

[42] A Leonard. (1980), Vortex methods for flow simulation, *J. Comp. Phys.* **37**, 289–335.

[43] JA Sethian and AF Ghoniem. (1988), Validation study of vortex methods, *J. Comp. Phys.* **74**, 283–317.

[44] CR Anderson. (1989), Vorticity boundary conditions and boundary vorticity generation for two-dimensional viscous incompressible flows, *J. Comp. Phys.* **80**, 72–97.

[45] AJ Chorin. (1993), Vortex methods, Technical report. Lawrence Berkeley Lab., CA (United States).

[46] P Koumoutsakos, A Leonard, and F Pepin. (1994), Boundary conditions for viscous vortex methods, *J. Comp. Phys.* **113**, 52–61.

[47] DM Summers and AJ Chorin. (1996), Numerical vorticity creation based on impulse conservation, *Proc. Nat. Acad. Sci.* **93**, 1881–1885.

[48] JD Eldredge, T Colonius, and A Leonard. (2002), A vortex particle method for two-dimensional compressible flow, *J. Comp. Phys.* **179**, 371–399.

DISTRIBUTION A: Distribution approved for public release.

[49] PG Saffman. (1992), *Vortex dynamics*, Camb. Univ. Press.

[50] J Yao and DS Stewart. (1996), The dynamics of multi-dimensional detonation, *J Fluid Mech.* **309**, 225-275.

[51] M Matalon, C Cui, and JK Bechtold. (2003), Hydrodynamic theory of premixed flames: effects of stoichiometry, variable transport coefficients and arbitrary reaction orders, *J. Fluid. Mech.* **487**, 179–210.

[52] MR Booty and M Siegel. (2010), A hybrid numerical method for interfacial fluid flow with soluble surfactant, *J. Comp. Phys.* **229**, 3864–3883.

[53] P Koumoutsakos and A Leonard. (1995), High-resolution simulations of the flow around an impulsively started cylinder using vortex methods, *J. Fluid. Mech.* **296**, 1–38.

[54] M Bar-Lev and HT Yang. (1975), Initial flow field over an impulsively started circular cylinder, *J. Fluid. Mech.* **72**, 625–647.

DISTRIBUTION A: Distribution approved for public release.

A Journal articles directly derived from this grant

DISTRIBUTION A: Distribution approved for public release.

Journal of Fluids and Structures 55 (2015) 262–275

Contents lists available at ScienceDirect

Journal of Fluids and Structures

journal homepage: www.elsevier.com/locate/jfs

Large amplitude flow-induced oscillations and energy harvesting using a cyber-physical pitching plate

Kyohei Onoue *, Arnold Song [1], Benjamin Strom [2], Kenneth S. Breuer

Brown University School of Engineering, Providence, Rhode Island 02912, USA

ARTICLE INFO

Article history:
Received 25 January 2014
Accepted 2 March 2015
Available online 27 April 2015

Keywords:
Cyber-physical system
Energy harvesting
Limit-cycle oscillations
Fluid-structure interactions

ABSTRACT

The dynamics of an elastically mounted flat plate in a uniform stream undergoing flow-induced pitching oscillations is studied with the aid of a cyber-physical system which is capable of simulating arbitrary structural dynamics. The system measures the angular position and velocity, and combines them with appropriate gains to provide a torque to a computer-controlled servomotor that emulates arbitrary torsional stiffness and damping. A series of experiments were carried out over a wide range of parameter space and the results demonstrate that inertial scaling of the stiffness and damping effectively captures the system behavior. As the torsional stiffness decreases, the system exhibits several bifurcations in its dynamical behavior. Firstly, a subcritical transition through a saddle-node bifurcation results in small-amplitude asymmetric limit-cycle oscillations and later, a subcritical transition through a Hopf bifurcation gives rise to large-amplitude symmetric limit-cycle oscillations. At very low stiffness the plate does not oscillate. Energy harvesting from the flow is only $\sim 1\%$ efficient, but is found to be optimized at a non-dimensional stiffness close to unity while increasing the Reynolds number is found to extend the range of damping over which large scale oscillations and energy harvesting can be sustained. Although velocity measurements are not made, the details of torque-position phase plane are used to infer the details of the formation time and stability of the leading-edge vortex associated with the rapidly pitching plate.

© 2015 Elsevier Ltd. All rights reserved.

1. Introduction

The unsteady motion of an elastically supported structure immersed in a fluid flow has been a problem of technical and scientific interest for decades, originating from the aeroelastic excitation of aircraft wings, marine structures, bridges, and even traffic signs (Bisplinghoff et al., 1957; Blevins, 1990). In recent years, harvesting of the aeroelastic motions has also been explored for energy conversion applications (Bernitsas et al., 2008; Frayne, 2011). The onset of small amplitude motions can be predicted using classical theories (e.g., Theodorsen, 1935) for which linear potential flow assumptions remain valid. However, for larger-amplitude motion, vortex growth and separation dominate the flow both on the body and in the wake, and the linear models are unable to predict the details either of the vortex dynamics or the unsteady forces that the flow imparts to the elastic structure. Developing a more sophisticated model is challenging, and part of the difficulty lies in

---

* Correspondence to: 182 Hope Street Box D, Providence, RI, 02912, USA.
E-mail addresses: kyohei_onoue@brown.edu (K. Onoue), arnsong@gmail.com (A. Song), strombw@uw.edu (B. Strom), kbreuer@brown.edu (K.S. Breuer).

[1] Current address: Cold Regions Research and Engineering Laboratory, Hanover, NH, USA.

[2] Current address: Dept of Mechanical Engineering, University of Washington, Seattle, WA, USA.

http://dx.doi.org/10.1016/j.jfluidstructs.2015.03.004
0889-9746/© 2015 Elsevier Ltd. All rights reserved.

DISTRIBUTION A: Distribution approved for public release.

Nomenclature

U_∞	free-stream velocity (m/s)
c	chord (m)
h	span (m)
δ	plate thickness (m)
ν	kinematic viscosity of the fluid (m^2/s)
ρ	fluid density (kg/m^3)
t	time (s)
α	angle of attack (rad)
α_0	equilibrium angle of attack (rad)
$\alpha_{\max}$	maximum angular position (rad)
$\overline{\alpha}$	time-averaged mean angle of attack
$\Delta\alpha$	peak amplitude (rad) $\Delta\alpha = \alpha_{max} - \overline{\alpha}$
I	mass moment of inertia (kg m^2)
k	torsional spring stiffness (N m/rad)
b	linear damping coefficient (N m s/rad)
I^*	dimensionless mass moment of inertia
b^*	dimensionless linear damping
k^*	dimensionless torsional spring stiffness
Re	Reynolds number
ξ	damping ratio
ω_n	undamped natural frequency (rad/s)
ω_p	pitching frequency (rad/s)
ω_p^*	reduced pitching frequency
ω_d	damped natural frequency (rad/s)
ω_d^*	reduced damped natural frequency
T	period of oscillation (s) $T = 2\pi/\omega_p$
τ_f	aerodynamic torque (N m)
W	average work per cycle (J)
N	number of cycles
C_p	power coefficient
C_m	steady moment coefficient about the mid-chord point

finding a unifying scaling of the leading-edge vortex (LEV) formation time, strength and stability that can be generalized to various geometries and kinematics. Our current ability to model large-amplitude oscillations due to fluid–structure instabilities remains insufficient, albeit a number of experimental studies reported in the archival literature (e.g., Dimitriadis and Li, 2009; Razak et al., 2011; Amandolese et al., 2013). Significant efforts have been made to elucidate the mechanism by which a classical linear flutter transforms into a complex bifurcation behavior that leads to violent oscillations induced by the dynamic stall phenomenon. Although the physical mechanism of the stall flutter is well understood, it still poses a great challenge to accurately correlate the aerodynamic loads due to unsteady vortex formation and shedding with the resulting dynamics of an elastically supported structure.

Recent studies that focused exclusively on characterization of the LEV formation have used predefined kinematic motion of a sharp-edged flat plate to explore the forces induced by pitching (Granlund et al., 2013; Jantzen et al., 2014), rotation (DeVoria and Ringuette, 2012; Wojcik and Buchholz, 2014), and plunging (Rival et al., 2009; Ford and Babinsky, 2013). Numerous studies on pitching and/or plunging wings with sufficient forcing have identified reduced frequency as the primary scaling parameter that determines the flow evolution and unsteady force (see, e.g., Baik et al., 2012; Jantzen et al., 2014). However, the measurements of Granlund et al. (2013) have shown that the pitch rate contribution to unsteady force is largely dependent on the location of the pitch axis, presumably because the vorticity distribution and non-circulatory loads on the wing vary sensitively with the pitch axis, as has been demonstrated by Yu and Bernal (2013). Therefore, the applicability of scaling relations based solely on reduced frequency (such as those of Ol et al., 2010; Jantzen et al., 2014) may be quite limited. More detailed characterization of large-amplitude pitching plate is still required to determine a more robust scaling parameter that captures the essential features of the unsteady aerodynamics with variations in plate configurations and kinematics.

It is nevertheless well-established by now that the LEV formation on an unsteady flat plate is responsible for significant enhancement in lifting force that far exceeds its static counterpart. Hence from the energy harvesting point of view, one may surmise that the LEV dynamics can also have a significant impact on the amount of fluid energy that can be harvested by the elastic structures through large-scale coupled-mode flutter mechanisms. The numerical investigations of Peng and Zhu (2009) and Zhu and Peng (2009) reinforced the importance of vorticity control mechanism, wherein the energy of LEVs is partially recovered through favorable vortex–body interactions, in enhancing the system's overall energy harvesting capacity.

Experimental studies of energy harvesting are less common in the archival literature. Part of the difficulty lies in creating a physical experiment in the laboratory scale that possesses the characteristics for optimal energy harvesting. One approach to overcome this issue is the use of a “cyber-physical” system in which the mechanical properties of the system (e.g. stiffness, damping) are generated using a control algorithm that measures the state of the system and feeds back restoring torques and forces so as to simulate the appropriate structural stiffness and damping. Thus far, the cyber-physical systems reported have been used to investigate vortex-induced vibration (VIV) behavior of elastically mounted marine cables and cylinders in water (Hover et al., 1997; Mackowski and Williamson, 2011, 2013; Lee et al., 2011; Lee and Bernitsas, 2011). The implementation in water typically allows for testing in relatively low speed flows (and hence requiring low bandwidth control systems) while still being able to explore moderate Reynolds number regimes that range from $\mathcal{O}(10^3)$ to $\mathcal{O}(10^5)$. With the exception of the preliminary results presented by Song (2013), cyber-physical implementations of pitching and/or plunging airfoils or of systems using air as the working fluid have not yet been reported.

In the current paper, we take advantage of the wide range of parameters that can be explored using a cyber-physical system to report on the flow-induced oscillations of a flat plate, mounted at mid-chord and immersed in an airstream. This geometry has the advantage of simplicity; the sharp leading and trailing edges fix the separation points while the single degree of freedom means that the available parameter space (stiffness, damping and Reynolds number) is constrained so that we can fully understand the fluid–structure interaction. The objectives of the present investigation are three-fold: (1) to

DISTRIBUTION A: Distribution approved for public release.

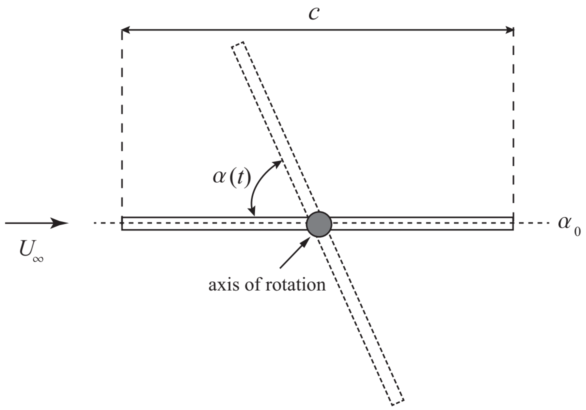

Fig. 1. A schematic of the oscillating flat plate (with 1 DOF). The axis of rotation is placed at the mid-chord point to ensure symmetry, and the sharp edges of the plate fix the flow separation points at the leading and trailing edges.

demonstrate the successful implementation of a high-bandwidth cyber-physical system in a wind tunnel, and confirm its capability to simulate a wide range of structural stiffness and damping, (2) to determine the scaling of the aeroelastic behavior with respect to the geometric, elastic and fluid parameters, and (3) to assess the system's ability to harvest energy from a uniform airflow as a function of these parameters.

2. Experimental system and dimensional scaling

2.1. Schematic description and dimension scaling

Fig. 1 illustrates a flat plate, with chord c, span, h, thickness, δ, and mass moment of inertia, I, free to rotate in pitch about its mid-chord in a uniform airflow of density ρ and magnitude U_∞. The structural behavior of the plate is determined by a torsional spring and damper, characterized by coefficients k and b respectively. The dynamics of this single-degree-of-freedom plate in response to aerodynamic forcing, τ_f, can be modeled as a forced torsional harmonic oscillator

$$I\ddot{\alpha}(t)+b\dot{\alpha}(t)+k(\alpha(t)-\alpha_o)=\tau_f(t) \tag{1}$$

where α is the rotational position of the plate, α_o is the equilibrium angle of the torsional spring and dots represent time derivatives.

In this study, we are primarily interested in very strong fluid-structure interactions which drive large-scale structural motions. For such interactions, we hypothesize that the dominant scaling force will be related to the inertial forcing by the fluid, ρU_∞^2 (Shiels, 1998; Gharib, 1999). With this assumption, the reduced torsional spring stiffness, k^*, which gives the ratio between the elastic restoring force and aerodynamic force can be written as

$$k^*=\frac{2k}{\rho U_\infty^2 c^2 h}. \tag{2}$$

Similarly, the dimensionless damping, b^*, which describes the ratio between the structural damping force and aerodynamic force is given by

$$b^*=\frac{2b}{\rho U_\infty c^3 h}, \tag{3}$$

and the dimensionless inertia, I^* (often called the “mass parameter”) which compares the plate inertia to that of the surrounding fluid is given by

$$I^*=\frac{2I}{\rho c^4 h}. \tag{4}$$

Alternative scalings have been proposed, such as the traditional reduced velocity and damping ratio, that use purely structural parameters (i.e. the structural mass and the natural frequency time scale) as utilized, for example, by Khalak and Williamson (1999). However, such formulation lacks a clear connection to the fluid dynamical aspects of the problem and causes the normalized structural parameters to be coupled. Lastly, provided that the Reynolds number is large (in the present study, it is $\mathcal{O}(10^5)$), and the separation points are well-defined (ensured in the current study by the use of a sharp-edged flat plate), it is reasonable to assume that the viscosity plays only a minor role in the overall dynamics. For these reasons a viscous time scale is probably not an appropriate choice. The validity of the current normalization will be tested in the accompanying experiments.

DISTRIBUTION A: Distribution approved for public release.

2.2. Experimental implementation

Fig. 2 shows a schematic of the experimental configuration used in the current work, illustrating the flat plate mounted to a virtual spring–damper system in the wind tunnel test section. The closed-return wind tunnel has a test section of 0.61 m in width, 0.61 m in depth, and 1.22 m in length. The turbulence level was previously measured to be less than 0.1% of the free-stream velocity (Song et al., 2008). Titanium plates, 1 mm in thickness, were attached to a steel shaft with a diameter of 1 cm mounted vertically between the floor and ceiling of the test section. Two different configurations were tested, with chord dimensions of 0.1 m and 0.15 m. In both cases, the plate span was 0.53 m, giving aspect ratios of 5.3 and 3.5. The experiments were performed at free-stream velocities ranging from 10 m/s to 25 m/s, corresponding to Reynolds numbers, based on the chord length, ranging from $\mathcal{O}(10^4)$ to $\mathcal{O}(10^5)$. Since the chord represented no more than 25% of the test section width, blockage and side wall boundary layer effects were deemed insignificant.

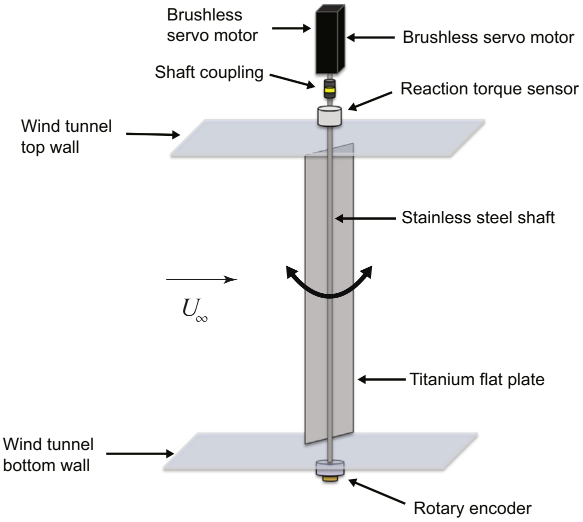

Fig. 2. Experimental setup: a computer-controlled servomotor rotates the shaft-plate assembly by applying a specific amount of torque determined numerically to realize desired structural dynamics.

2.3. Cyber-physical system control scheme

Rather than using a physical torsional spring and damper, the structural stiffness and damping characteristics of the pitching plate were controlled using a cyber-physical system consisting of a servomotor, rotary encoder and torque sensor coupled to a real-time digital control system (Fig. 3). The top end of the shaft was coupled to a brushless servomotor (SM233AE, Parker Compumotor, Rohnert Park, CA) via a reaction torque sensor (TFF400 Futek, Irvine, CA) while the bottom end of the shaft was attached to a rotary encoder (HB6M Optical Encoder, US Digital, Vancouver, WA). A tachometer (ETCH2, USDigital, Vancouver, WA) was used to calculate the angular velocity in real time from the encoder readings.

Simulink (Mathworks, Natick MA) was used to implement the real-time digital control system. The torque, position and velocity signals were sampled at 4 kHz (PC6259, National Instruments, Austin, TX), filtered using a linear phase low pass filter with the cutoff at the Nyquist frequency and converted into physical units. The position, α, and the velocity, $\dot{\alpha}$, were then multiplied by the user-selected stiffness and damping coefficients, k_v and b_v respectively, and then combined to give the target motor torque, τ. This torque was then applied to the motor using the manufacturer-supplied torque–voltage conversion factor. The servo motor controller (Model: DPRALTE-020B080, Advanced Motion Controls, Camarillo, CA) employed an internal PID controller operating at 20 kHz ensuring that the torque applied to the motor remained accurate, independent of load, speed and position.

Although arbitrary plate inertia, I, can be simulated using cyber-physical systems (see, for example, Hover et al., 1997; Mackowski and Williamson, 2011) the current work is restricted to cases in which the effective inertia was the same as the physical inertia ($I = I_p$, where the subscript "p" here, and elsewhere denotes a physical quantity). As described above, the physical system does not possess a physical torsional spring ($k_p = 0$) and the effective stiffness is solely due to the virtual spring provided by the cyber-physical system ($k = k_v$). Lastly, the effective structural damping is provided by a combination of inherent physical damping due to friction in the bearings, and the virtual damping added by the cyber-physical model ($b = b_p + b_v$). Ideally the physical damping should be small compared with the virtual damping, and this will be confirmed in the following section. Lastly, we note that the energy "dissipated" by the virtual damping system represents energy that, with appropriate electronic circuitry, could be harvested and put to practical use.

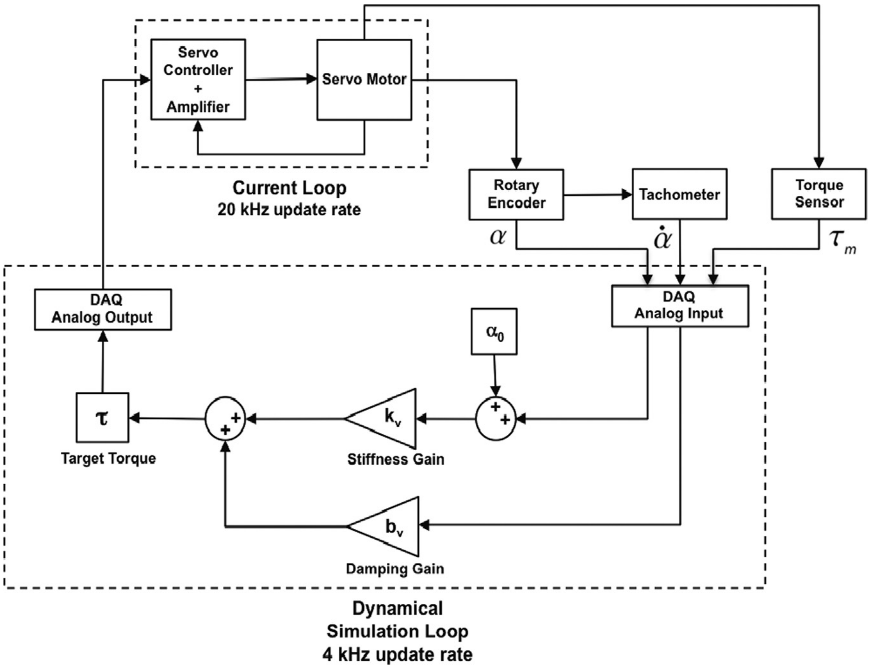

Fig. 3. The cyber-physical system control scheme composed of two feedback loops: (1) a current following loop with a 20 kHz update rate internal to the servo controller and (2) a dynamical simulation loop operating at 4 kHz calculates a target torque value based on the user-specified torsional stiffness and damping gains.

2.4. Testing procedures

Prior to any fluid–structure experiments, an extensive series of validation experiments was performed to assess the behavior of the wind tunnel model and specifically (i) to characterize the internal (physical) damping of the motor-bearing assembly, b_p, and (ii) to confirm that the cyber-physical system was capable of accurately simulating the linear structural dynamics of a lightly damped spring–mass system. Once the suitability of the model was confirmed, a wide variety of measurements were taken to assess the fluid–structure interactions, and the energy harvesting performance of the cyber-physical flat plate.

In each trial, the value of torsional spring stiffness, k, was varied, while the other parameters (i.e., free-stream velocity, U_∞, equilibrium angle of attack, α_o, damping, b, and plate's mass moment of inertia, I) were all held constant. Thus, the torsional spring stiffness served as the variable to modulate the structural frequency and the stability of the system. In most experiments the dimensionless stiffness was initially set at a high value and then reduced incrementally. A range of damping coefficients and wind speed were considered for the two different plates. The values of stiffness, damping, and wind speed were chosen such that the dimensionless stiffness and damping spanned roughly the same range across all experiments. These experiments enabled us to systematically observe the onset of instabilities, to characterize the general behavior of the system and to validate the inertial scaling proposed. Note that, by directly controlling the structural stiffness and damping, k and b, we are able to change the fluid–structure interaction parameters, k^* and b^*, while keeping the Reynolds number (and thus the pure fluid effects) constant.

In post-processing, the aerodynamic torque was determined from the equation of motion (Eq. (1))

$$\tau_f(t) = I\ddot{\alpha}(t) + b_p\dot{\alpha}(t) + \tau_m(t), \tag{5}$$

where $\tau_m(t) = b_v\dot{\alpha}(t) + k_v\alpha(t)$. To evaluate the terms in the equation, the position and torque signals were filtered by employing a zero-phase, sixth order Butterworth low-pass filter with a cut-off frequency set to 10 times the motion frequency. Second-order-accurate finite differences were used to evaluate the angular velocity and acceleration.

3. Results and discussion

3.1. Cyber-physical system validation tests

Several tests were performed to determine the stiffness and damping characteristics of the system. First, the linearity of the cyber-physical torsional spring, k_v, was confirmed for spring stiffnesses ranging from 0 to 4 Nm/rad. Next, the physical damping associated with the motor and shaft bearings, b_p, was determined by measuring the torque associated with rotating the motor and shaft over a range of constant angular velocities. The measured data is shown in Fig. 4a, from which

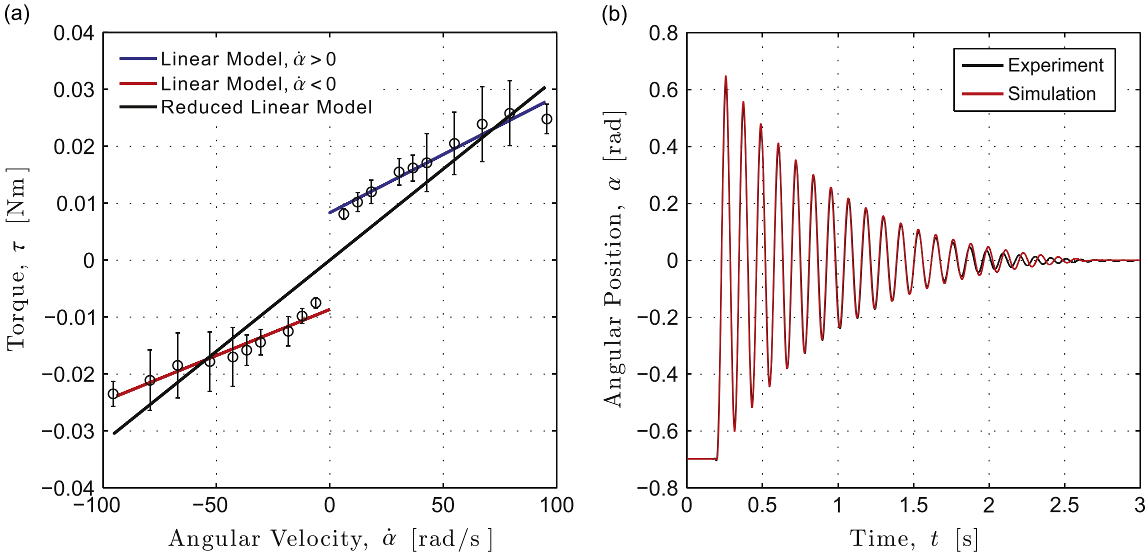

Fig. 4. (a) Damping model identification. The linear damping model is plotted in blue for ($\dot{\alpha} > 0$) and red for ($\dot{\alpha} < 0$). The reduced linear model is plotted in black. (b) Comparison of the experimentally observed free-oscillation behavior with the simulation: initial displacement=40°, $k = 2.49$ N m/rad, $b = 0.002$ N m s/rad, and $I = 7.82 \cdot 10^{-4}$ kg m^2.

we see that the friction is composed of both Coulomb and linear damping components

$$\tau_{m+b}(\dot{\alpha}) = b_1(\dot{\alpha}) + b_2 \ \mathrm{sgn}(\dot{\alpha}), \tag{6}$$

where τ_{m+b} denotes the total frictional torque due to motor and bearing. The coefficients, b_1 and b_2, were found by fitting the linear regression line to the experimental data. The resulting regression equations are provided below

$$\begin{aligned} \tau_{m+b}(\dot{\alpha}) &= 2.05 \cdot 10^{-4}(\dot{\alpha}) + 8.3 \cdot 10^{-3} \mathrm{sgn}(\dot{\alpha}), \quad (\dot{\alpha} > 0) \\ \tau_{m+b}(\dot{\alpha}) &= 1.62 \cdot 10^{-4}(\dot{\alpha}) - 8.6 \cdot 10^{-3} \mathrm{sgn}(\dot{\alpha}), \quad (\dot{\alpha} < 0). \end{aligned} \tag{7}$$

Although one would expect the damping model to be symmetric, the difference between positive and negative rotations are small, and within the range of experimental uncertainty. As will be shown later, the aerodynamic torques experienced during the aeroelastic motions are at least an order of magnitude larger than the inherent physical damping, and for this reason, it proved useful to define a simplified damping model by assuming zero Coulomb damping; this is shown as a black line in Fig. 4a. In practice the use of the simplified model yielded identical results to the those obtained with the full damping description, and so the simplified model was adopted throughout.

The last characterization experiment performed was a series of free oscillation ("ring down") experiments, which were performed for different values of plate inertia, torsional spring stiffness and damping coefficients. The response of the system from each trial was compared with that of a numerical simulation using the same parameter values. These experiments were performed both with and without the plate mounted so that different moments of inertia could be tested, and to confirm that the aerodynamic damping for these tests was negligible. In general, the results of these tests revealed excellent agreement between experiment and simulation (Fig. 4b), although for most values of k_v tested, the experiment is observed to damp out slightly faster than the simulation at the lowest amplitudes, a discrepancy believed to be attributable to the simplified treatment of the Coulomb friction discussed above. Nevertheless, all the dynamical motions that we present associated with fluid–structure interactions have much larger angular displacements, and so these low amplitude discrepancies are deemed insignificant in practice.

The mass moment of inertia of the experimental apparatus (including the contributions from the plate, servomotor, shaft coupling, reaction torque sensor and encoder) were determined from the damping ratio, ξ, and the undamped natural frequency of the system, ω_n. The damping ratio was obtained by calculating the rate at which the damped oscillation amplitude decreased, which is given by the natural logarithm of the ratio of any two successive amplitudes. This technique is commonly referred to as the method of logarithmic decrement (for example, Dukkipati, 2004). The range of damping ratio considered in the present study is approximately $0.002 < \xi < 0.15$. The natural frequency was calculated from the simple relationship, $\omega_d = \omega_n \sqrt{1-\xi^2}$, where $\omega_d = 2\pi/T_d$. The natural period of damped oscillation, T_d, was determined by calculating the average period between two successive peaks. Once ω_n and k are known, the mass moment of inertia can be determined directly from the expression, $\omega_n = \sqrt{k/I}$. Using this method, the values of mass moment of inertia were determined to be $3.45 \cdot 10^{-4} \pm 0.01 \cdot 10^{-4}$ kg m^2 (c = 0.1 m) and $7.82 \cdot 10^{-4} \pm 0.02 \cdot 10^{-4}$ kg m^2 (c = 0.15 m). The mass moment of inertia of the motor-shaft assembly (excluding the plate) was $1.98 \cdot 10^{-4} \pm 0.01 \cdot 10^{-4}$ kg m^2.

3.2. *Static aerodynamic moment*

The pitching moment coefficient about mid-chord was measured experimentally using two different sized plates by varying the angle of attack between approximately $\pm 90^\circ$ at $Re = 9.9 \cdot 10^4$, as illustrated in Fig. 5a. The value of $\pi/2$, predicted by the thin-airfoil theory is plotted with a black solid line. The present results compare well with previously-reported data of Fage and Johansen (1927), Pelletier and Mueller (2000), and Amandolese et al. (2013). A careful and high-resolution measurement of the pitching moment at fixed angles is shown in Fig. 5b illustrating a deviation from the thin-airfoil results of $C_m = \pi\alpha/2$. At angles very close to zero we note that the pitching moment quickly adopts a nonzero value for any angle of attack different from zero. This is presumably due to the fact that as soon as the sharp-edge plate deviates from $\alpha = 0$, a small separation bubble forms, generating a finite pitching moment. As the angle increases, C_m increases monotonically, although the curvature changes from positive at small angles to negative at higher incidence angles, with the inflection point located at $\alpha \approx 0.07$. The significance of this shape, as well as the dotted lines and red circles shown in Fig. 5b will be discussed in context of the dynamic motion of the plate, in the following section. Finally, while not shown here, we also confirmed that the slope of the moment, $dC_m/d\alpha$, is independent of Reynolds number.

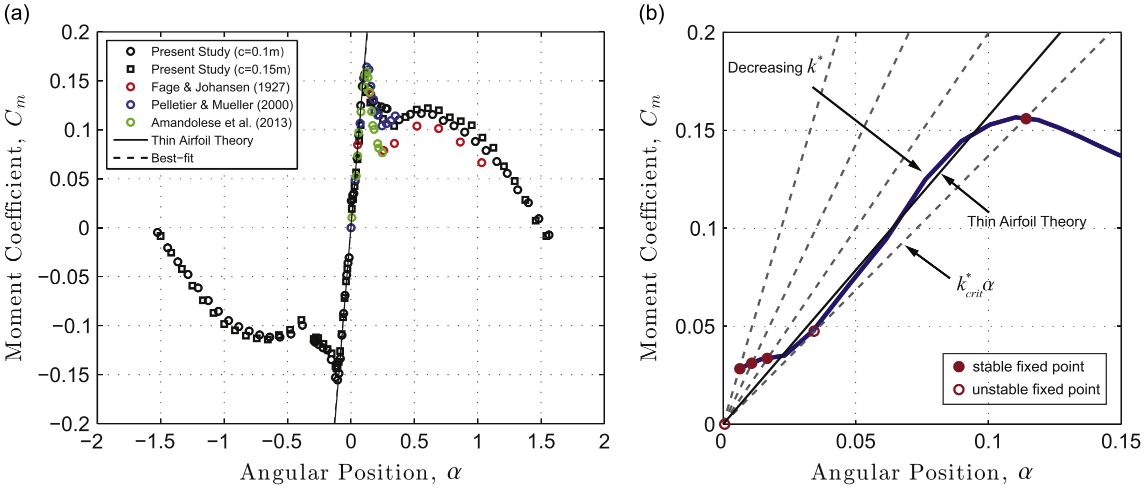

Fig. 5. (a) The evolution of static moment coefficient, $C_m(\alpha)$, as a function of the angle of attack, α, at $Re = 9.9 \cdot 10^4$: black circle ($c = 0.1$ m) and black square ($c = 0.15$ m); thickness-to-chord ratio = 1%. Fage and Johansen (1927), $Re \approx 10^4$, thickness-to-chord ratio = 3% (red circle). Pelletier and Mueller (2000), $Re \approx 8 \cdot 10^5$, thickness-to-chord ratio = 1.93% (blue circle). Amandolese et al. (2013), $Re \approx 2.3 \cdot 10^4$, thickness-to-chord ratio = 4.3% (green circle). Thin-airfoil theory, $\pi\alpha/2$ (solid black line). A best-fit line through the linear region with a slope of 1.53 (dashed line). The results of Fage and Johansen (1927) and Pelletier and Mueller (2000) were adopted from Amandolese et al. (2013). (b) $C_m(\alpha)$ versus α within a small range of α is plotted with a blue curve (only the first quadrant is shown). Various $k^*\alpha$ lines, including the critical torsional restoring torque, $k^*_{crit}\alpha \approx 1.37$, are plotted with dotted-lines. The thin airfoil theory prediction is plotted with a solid black line. Approximate locations of the unstable (open red circle) and stable (solid red circles) fixed points are given by the intersecting points between the $C_m(\alpha)$ curve and the $k^*\alpha$ lines. The origin is the unstable fixed point. (For interpretation of the references to color in this figure caption, the reader is referred to the web version of this paper.)

3.3. *Flow-induced oscillations*

We now turn to the unsteady response of the plate and describe its behavior for different values of the scaled stiffness, damping and Reynolds number. For each experiment, the plate was initially positioned parallel to the direction of free stream ($\alpha = 0$) and the structural stiffness was set to a large value as to keep the plate stationary. The structural stiffness, k^*, was then decreased incrementally, while keeping the free stream velocity (and thus, Reynolds number), damping, and mass moment of inertia constant.

3.3.1. *Amplitude response and hysteresis*

An overall phase map of the aeroelastic system response as a function of the inverse dimensionless stiffness is illustrated in Fig. 6, Here the amplitude of any unsteady motion, $\Delta\alpha$, is plotted against the inverse stiffness, $1/k^*$. The dynamical response of the system can be categorized broadly into four distinct regimes: (I) for small values of $1/k^*$, the plate remains stationary and nearly parallel to the flow. (II) As the stiffness decreases below a critical value, k^*_{crit}, a region of small amplitude limit-cycle oscillations (LCOs) is observed. These oscillations are asymmetric (e.g. Fig. 7, Region II), meaning that the midpoint of the LCOs (i.e., $(\max(\alpha) + \min(\alpha))/2$) is non-zero. (III) As the structural stiffness is reduced further, the system experiences a second instability and the pitching amplitude grows markedly, reaching a state characterized by pitching amplitudes of $\Delta\alpha \approx 1.3$, and symmetric about $\alpha = 0$. (IV) Finally, as the stiffness is reduced even further, the coupling between the fluid and structure breaks down and the plate stops oscillating, adopting a stable deflected state, perpendicular

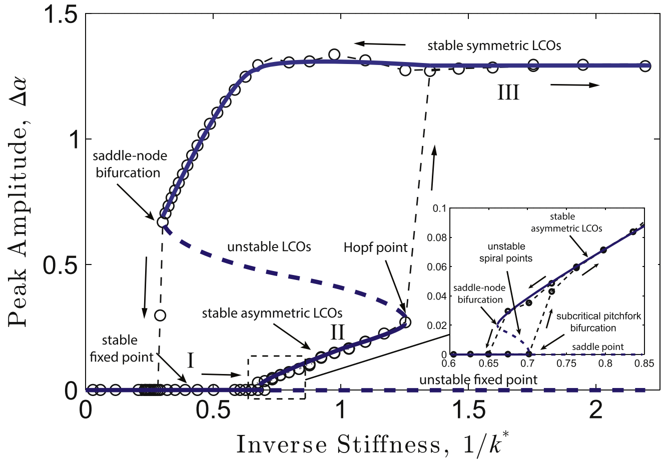

Fig. 6. An overall phase map of the aeroelastic system response as a function of the inverse dimensionless stiffness for $Re = 9.9 \cdot 10^4$, $b^* = 0.13$, and $I^* = 10.6$. The local bifurcation behavior of the system is illustrated in blue. Asymmetric LCOs are created as the system encounters a subcritical pitchfork bifurcation at the static torsional divergence condition, followed by a saddle-node bifurcation. Large symmetric LCOs are generated as a result of a subcritical Hopf bifurcation, coupled to a saddle-node bifurcation. Black arrows indicate the orientation of the hysteresis. Three distinct dynamical regimes are labeled as I (steady), II (small asymmetric LCOs) and III (large symmetric LCOs). (For interpretation of the references to color in this figure caption, the reader is referred to the web version of this paper.)

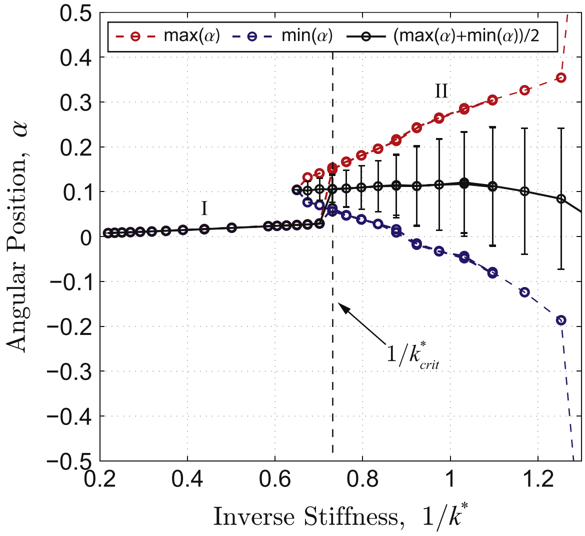

Fig. 7. A magnified view of the Regions I and II, illustrating a quasi-steady deflected state followed by an unsteady state characterized by small-amplitude asymmetric LCOs. A small region of hysteresis ($0.67 < 1/k^* < 0.73$) is portrayed. The error bars denote the standard deviation of the oscillation amplitude.

to the flow (this regime is not portrayed in Fig. 6 or 7). Similar dynamical regimes have been reported by Dimitriadis and Li (2009), who studied the stall flutter behaviors of a symmetric airfoil with pitch-plunge degrees of freedom and also by Kim et al. (2013) who examined a self-excited flapping behavior of the inverted flexible flag model with a free leading edge and a clamped trailing edge. We discuss each of these regimes in more detail in the next few paragraphs.

In Region I, when $1/k^*$ is small, the plate remains stationary ($\Delta\alpha = 0$). As $1/k^*$ increases, the plate deflects slightly while maintaining a stable state (Fig. 7, Region I). This subtle deflection with decreasing structural stiffness can be understood in conjunction with the static pitching moment (Fig. 5b). At any finite value of k^*, the plate adopts an angle such that the static aerodynamic moment is balanced by the restoring torque of the torsional spring, $k^*\alpha$. Since $C_m(\alpha)$ is concave up, as k^* decreases, this stable fixed point moves to higher values of α (Fig. 5b).

At a critical value of $1/k^*_{crit} \approx 0.73$, the plate enters Region II, in which the plate exhibits low-amplitude asymmetric LCOs (Fig. 7). At this critical stiffness value, based on the static pitching characteristics (Fig. 5b), the location of the fixed point is expected to jump from $\alpha \approx 0.03$ to 0.11 and this agrees very well with the experimental observation. The initial LCO has low amplitude, but it increases smoothly as $1/k^*$ continues to increase. The critical stiffness at which we expect to see this transition to small amplitude LCO can be predicted using the classical quasi-steady Theodorsen analysis of static torsional divergence (see, e.g., Bisplinghoff et al., 1957) in which the dynamical equation for the motion of the plate (Eq. (1)) reduces

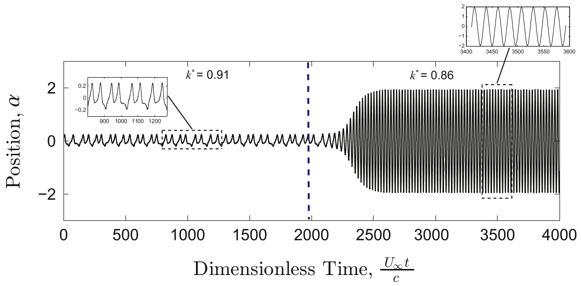

Fig. 8. The evolution of angular position as a function of the dimensionless time, $U_\infty t/c$, during a transition from small amplitude asymmetric LCOs to large amplitude symmetric LCOs. In this case, $Re = 9.9 \cdot 10^4$, $b^* = 0.03$, $I^* = 10.6$ and $\alpha_0 = 0$. The change in vibrational mode is triggered by reducing the dimensionless stiffness, k^*, from 0.91 to 0.86. The vertical dotted-line shows the instant at which the structural stiffness was reduced.

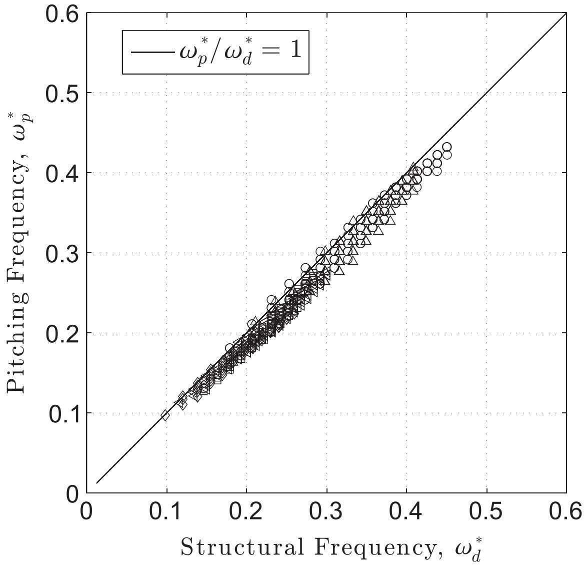

Fig. 9. Measured pitching frequency versus the structural frequency (both normalized by the chord and free stream velocity) drawn from a wide range of experiments: $U_\infty = 10 \sim 25$ m/s, $I^* = 4.8$ and 10.6, $k^* = 0.3 \sim 1.1$, and $b^* = 0.01 \sim 0.21$.

to $k^*_{crit} = dC_m/d\alpha$. The original Theodorsen analysis (based on thin-airfoil theory) predicts $k^*_{crit} = \pi/2 = 1.57$, although if we use our experimentally measured value of $C_m(\alpha)$ (Fig. 5b), we estimate $k^*_{crit} \approx 1.4$, which is in very good agreement with the measured instability threshold of $k^*_{crit} \approx 1.37$ (Fig. 6). The analysis also predicts that k^*_{crit} is independent of damping and inertia, and this was confirmed in our experiments (as long as the damping is not too large). From a dynamical systems perspective, the system experiences a subcritical pitchfork bifurcation at the static torsional divergence. At this instance the stable fixed point transforms into a saddle point and two additional unstable equilibria (spiral points) are created at positive and negative values of α. Subsequently the system undergoes a saddle-node bifurcation that ultimately gives rise to a stable asymmetric LCO (Strogatz, 1994). We believe that the interaction between the static divergence and dynamic stall is responsible for the generation of these small asymmetric LCOs; this assertion is reinforced by the fact that the plate oscillates in and out of the static stall angle of $\alpha \approx 0.12$. Our experimental observations and theoretical analysis are also in agreement with those of Dimitriadis and Li (2009) in which the onset of small asymmetric LCOs was also seen just past the static divergence condition. The pitching frequency of the small-amplitude asymmetric LCOs (Fig. 7b, Region II) was difficult to measure accurately due to the fact that the oscillations are irregular. However, to the extent that they could be characterized, they were observed to be approximately 20–40% lower than the natural structural frequency of the plate.

As $1/k^*$ continues to rise, we observe an abrupt transition to large-amplitude symmetric LCOs which we term Region III (Fig. 6). The transition occurs immediately upon crossing the critical value of $1/k^*$, with the oscillation amplitude growing exponentially in time from its small-amplitude state in Region II to the large-amplitude state characteristic of Region III (Fig. 6). A representative transient response is depicted in Fig. 8, where the exponentially growing amplitude is limited presumably by unsteady separated flows at large angle of attack. This self-limiting amplitude oscillation is a unique characteristic of the dynamic stall flutter phenomenon, which is caused by the periodic separation and reattachment of the flow around the unsteady plate immersed in a uniform free-stream (McCroskey, 1982). As the phase portrait indicates (Fig. 6), this transition bears all the hallmarks of a subcritical Hopf bifurcation (Strogatz, 1994), illustrating an abrupt transition to the large amplitude state, and a hysteretic return to the stationary state if one were to increase the stiffness (i.e. decrease $1/k^*$) while in large amplitude regime. As shown in Fig. 6, large amplitude LCOs will persist until the system encounters a saddle-node bifurcation at $1/k^* \approx 0.3$, where the stable and unstable LCOs coalesce. A similar hysteretic behavior has been also observed by a number of investigators (e.g., Razak et al., 2011; Amandolese et al., 2013; Kim et al., 2013), although the ranges of the hysteresis reported in these studies are generally smaller than what we observed in the present study. In Region III, the oscillations are symmetric about $\alpha = 0$ and have a nearly sinusoidal character with a well-defined frequency. We find that, over a very wide range of velocities, stiffness and (light) damping, the pitching frequency is very close to, but always slightly lower than, the natural structural frequency of the plate (Fig. 9). In this regime, any large-scale vortex formation and shedding that must accompany these huge amplitude excursions is driven by the structural dynamics but does not influence the overall pitching frequency. An explanation for the observation that the pitching frequency is consistently below the natural frequency might be that the vortex that forms at the leading edge of the plate as it pitches up applies an aerodynamic torque to the plate and serves to reduce the effective stiffness of the torsional spring, thus lowering the effective natural frequency. This hypothesis will be revisited in Section 3.3.2.

3.3.2. *Aerodynamic torque, energy harvesting and Reynolds number effects*

Fig. 10 shows a representative projection of the phase plane trajectory, plotted over approximately 10 oscillation cycles. A typical phase plot of the moment, τ_f, versus the angle, α, exhibits regions of both positive and negative hysteresis. A positive hysteresis implies net positive energy exchange between the fluid and the plate, in which the energy is extracted from the fluid and dissipated (or harvested) by the cyber-physical system. In contrast, negative hysteresis implies that the energy is being transferred from the system into the wake. The measured static moment coefficient curve is drawn in blue for comparison.

Several features are worth discussing. Starting at the equilibrium position of $(\alpha = 0, \tau_f = 0)$, we see that, as the plate pitches up, the torque rises, but, curiously, at a slower rate than that predicted by the static $C_m(\alpha)$ curve. This suggests that a dynamically generated flow structure, possibly a vortex on the pressure side of the plate that has survived from the previous cycle, is resisting the positive rotation of the plate with a small clockwise torque. This idea is supported by the observation (not shown here) that, for lower values of k^* where the pitching frequency is lower and unsteady effects presumably weaker, the dynamic torque-angle trajectory falls closer to the statically measured $C_m(\alpha)$ curve.

As the plate continues to pitch up, the aerodynamic torque continues to grow well beyond the static stall angle finally reaching a maximum value that far surpasses its static counterpart. This is a classic example of "dynamic stall", in which the force and torque on the plate is strongly affected by the formation and growth of a strong leading-edge vortex (LEV) that develops on the suction side of the plate (e.g., McCroskey, 1982; Ohmi et al., 1991; Baik et al., 2012; Ford and Babinsky, 2013; Granlund et al., 2013). The torque reaches a maximum, after which it begins a precipitous decline, starting roughly at $\alpha \approx 0.7$, suggesting a stall condition most likely caused by the separation of the LEV. A precise definition of LEV "separation" is elusive in the literature, and the question still remains to be answered whether the LEV pinch off coincides with the aerodynamic force peak, as discussed by Granlund et al. (2013). Despite this drop in torque, the plate continues to rotate (due to its inertia), eventually coming to a rest at $\alpha \approx 1.5$. At this position, we observe a second increase in the aerodynamic torque which we hypothesize is due to the development of a second vortex forming as the shear layer shed from the leading

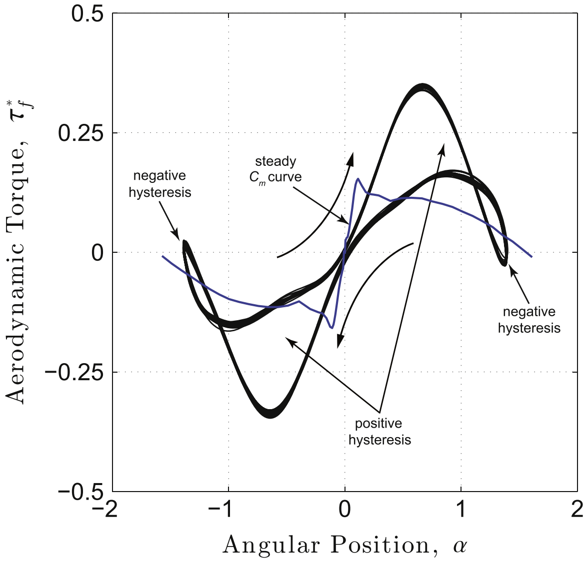

Fig. 10. Aerodynamic torque versus angular position phase portrait near the peak power coefficient. $Re = 9.9 \cdot 10^4$, $k^* = 0.78$, $b^* = 0.13$, $I^* = 10.6$, and $\alpha_0 = 0$. Curved arrows indicate the direction of the hysteresis. The mean steady moment coefficient curve is also plotted for comparison. The maximum aerodynamic torque induced by the pitching plate greatly exceeds its static counterpart; the aerodynamic torque continues to increase well beyond the static stall angle of $\alpha \approx 0.12$.

DISTRIBUTION A: Distribution approved for public release.

edge rolls up in the vicinity of the plate's upper surface. At this extreme angle of rotation, the structure's torsional spring exerts a strong torque which pulls the plate back towards its equilibrium position. However, as the plate starts its return, a small region of negative hysteresis is observed owing to the fact that the plate's return motion is hampered by the aerodynamic counter-torque induced by the second vortex. As the angle of incidence becomes small, we anticipate that the flow over the plate to temporarily reattach to the surface and the aerodynamic torque returns to zero. Due to the symmetry of the configuration, the pattern repeats during the second half of the cycle.

The net aerodynamic work per oscillation cycle can be determined by calculating the area enclosed by the $\tau_f - \alpha$ hysteresis loop

$$W = \frac{1}{N}\int_{\alpha(t_o)}^{\alpha(t_o+NT)} \tau_f \, d\alpha = \frac{1}{N}\int_{t_o}^{t_o+NT} \tau_f \dot{\alpha} \, dt. \tag{8}$$

where T is the cycle period, and N is an integral number of cycles. The integration was performed by employing a trapezoidal integration scheme with a time step of 0.25 ms using 30 s of recorded data ($N \approx \mathcal{O}(10^2)$). The power coefficient, C_p, is simply the energy per cycle, W, multiplied by the pitching frequency and appropriately normalized

$$C_p = WT \Big/ \frac{1}{2}\rho U_\infty^3 ch. \tag{9}$$

Fig. 11 shows contour plots of the power coefficient at three different Reynolds numbers. The power coefficient is characterized over a range of dimensionless stiffness and damping. First, we note that the magnitude of the power coefficient remains approximately independent of Reynolds number, reaching a maximum value of approximately 1.2%. Secondly the range of k^* over which power generation is achieved is also approximately constant with Reynolds number with the optimal stiffness for power generation located slightly lower than unity. Both of these results confirm that the inertial scaling chosen to describe the physics of these large scale oscillations is appropriate for this problem. Nevertheless, there is an observable effect of Reynolds number. As Re increases, larger values of structural damping, b^*, can be employed while still maintaining large scale motion to extract energy from the flow. It is, nevertheless interesting that despite using larger values of b^*, the power coefficient does not increase appreciably. This is likely due to the fact that although more energy per cycle is being harvested (recall that the structural damping is the mechanism by which energy is harvested from the fluid), the pitching frequency and the amplitude are reduced. The phase portraits of torque, τ_f, versus position, α, associated with two different Reynolds numbers and two different damping coefficients are shown in Fig. 12. In each case, k^* and I^* were held constant. The corresponding cases are shown using a green triangle and circle in Fig. 11. For a moderately low damping case (Fig. 12a, and the circles in Fig. 11), one can see that the shape and the size of the hysteresis trajectories are very similar; consequently the dimensionless pitching frequency, amplitude, and power coefficient scale very well at two different Re values. On the contrary, the Reynolds number effect appears to become more prominent at a higher dimensionless damping value, as depicted in Fig. 12b (the triangles in Fig. 11). We can clearly see that not only the maximum pitching amplitude is increased, but also the plate experiences slightly larger aerodynamic torque. The high Reynolds number case generates a much higher power coefficient (0.0092 vs. 0.0054) and has a much higher pitching frequency (7.1 Hz vs. 4.5 Hz). Since the structural characteristics of the system are identical, the difference between the two system's behavior must lie in the fluid behavior and faster generation of a stronger and more stable LEV is likely responsible for the augmentation in the aerodynamic torque and pitching amplitude. Velocity measurements are needed to properly identify these effects, something beyond the scope of this paper.

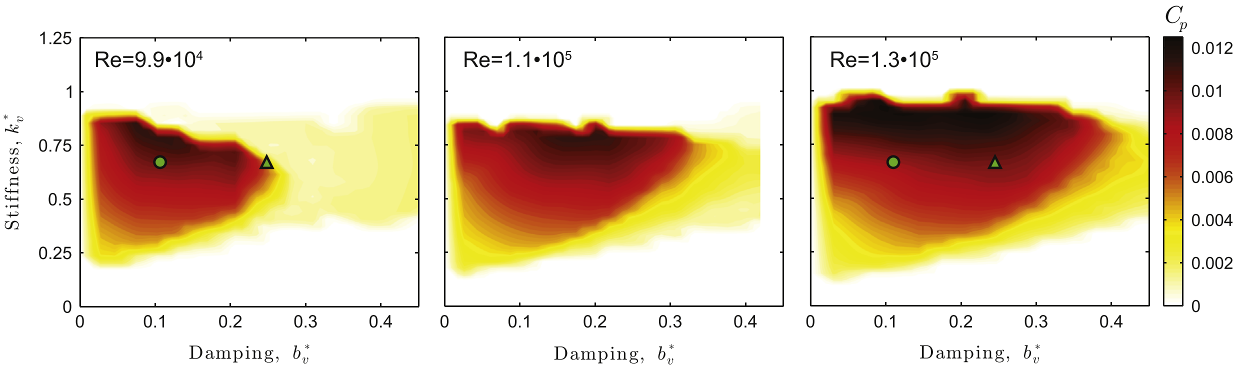

Fig. 11. The power coefficient contour plots for various Reynolds numbers: (left) $Re = 9.9 \cdot 10^4$, (center) $Re = 1.1 \cdot 10^5$, and (right) $Re = 1.3 \cdot 10^5$. The normalized mass moment of inertia, I^*, is 10.6. The ○ and △ represent low and high damping cases, respectively, whose corresponding aerodynamic torque versus angular position phase plane trajectories are illustrated in Fig. 12. The contours are constructed using linear interpolation.

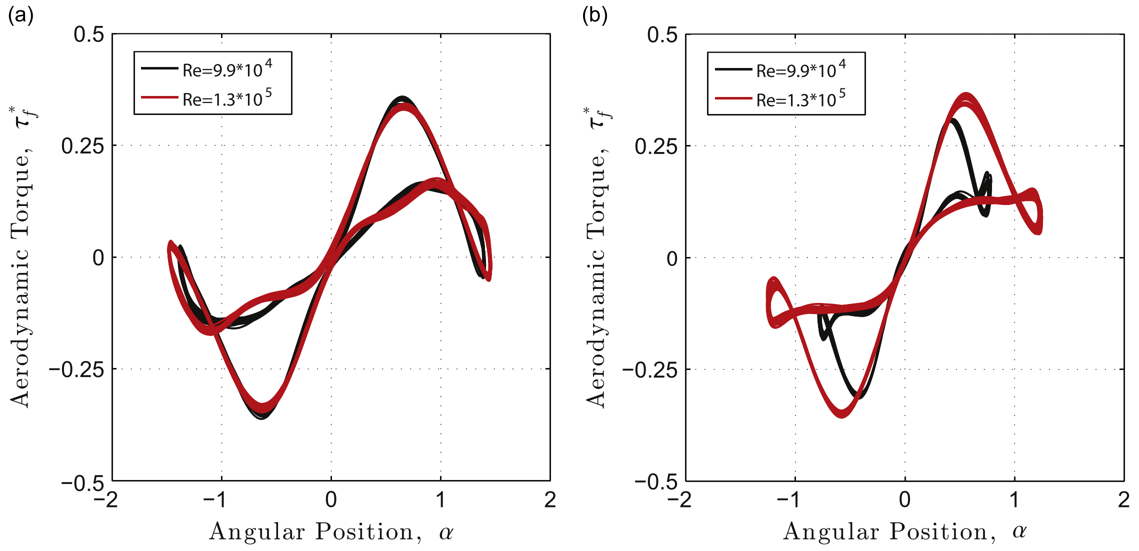

Fig. 12. Changes in the normalized aerodynamic torque versus angular position hysteresis curves at two distinct Reynolds numbers ($Re = 9.9 \cdot 10^4$ and $Re = 1.3 \cdot 10^5$) for two different values of the dimensionless damping: (a) $b^* = 0.11$ and (b) $b^* = 0.23$. In both cases, the dimensionless mass moment of inertia and torsional stiffness were, respectively, $I^* = 10.6$ and $k^* = 0.68$. The data are plotted over several cycles. Cases (a) and (b) are designated with ○ and ▵, respectively, in Fig. 11.

3.3.3. *Energy harvesting enhancement using a nonlinear (Cubic) spring*

Perhaps the most appealing aspect of the cyber-physical system is that it enables the user to easily explore the impact of structural nonlinearities (i.e, nonlinear elastic and damping forces) on the fluid–structure interactions. In this section, we demonstrate the implementation of a simple nonlinear cubic spring, and show how it can be utilized to improve the energy extraction capacity of the system. The nonlinear elastic torque, τ_v is modeled as

$$\tau_v = \kappa_1 \alpha + \kappa_3 \alpha^3 \tag{10}$$

where κ_1 and κ_3 are the linear and cubic spring constants, respectively. In this example, we wish to model a hardening cubic spring with values of $\kappa_1 = 0.58$ and $\kappa_3 = 0.42$. In this way, the nonlinear spring has similar characteristics to the original linear spring for small angular displacement (Fig. 13a). With the installment of the cubic spring, the dimensionless pitching frequency and the power coefficient increased by 37.5% and 57.0%, respectively. The phase portraits of τ_f versus α associated with the two distinct springs are presented in Fig. 13b and can be used to explain these changes. One can clearly observe

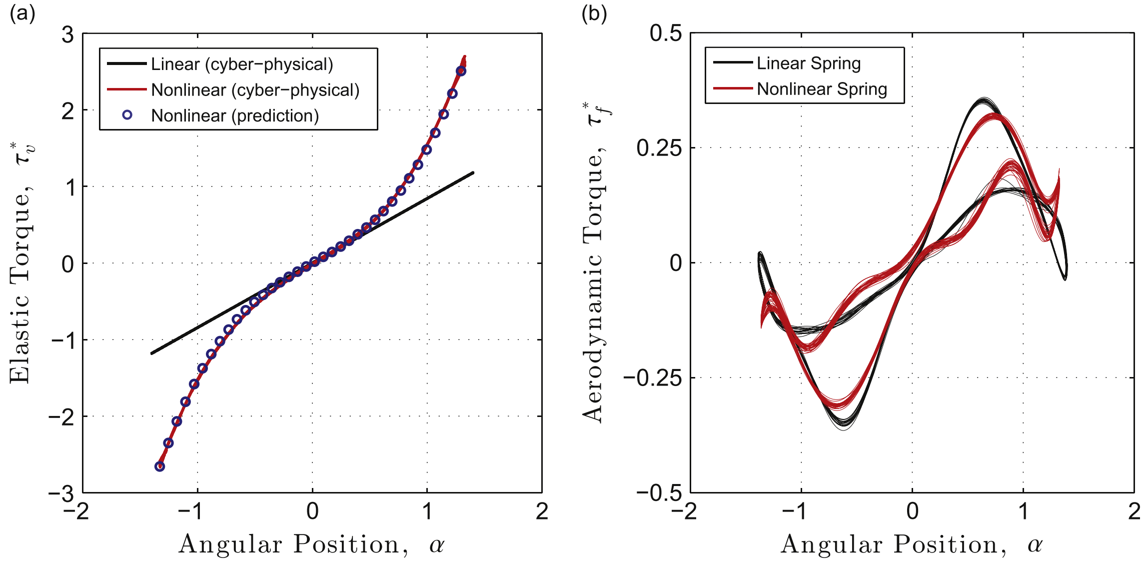

Fig. 13. (a) Dimensionless elastic torque as a function of angular displacement for a linear and nonlinear springs. Elastic torque was measured experimentally. (b) Aerodynamic torque versus angular position phase portraits for linear and cubic springs. $Re = 9.9 \cdot 10^4$, $b^* = 0.13$, $I^* = 10.6$, and $\alpha_0 = 0$. The values of spring constants associated with a cubic spring (as defined by Eq. (10)) are $\kappa_3 = 0.42$ and $\kappa_1 = 0.58$. The linear spring constant equals κ_1.

that, by implementing a simple cubic spring, the regions of negative hysteresis typically observed during the pitch reversal have been significantly reduced, and the maximum pitching amplitude has been decreased by roughly 12%. More importantly, by increasing the elastic restoring force at maximum rotation, the plate is forced to spring back faster (hence the higher pitching frequency) and we hypothesize that this reduces the time available for the second (and detrimental) vortex to form at the leading-edge, thus eliminating the negative hysteresis. This hypothesis is yet to be confirmed (using velocity measurements).

4. Concluding remarks

The work presented here demonstrates a number of advances. We have successfully demonstrated the use of a cyber-physical system to accurately and easily simulate a wide range of structural dynamics. In the current work we have not implemented any virtual modification of the plate's inertia, and have restricted the study to a single degree of freedom motion. However, both these are easy to implement, and despite the initial complexity of the cyber-physical system setup, the key benefit—that of rapid and extensive access to the entire fluid-structural parameter space—is the ability to perform a very deep study of the physics of fluid–structure interactions. Unlike previous cyber-physical systems (Hover et al., 1997; Lee et al., 2011; Mackowski and Williamson, 2013) that operate in water at low frequencies, our system operates in air at high operational frequencies and with much larger and more violent structural motion.

Nevertheless, the purpose of implementing the cyber-physical system is not only as a technical demonstration, but rather to enable the exploration and detailed characterization of fluid–structure interactions and here too we have presented several novel insights. Although the onset of the small-amplitude nonlinearly stabilized oscillations (Region II) has been widely explored, dating back to Theodorsen, the large-amplitude motion (Region III) has not been well characterized, and the current data provides valuable insight into this regime. The pitching moment associated with the large scale unsteady motion is greatly enhanced, with torques nearly three times as large as those associated with quasi-steady motion. These forces are achieved, presumably, by the dynamics of the leading-edge vortex that forms at the sharp leading edge of the plate, and the cyber-physical system can be tailored using the characteristics of the torsional spring, to modify the interaction between the vortex and the structure. Furthermore, by monitoring the phase plane representation of the structural motion, we can follow the formation time and separation dynamics of these leading-edge structures and identify timescales as a function of Reynolds number. Finally, from the perspective of energy harvesting, with efficiencies of only one or two percent, the pitching plate is a poor choice if one seeks efficient extraction of energy from the free stream. The pitching-plunging plate studied by several other researchers (see, e.g., Dumas and Kinsey, 2006; Simpson et al., 2008; Peng and Zhu, 2009) is much more effective since it can take advantage of the aerodynamic lift during the heave motion to extract significant energy from the flow. It is not our intent to propose an efficient energy harvesting system, but rather to gain perspective on the dynamics of energy flow in a simplified physical system, and here a key insight gained from the present study is the role that the torsional spring stiffness plays in establishing feedback between the fluid and the structure, the role of damping in moderating that feedback, and the appropriate scaling of the stiffness and damping necessary for maximum energy extraction performance for a given flow condition. A hysteretic behavior of an aeroelastic energy harvesting system is beneficial in real applications as it serves to expand the operational regime for power generation. The implementation of such devices in real applications poses enormous challenges owing to difficulty in tuning the system's structural characteristics to realize stable and efficient power generation. One possible solution is to implement a cyber-physical system, coupled with an optimization scheme, as a means to automate the modulation of the structural parameters.

Moving forward, the insight gained from the phase portraits, in particular with regard to the behavior of the separated flow structures, must be confirmed and quantified directly, and the next phase of the research will include velocimetry (using Particle Image Velocimetry), coupled to measurements of the plate motion. We believe that the results from these experiments will shed more insight on the physics of the fluid–plate interactions and the process of energy transfer from the fluid to the structure.

Acknowledgments

This research is funded by the Air Force Office of Scientific Research (AFOSR) Grant number FA9550-12-1-0099, monitored by Dr. Douglas Smith. We would like to acknowledge the members of the Breuer Lab and the Energy Harvesting group for fruitful discussions and advice. A more limited version of this paper was presented at the 2014 AIAA SciTech conference.

References

Amandolese, X., Michelin, S., Choquel, M., 2013. Low speed flutter and limit cycle oscillations of a two-degree-of-freedom flat plate in a wind tunnel. Journal of Fluids and Structures 43, 244–255.

Baik, Y., Bernal, L., Granlund, K., Ol, M., 2012. Unsteady force generation and vortex dynamics of pitching and plunging aerofoils. Journal of Fluid Mechanics 709, 37–68.

Bernitsas, M.M., Raghavan, K., Ben-Simon, Y., Garcia, E.M.H., 2008. Vivace (vortex induced vibration aquatic clean energy): a new concept in generation of clean and renewable energy from fluid flow. Journal of Offshore Mechanics and Arctic Engineering—Transactions of the Asme 130 (November (4)), 041101.
Bisplinghoff, R.L., Ashley, H., Halfman, R.L., 1957. Aeroelasticity. Addison-Wesley Publishing Co. Inc., Cambridge, MA.
Blevins, R.D., 1990. Flow-Induced Vibrations. Van Nostrand Reinhold, New York.
DeVoria, A.C., Ringuette, M.J., 2012. Vortex formation and saturation for low-aspect-ratio rotating flat-plate fins. Experiments in Fluids 52, 441–462.
Dimitriadis, G., Li, J., 2009. Bifurcation behavior of airfoil undergoing stall flutter oscillations in low-speed wing tunnel. AIAA Journal 47 (11), 2577–2596.
Dukkipati, R.V., 2004. Vibration Analysis. Alpha Science International Ltd, United Kingdom.
Dumas, G., Kinsey, T., 2006. Eulerian simulations of oscillating airfoils in power extraction regime. Advances in Fluid Mechanics VI, 245.
Fage, A., Johansen, F.C., 1927. On the flow of air behind an inclined flat plate of infinite span. Proceedings of the Royal Society of London A 116, 55.
Ford, C.W.P., Babinsky, H., 2013. Lift and the leading-edge vortex. Journal of Fluid Mechanics 720, 280–313.
Frayne, S.M., Jul. 26 2011. Energy Converters Utilizing Fluid-Induced Oscillations. US Patent 7,986,051. URL ⟨https://www.google.com/patents/US7986051⟩.
Gharib MR. Vortex-induced vibration, absence of lock-in, and fluid force deduction [Ph.D. thesis]. California Institute of Technology; 1999.
Granlund, K.O., Ol, M.V., Bernal, L.P., 2013. Unsteady pitching flat plates. Journal of Fluid Mechanics 733. R5.1–13.
Hover, F., Miller, S., Triantafyllou, M.S., 1997. Vortex-induced vibration of marine cables: experiments using force feedback. Journal of Fluids and Structures 11, 307–326.
Jantzen, R.T., Taira, K., Granlund, K., Ol, M.V., 2014. Vortex dynamics around pitching plates. Physics of Fluids 26, 053606.
Khalak, A., Williamson, C.H.K., 1999. Motions, forces and mode transitions in vortex-induced vibrations at low mass-damping. Journal of Fluids and Structures 13, 813–851.
Kim, D., Cossè, J., Cerdeira, H.C., Gharib, M., 2013. Flapping dynamics of an inverted flag. Journal of Fluid Mechanics 736http://dx.doi.org/10.1017/jfm.2013.555.
Lee, J., Bernitsas, M., 2011. High-damping, high-Reynolds viv tests for energy harnessing using the vivace converter. Ocean Engineering 38, 1697–1712.
Lee, J., Xiros, N., Bernitsas, M., 2011. Virtual damper–spring system for viv experiments and hydrokinetic energy conversion. Ocean Engineering 38, 732–747.
Mackowski, A.W., Williamson, C.H.K., 2011. Developing a cyber-physical fluid dynamics facility for fluid–structure interaction studies. Journal of Fluids and Structures 27, 748–757.
Mackowski, A.W., Williamson, C.H.K., 2013. An experimental investigation of vortex-induced vibration with nonlinear restoring forces. Physics of Fluids 25, 087101.
McCroskey, W.J., 1982. Unsteady airfoils. Annual Review of Fluid Mechanics 14, 285–311.
Ohmi, K., Coutanceau, M., Daube, O., Loc, T.P., 1991. Further experiments on vortex formation around an oscillating and translating airfoil at large incidences. Journal of Fluid Mechanics 225, 607–630.
Ol, M.V., Altman, A., Eldredge, J.D., Garmann, D.J., Lian, Y.,Summary of progress on pitching plates: canonical problems in low-re unsteady aerodynamics. AIAA Paper, 2010-1085; 2010.
Pelletier, A., Mueller, T.J., 2000. Low Reynolds number aerodynamics of low-aspect-ratio thin/flat/cambered-plate wings. Journal of Aircraft 37 (5), 825–832.
Peng, Z., Zhu, Q., 2009. Energy harvesting through flow-induced oscillations of a foil. Physics of Fluids 21 (12).
Razak, N.A., Andrianne, T., Dimitriadis, G., 2011. Flutter and stall flutter of a rectangular wing in a wind tunnel. AIAA Journal 49 (11), 2258–2271.
Rival, D., Prangemeier, T., Tropea, C., 2009. The influence of airfoil kinematics on the formation of leading-edge vortices in bio-inspired flight. Experiments in Fluids 46, 823–833.
Shiels, D.,Simulation of controlled bluff body flow with a viscous vortex method [Ph.D. thesis]. California Institute of Technology; 1998.
Simpson, B., Licht, S.0, Hover, F.S., Triantafyllou, M.S., Energy extraction through flapping foils. In: Proceeding of the 27^{th} International Conference on Offshore Mechanics and Arctic Engineering, OMAE27; 2008.
Song, A., 2013. Aeromechanics of highly compliant structures: bat wings, compliant membranes and flexibly mounted flat plates. Ph.D. thesis, Brown University.
Song, A., Tian, X., Israeli, E., Galvao, R., Bishop, K., Swartz, S., et al., 2008. Aeromechanics of membrane wings with implications for animal flight. AIAA Journal 46, 2096–2106.
Strogatz, S.H., 1994. Nonlinear Dynamics and Chaos: With Applications to Physics, Biology, Chemistry, and Engineering. Perseus Books, Cambridge, Massachusetts.
Theodorsen, T., General theory of aerodynamic instability and the mechanism of flutter. NASA technical report 496; 1935.
Wojcik, C.J., Buchholz, J.H.J., 2014. Vorticity transport in the leading-edge vortex on a rotating blade. Journal of Fluid Mechanics 743, 249–261.
Yu HT, Bernal LP. Effect of pivot point on aerodynamic force and vortical structure of pitching flat plate wings. AIAA Paper, 2013–0792; 2013.
Zhu, Q., Peng, Z., 2009. Mode coupling and flow energy harvesting by a flapping foil. Physics of Fluids 21 (29).

DISTRIBUTION A: Distribution approved for public release.

Vortex formation and shedding from a cyber-physical pitching plate

Kyohei Onoue[1]† and Kenneth S. Breuer[1]

[1]School of Engineering, Brown University, Providence, RI 02912, USA

(Received ?; revised ?; accepted ?. - To be entered by editorial office)

We report on the dynamics of the formation and growth of the leading-edge vortex and the corresponding unsteady aerodynamic torque induced by large-scale flow-induced oscillations of an elastically mounted flat plate. All experiments are performed using a high-bandwidth cyber-physical system, which enables the user to access a wide range of structural dynamics using a feedback control system. A series of 2D particle image velocimetry is carried out to characterize the behaviour of the separated flow structures and its relation to the plate kinematics and unsteady aerodynamic torque generation. By modulating the structural properties of the cyber-physical system we systematically analyse the formation, strength, and separation of the leading-edge vortex, and the dependence on kinematic parameters. We demonstrate that the leading-edge vortex growth and strength scale with the characteristic shear-layer feeding velocity and that a potential flow model using the measured vortex circulation and position can, when coupled with the steady moment of the flat plate, accurately predict the net aerodynamic torque on the plate. Connections to previous results on optimal vortex formation time are also discussed.

Key words: Leading-edge vortex, flow-induced oscillations, cyber-physical system

1. Introduction

Characterization of unsteady leading-edge vortex (LEV) dynamics associated with separation from bodies at high angles of attack has been a problem of scientific interest for decades. The importance of LEV formation (the hallmark of dynamic stall) in relation to force augmentation is well documented in the archival literature, often in the context of biological flight (Ellington *et al.* 1996), the dynamics of highly maneuverable aircraft (Ol *et al.* 2010) and, more recently, energy conversion applications (Peng & Zhu 2009; Ramesh *et al.* 2015; Onoue *et al.* 2015).

A number of studies that imposed predefined wing kinematics to characterize the LEV formation have demonstrated that the behaviour of the separated flow structures is quite sensitive to variations in wing kinematics (Kim & Gharib 2010; Baik *et al.* 2012; Ozen & Rockwell 2012), pivot axis location (Yu & Bernal 2013; Granlund *et al.* 2013), wing geometry (Yilmaz & Rockwell 2012; Hartloper & Rival 2013), and Reynolds numbers (Jantzen *et al.* 2014). For this reason, it poses an enormous challenge to find unifying scaling principles for the LEV formation time, strength and stability that can be generalized to arbitrary problems. One promising approach uses the so-called “universal vortex formation number”(originally introduced by Gharib *et al.* (1998)), which can be

---

† Email address for correspondence: kyohei_onoue@brown.edu

DISTRIBUTION A: Distribution approved for public release.

extended to a wide variety of vortical flows; Dabiri (2009) defined the formation number based on the feeding shear-layer velocity and the characteristic length of the vortex generator. The premise of this universal vortex formation number is that the dimensionless dynamic formation time corresponding to the generation of a maximum-strength vortex remains constant at a value of about 4, at which time the vortex rejects additional entrainment of vorticity from the shear layer and pinches off. Measurements by Rival *et al.* (2009) have demonstrated that the formulation of Dabiri (2009) provides a good scaling for the maximum LEV circulation generated by an aerofoil executing sinusoidal plunging motions. The use of feeding-shear layer velocity to scale LEV circulation seems to be a logical choice given that the vortex growth is dictated by the transport of circulation flux into the vortex core through the feeding shear-layer, as suggested by Sattari *et al.* (2012). More recently, Kriegseis *et al.* (2013) measured the LEV circulation and unsteady forces acting on a flat plate undergoing accelerating plunging and towing motions at a fixed angle of attack. The authors have demonstrated that the LEV circulation and hydrodynamic forces can be effectively normalized by the characteristic shear-layer velocity, $U_{eff} = U_\infty + \dot{h}$, where $\dot{h}$ designates the towing or plunging velocity. Buchholz *et al.* (2011) has proposed an alternative scaling for the total spanwise circulation shed by a periodically pitching rectangular plate about its leading edge. This scaling parameter is formulated based on a dynamic pressure associated with the maximum transverse velocity of the trailing edge and the plate geometry. The authors have demonstrated that their scaling parameter can be used to satisfactorily collapse the vortex circulation data for different aspect ratios and pitching amplitudes. However, it still remains to be verified whether the aforementioned scaling relations are robust enough to collapse the LEV circulation histories, both in magnitude and time, throughout the entire vortex growth phase.

While these studies have used proscribed kinematics to generate LEVs, in real systems, the vortex structures are often a result of fluid structure interactions, in which the structural dynamics of an elastically-supported aerodynamic surface (for example a flat plate) are driven by the growth, evolution and shedding of strong LEVs. As discussed in Onoue *et al.* (2015), such aeroelastic interactions often result in non-destructive limit-cycle oscillations (LCOs) with a nearly constant amplitude and frequency, which can potentially serve as the basis for the passive power generation. While previous studies on dynamic-stall flutter have provided a wealth of information with regard to the instability boundaries, local bifurcation behaviours, and amplitude of LCOs with variations in flow speed and structural characteristics (Amandolese *et al.* 2013; Poirel & Mendes 2014; Onoue *et al.* 2015), a direct connection between the large amplitude oscillations and the vortical structures generated by the violent motion of the structure has not yet been made. Onoue *et al.* (2015) measured the aerodynamic torque as a function of the plate motion, from which a plausible description of vortex formation, growth and separation can be inferred, but without measurements of the velocity field, it is impossible to develop robust aerodynamic models that allow us to characterize, and thus predict, the detailed behaviour of large-scale fluid-structure interactions (and positive energy harvesting).

The measurements and analyses presented in the current manuscript provide this valuable connection between the vortex dynamics and aerodynamic loads, and in this study, we take advantage of the cyber-physical experimental setup in conjunction with synchronized PIV to carry out a detailed study of the flow physics associated with a rapidly pitching plate in a uniform airflow. As described in Onoue *et al.* (2015), the cyber-physical system is one in which the structural dynamics (torsional spring stiffness, damping and mass moment of inertia) are emulated using a digital controller rather than by physical hardware. By being able to directly control the structural properties of the system,

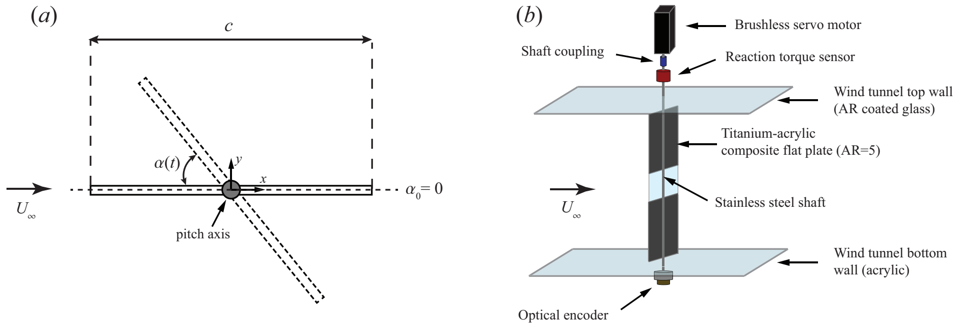

FIGURE 1. (a) schematic of an oscillating flat plate with a pitch axis located at the mid chord. The dashed horizontal line designates the equilibrium angle of attack, α_0=0. (b) A computer–controlled servo motor rotates the shaft-plate assembly by applying a specific torque calculated via numerical simulation to achieve the desired structural dynamics. See Onoue *et al.* (2015) for detailed descriptions of the cyber-physical system control algorithm.

the user can systematically tune the fluid-structure interaction parameters while completely isolating the effects of Reynolds number, and hence the pure fluid effects. The use of cyber-physical system was first demonstrated by Hover *et al.* (1997), who successfully implemented a force-feedback algorithm to impose arbitrary structural forces in the study of vortex-induced vibration (VIV) of marine cables. In recent years, several cyber-physical systems have been successfully employed in VIV energy harvesting investigations (Lee & Bernitsas 2011; Mackowski & Williamson 2013). While all of these cyber-physical systems have been designed to be operated in water at relatively low frequencies, our cyber-physical system operates in air (where the plate inertia is more important), at higher frequencies and with much more violent structural motions (Onoue *et al.* 2015).

The primary objectives of the current study are two-fold: (1) to determine the scaling relation for the LEV growth rate and circulation on a rapidly pitching flat plate, and (2) to elucidate the linkage between the LEV dynamics and the aerodynamic forces and moment that the flow imparts on the elastic structure.

2. Experimental techniques

Experiments were conducted in a closed-return wind tunnel with a test section of 0.6 m in width, 0.6 m in depth, and 1.2 m in length. The turbulence level in the wind tunnel was previously measured to be less than 0.1% of the free-stream velocity (Song *et al.* 2008). Figure 1(a) illustrates a flat plate, with chord, c, span, h and thickness, δ, free to rotate about its mid-chord in a uniform airflow of magnitude, U_∞, and density, ρ_f. In the present study, the Reynolds numbers based on the chord length, $Re = U_\infty c/\nu$, were in the order of $O(10^4)$ to $O(10^5)$, where ν is the kinematic viscosity of the fluid. Since the chord represented no more than 17% of the test section width, blockage and side-wall boundary layer effects were deemed insignificant.

Figure 1(b) shows a schematic of the experimental configuration used in the current study, illustrating the flat plate mounted to a virtual mass-spring-damper system in the wind tunnel test section. Instead of using a physical torsional spring and damper, the structural stiffness and damping characteristics of the pitching plate were controlled using a cyber-physical system that consists of a computer-controlled servomotor (SM233AE, Parker Compumotor, Rohnert Park, CA), torque sensor (TFF400, Futek, Irvine, CA), and rotary encoder (HB6M Optical Encoder, US Digital, Vancouver, WA) coupled to a real-time digital controller operating in a feedback loop. The cyber-physical system also

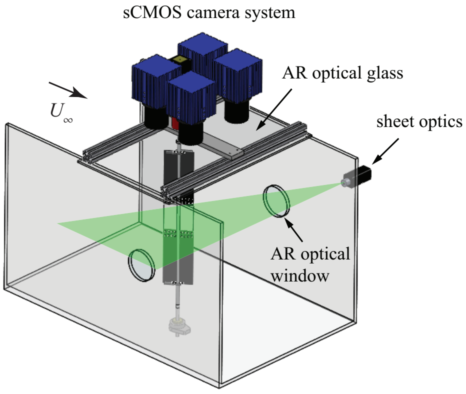

FIGURE 2. Experimental setup for the PIV measurements in the streamwise plane at the midspan location.

allows for the virtual modification of the structural mass moment of inertia. The digital control system (Simulink, Mathworks, Natick MA) samples the angular position signal, $\alpha(t)$, from the optical encoder at 4 kHz, and numerically calculates the velocity, $\dot{\alpha}(t)$ and acceleration, $\ddot{\alpha}(t)$, in real-time via custom-designed FIR differentiators with a linear-phase response in the pass-band. These signals are then multiplied by the user-specified stiffness, k_v, damping, b_v, and mass moment of inertia, I_v, coefficients, respectively, where the subscript v denotes a virtual quantity. These signals are combined to determine the target motor torque, $\tau_m(t) = I_v\ddot{\alpha}(t) + b_v\dot{\alpha}(t) + k_v\alpha(t)$, which is applied to the servomotor. This torque is measured using the reaction torque sensor with a maximum measurement capacity of 7 N·m. In post-processing, the aerodynamic torque was determined from the equation of motion: $\tau_f(t) = I_p\ddot{\alpha}(t) + b_p\dot{\alpha}(t) + \tau_m(t)$, where the subscript p designates a physical quantity. A series of free-oscillation tests were conducted in air to deduce the value of physical mass moment of inertia, I_p, using the method of logarithmic decrement. These free-oscillation tests exhibit exponentially-decaying amplitude such that the effect of Coulomb damping (or dry friction) can be neglected. Therefore, the physical damping can be simply modelled as a linear function of velocity, $b_p\dot{\alpha}(t)$. The physical damping associated with the motor and bearing was determined by measuring the torque resulting from rotating the motor and shaft over a range of constant angular velocities, and fitting the linear regression line to the data. Finally, to evaluate the above equation for $\tau_f(t)$, the position and torque signals were filtered by employing a zero-phase, sixth order Butterworth low-pass filter with a cut-off frequency set to ten times the pitching frequency. Second-order accurate finite differences were used to evaluate the angular velocity and acceleration during post-processing. Hereinafter for simplicity, the effective torsional stiffness, damping and mass moment of inertia are denoted without any subscript, as k, b, and I, respectively.

The setup for the streamwise 2D PIV experiment is illustrated in figure 2. All PIV measurements were acquired in a streamwise plane located at the mid-span of the plate. The laser sheet was generated using a double-pulsed 200 mJ Nd:YAG laser (λ=532 nm) (EverGreen, Quantel USA, MT) with LaVision sheet optics. The thickness of the laser sheet was approximately 3 mm. The flow was seeded with oil droplets nominally 1 μm in diameter. The mid-span section of the plate is made out of clear anti-reflective acrylic which enabled PIV measurements from both sides of the structure. The particle images were acquired with four synchronized sCMOS cameras (LaVision) equipped with 50 mm lenses (Nikon). Each camera has a resolution of 2560 pixels x 2160 pixels and

DISTRIBUTION A: Distribution approved for public release.

the frame rate for image acquisition was 15 Hz. Velocity fields were calculated using DaVis 8.6 software (LaVision) by applying a sequential spatial cross-correlation with multi-pass iterations with decreasing window size (128x128, 2 iterations, 50% overlap to 32x32, 2 iterations, 50% overlap). Velocity fields acquired by four different cameras were stitched together by averaging the overlapped regions, yielding a composite field-of-view of approximately 0.25 m by 0.3 m containing over 63,000 vectors. For each PIV experiment, approximately 2500 composite image pairs were acquired, and subsequently allocated into 72 equally-spaced phase bins equally spaced over the oscillation cycle ($\Delta\phi$=5°). The instantaneous phase was calculated by taking the Hilbert transform of the angular position time history (Khalak & Williamson 1999).

In order to identify the vortical structures in the flow field, the vortex identification technique based on the vortex swirling strength was employed (Adrian *et al.* (2000)). The threshold was set to 10% of the maximum swirling vortex strength to isolate the vortices of interest from the low-level background noise. This threshold was appropriate to exclude the vorticity confined in the feeding shear-layer in the calculation of the primary vortex strength. The spanwise circulation of the primary vortex was calculated by integrating the simply connected vorticity patch about the vortex centroid using the Stokes' theorem. The results were insensitive to the threshold values in the range of 0.1±0.05. Another local vortex identification method (Q-criterion) was also tested, and was found to yield similar results. In addition, the Γ_1 criterion (Graftieaux *et al.* 2001) was employed to identify the location of the LEV centroid. In the present study, a threshold of $\Gamma_1 \geqslant 0.9$ was selected, and the vortex centre is found where the maximum spatial value of Γ_1 is achieved. This vortex identification method has been successfully implemented by numerous investigators (e.g., Baik *et al.* (2012); Jantzen *et al.* (2014)).

3. Results and discussion

3.1. *Phase-averaged swirl fields and τ_f vs. α phase portrait*

As mentioned earlier, the plate exhibits very large amplitude limit cycle oscillations (LCO) over a wide range of structural parameters, presumably, driven by the development, growth and separation of leading edge vortices. A representative sequence of phase-averaged swirl fields at several stages during the half cycle are presented in figure 3, along with the associated torque versus angular position phase portrait. As the plate begins to rise from its equilibrium position, $\alpha_0 = 0$ (figure 3: (1)), the aerodynamic torque increases, but interestingly the dynamic torque is *lower* than that predicted by the steady moment coefficient curve (also shown in figure 3), as discussed by Onoue *et al.* (2015). This is presumably due to the apparent generation of the vortices at the half-chord location as the boundary layer on the suction side of the plate separates from the rotating shaft (figure 3: (1)). This in turn generates a low pressure region over the rear-half of the plate, causing the centre of pressure to move further aft of the leading edge. Measurements over a wide range of conditions indicate that this effect is weaker at lower pitching frequencies, for which cases the aerodynamic torque-angle trajectory falls closer to the statically-measured $C_m(\alpha)$ curve. The torque offset at α=0 can be attributed to the separated flow on the lower side of the plate at the end of the previous cycle, which creates a pressure gradient in favour of generating an aerodynamic torque in the direction of the wing rotation.

As the angle of attack increases, the aerodynamic torque continues to grow well beyond the static stall angle finally reaching a maximum value nearly 2.5 times greater than its static counterpart (figure 3: (1)–(3)). This is a classic example of "dynamic stall"

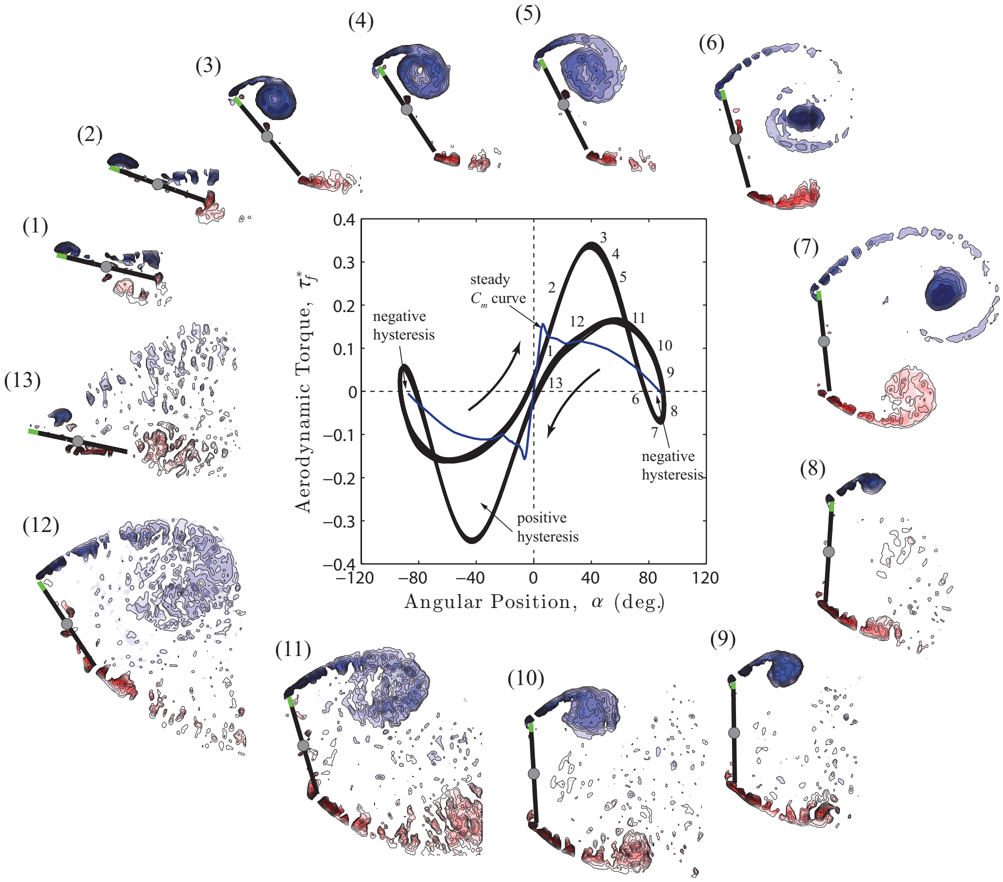

FIGURE 3. Snapshots of the phase-averaged swirl fields over a half cycle and the corresponding aerodynamic torque versus angular position phase portrait. Curved arrows indicate the orientation of the hysteresis trajectory. Regions of positive and negative hysteresis are shown; a positive hysteresis implies net positive energy exchange between the fluid and the plate and a negative hysteresis describes the amount of energy transferred from the system to the wake. The steady moment coefficient, C_m, is plotted with a blue curve. Re=$9.9 \cdot 10^4$; maximum pitching amplitude, $\Delta\alpha$=93 deg.; pitching frequency, f=5.6 Hz.

wherein the force and torque on the plate is significantly augmented by the formation and growth of a strong LEV on the suction side of the plate (McCroskey 1982). The LEV core continues to grow in size and strength as it entrains circulation of the small eddies generated at the leading edge. At the same time, a train of opposite-signed vortices is continuously shed from the trailing edge—a phenomenon that can be explained by the fact that the LEV circulation growth must be equalized by the flux of opposite circulation shed from the trailing edge so that the total circulation is conserved (i.e., Kelvin's circulation theorem). The formation of these discrete eddies has been commonly attributed to a Kelvin-Helmholtz-like instability inherent in the separated shear layer by numerous investigators (e.g. Baik *et al.* 2012; DeVoria & Ringuette 2012). The velocity shear arising from the high velocity of the impinging flow and the relatively low velocity of the separated free shear layer at the sharp-edges promotes instability in the shear layer, and therefore leads to the generation of the small-scale eddies. Moreover, the shedding

DISTRIBUTION A: Distribution approved for public release.

frequency associated with the small eddies is much higher than that of the primary vortices which is comparable with the pitching frequency.

The aerodynamic torque attains a maximum at $\alpha \approx 40°$ after which it immediately begins a precipitous decrease (figure 3: (4)). This torque decrement is not due to vortex leaving the plate, given that the attached LEV is evident at $\alpha \approx 63°$ (figure 3: (5)). Rather, we hypothesize that the saturation of the LEV circulation, and the movement of the vortex core closer to the mid-chord point are responsible for the decrease in the aerodynamic torque. This hypothesis will be revisited in §3.2 and §3.4. Despite this sharp drop in the aerodynamic torque, the plate continues to rotate (due to its inertia) until it comes to rest at a maximum pitch angle, in this particular case, approximately 90 degrees to the free stream direction. The shear-layer from the trailing edge begins to roll up and forms a trailing-edge vortex (TEV) (figure 3: (6)–(7)). This roll-up of the shear layer is presumably due to a global instability of the wake which includes the influence of the LEV passing just overhead. Another robust feature associated with the dynamics of a strong LEV is the generation of small discrete eddies surrounding the isolated LEV core in the wake, as clearly portrayed in figure 3: (7). These small eddies emerge as the vortex filament decays as a result of the Kelvin-Helmholtz instability (Gustafson & Albert 1991). Upon reaching a maximum angle of rotation, we observe a second increase in the aerodynamic torque owing to the development of a secondary vortex in the close proximity of the leading edge (figure 3: (8)–(10)). This secondary vortex is analogous to that observed by Ringuette *et al.* (2007), who examined the LEV formation on a flat plate undergoing a translating motion perpendicular to the incoming flow.

During the pitch reversal, a small region of negative hysteresis is observed due to the fact that the plate's return motion is hampered by the counter torque induced by the secondary vortex. For applications interested in energy harvesting, the negative hysteresis implies that the energy is being transferred from the system into the wake and represents a drop in harvesting efficiency. We also note that the secondary TEV develops as the shear layer emanating from the trailing edge curls up in the wake.

Finally, the elastic restoring toque of the torsional spring pulls the plate back to its equilibrium angle of attack (figure 3: (11)–(13)). Even at very small angle, the flow on the suction side of the plate does not completely reattach, and as mentioned eariler, this results in a vertical pressure gradient across the plate that gives rise to a finite torque at zero angle of attack. By symmetry, the pattern repeats during the second-half of the cycle.

3.2. *Leading-edge vortex dynamics*

In order to examine the effects of pitching frequency and amplitude on the ensuing LEV formation, let us consider four different cases of the reduced frequency. In this paper, the reduced frequency is defined as $f^* = \pi f c \Delta\alpha / 2U_\infty$, where f is the pitching frequency and $\Delta\alpha$ is the maximum pitching amplitude in radians. Note that $c\Delta\alpha/2$ represents the leading edge excursion as the plate rotates from α_0 to α_{max}, during which the LEV formation takes place. This amplitude-based reduced frequency describes the dynamic similarity between the leading-edge velocity, $f c \Delta\alpha/2$, and the characteristic flow velocity, U_∞, which resembles the inverse of the advance ratio parameter defined by Ellington (1984). It is obvious that in order to precisely characterize the wing-tip velocity, one must consider both pitching frequency *and* stroke amplitude—something not reflected in the traditional formulation of the reduced frequency, i.e., $\pi f c / U_\infty$. As will be discussed later, the wing-tip velocity has an important implication on the evolution of the LEV as it is intrinsically related to the feeding shear-layer velocity which regulates the advection of circulation into the vortex core. The pitching frequency and amplitude were modulated

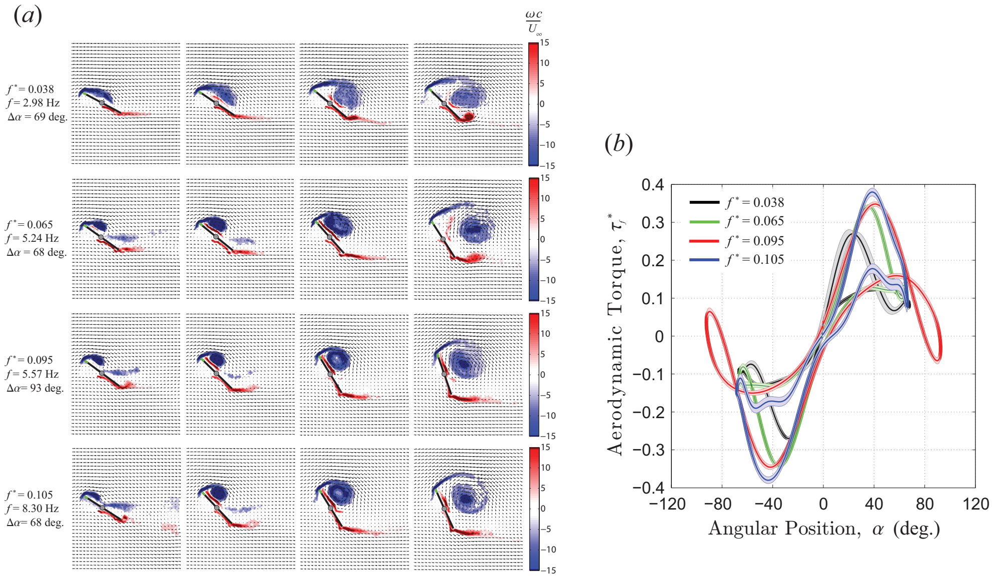

FIGURE 4. (a) Snapshots of the spanwise vorticity fields associated with various reduced frequencies (f^*=0.038 $\sim$ 0.105) at Re=9.9·10^4. The vorticity is scaled by c/U_∞: negative, clockwise (blue) and positive, counter-clockwise (red). (b) Corresponding aerodynamic torque versus angular position phase portraits. Shaded regions represent the standard deviation over several oscillation cycles. All experiments are performed at Re=9.9·10^4.

by tailoring the torsional stiffness and damping characteristics of the structure. In each case, the time history of the angular position revealed a very strong sinusoidal character with a nearly constant amplitude and a well-defined frequency such that the sinusoidal regression curve with a 95% confidence interval yielded an R-squared value greater than 0.99. The Reynolds number was held constant at 9.9·10^4 in all experiments.

A strong dependence of the reduced frequency (defined as $\pi f c/U_\infty$) on LEV circulation and resulting forces has been well documented (Ol *et al.* 2010; Baik *et al.* 2012; Granlund *et al.* 2013; Jantzen *et al.* 2014). For example, Baik *et al.* (2012) and Jantzen *et al.* (2014) concluded that the reduced frequency is the primary parameter governing the flow evolution and the unsteady force generation on a flat plate with sufficient forcing and large effective angle of attack. In contradiction to their findings, however, we found that the fluid behaviour becomes progressively similar as f^* increases and nearly independent of the reduced frequency for f^*>0.09, as can be inferred from figure 4(a). Moreover, the apparent self-similarity of the $\tau_f - \alpha$ phase trajectories for f^*>0.07 also reinforces this assertion (figure 4b), which further implies that the reduced frequency is not a sufficient scaling parameter for the characterization of the LEV and the accompanying aerodynamic torque. However, a similarity in the torque trajectories does not necessarily entail a similarity in the force curves, partly because the latter is independent of the location of the centre of pressure. Due to the fact that the pressure gradients acting on the plate account for a very large proportion of the resultant force, as noted by Albrecht *et al.* (2012), the force should scale with the suction pressure induced by the LEV and reach a maximum approximately when the LEV of maximal strength is shed from the plate, at which time the strongest suction is presumably generated; this hypothesis will be verified in §3.4. Because the LEV circulation increases roughly with the pitching frequency, as will be seen in §3.3, the force curves corresponding to f^*>0.09 may reveal distinct characters despite the qualitative similarity of the vorticity fields shown in figure

DISTRIBUTION A: Distribution approved for public release.

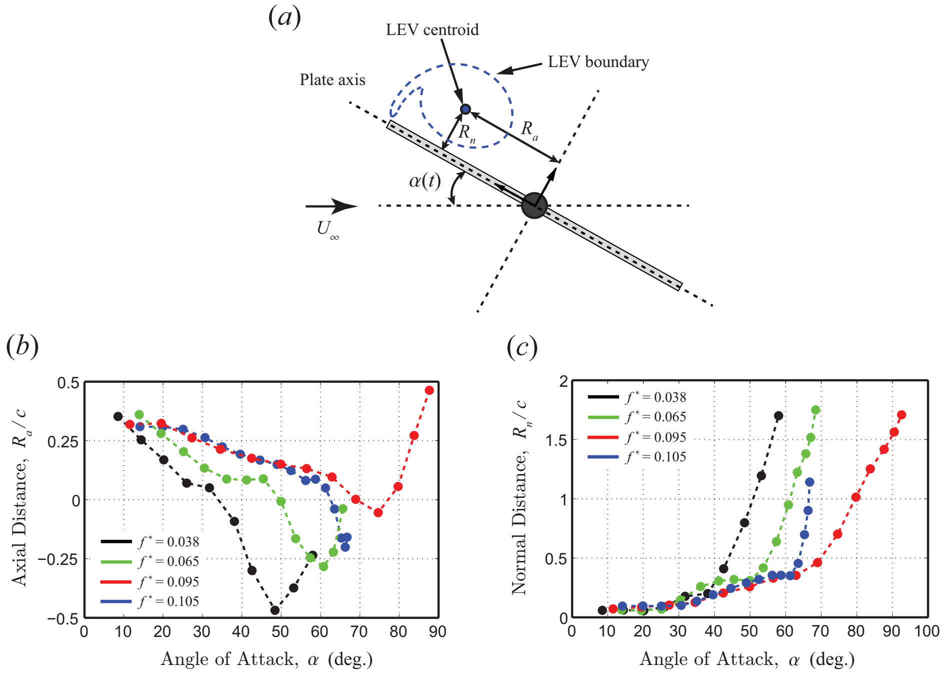

FIGURE 5. (a) Definition sketch of the vortex centroid with respect to the plate. R_a: axial distance between the LEV centroid and the pitch axis; R_n: shortest distance between the LEV centroid and the axis of the plate. (b) Evolution of R_a as a function of angle of attack. Different colours represent different reduced frequencies: black (f^*=0.038), green (f^*=0.065), red (f^*=0.095) and blue (f^*=0.105). (c) Evolution of R_n/c as a function of angle of attack. All experiments are performed at Re=9.9·10^4.

4(a). Interestingly, the measurements of Granlund *et al.* (2013) have shown that, for a flat plate executing a linear pitch-up manoeuvre from α=0 to 90° with the rotational axis placed at 3c/4, the force coefficient curves become similar for reduced pitch rates, defined as $K=\dot{\alpha}c/2U_\infty$, higher than 0.1. As discussed by the authors, this observation resonates with the unsteady aerofoil theory (Leishman 2000) which predicts that the effect of pitch rate on the lifting force becomes negligible if the pivot point is located at 3c/4.

To examine the details of the LEV dyanmics, the spatial location of the LEV centroid was tracked using the vortex identification technique described in §2. Figure 5(b) shows the evolution of the normalized axial distance, R_a/c, as a function of the angle of attack (refer to figure 5(a) for notation). For the lowest frequency case, the LEV centroid convects more than $c/2$ aft of the aerodynamic centre, $c/4$, during the course of the vortex growth phase. Snapshots of the corresponding spanwise vorticity fields exhibit salient features of the separated flow worth noting—streamwise elongation of the vortex core and early separation of the LEV (figure 4(a): top row). With increasing f^*, one observes that the vortex core becomes tighter and the vortex separation is delayed to a higher angle of attack. This effect is clearly illustrated in the two highest frequency cases (figure 4(a): bottom two rows; figure 5(b)), in which very tight and strong LEV cores drift no more than $c/5$ aft of the aerodynamic centre until the vortices separate at approximately $\alpha\approx60°$. This observation supports the notion that sufficient rotational acceleration (due to high pitching frequency) may contribute to the stability of LEVs on wings undergoing flapping manoeuvres, as suggested by Lentink & Dickinson (2009). It is important to note here that the qualitative similarity in the vortex dynamics between these two cases

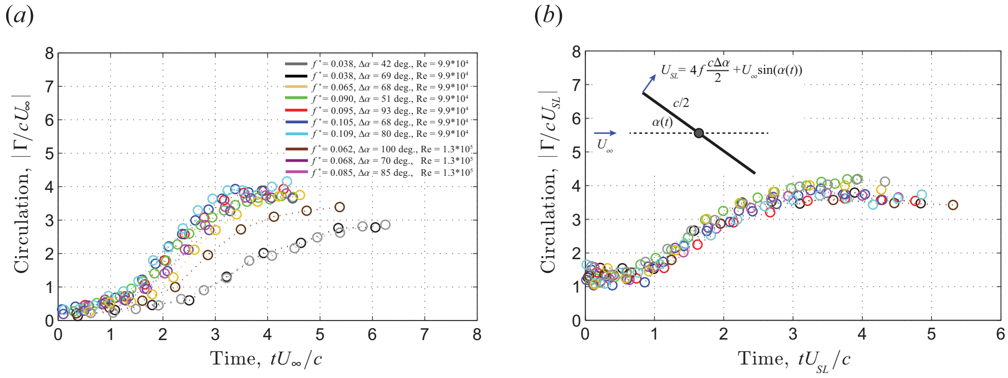

FIGURE 6. Temporal evolution of the LEV circulation for various motion profiles at two different Reynolds numbers. The circulation and time are scaled with (a) the free-stream velocity, U_∞ and (b) the shear-layer feeding velocity, U_{SL}.

(despite the large differences in f and $\Delta\alpha$) suggests that the proposed scaling of the pitching frequency is appropriate for the present problem (figure 4(a): bottom two rows). In addition, the velocity measurements over a range of operational conditions indicate that the LEV characteristics become quite similar when the variation in f^* is small.

Figure 5(c) illustrates the evolution of the normalized distance between the LEV centroid and the plate axis, R_n/c, as a function of the angle of attack. An approximate separation angle can be inferred from the figure where R_n/c starts to increase rapidly as a result of the advection of the LEV into the wake. An important observation, introduced earlier, is that the aerodynamic torque starts to decrease well before the vortex separates from the plate (figure 4a). In order to precisely explain this phenomenon, the relationship between the LEV formation and the accompanying aerodynamic torque will be examined in §3.4 using a potential flow model.

3.3. *Scaling of the leading-edge vortex growth*

In order to determine the scaling for the LEV formation time and strength, we calculate the spanwise circulation of the LEVs for various pitching profiles. The experiments are performed over a wide range of reduced frequencies (f^*=0.038 $\sim$ 0.11), amplitudes ($\Delta\alpha$=42 deg. $\sim$ 100 deg.) and at two different Reynolds numbers. Various LEV circulation histories are compared in figure 6(a), where the circulation and time are normalized using the free-stream velocity and chord. Here, t=0 corresponds to an instant when the plate starts to rise from the equilibrium angle, α=0. The circulation of the LEVs increases monotonically with the angle of attack and reaches a maximum approximately when the vortex lifts off from the plate surface. Subsequently the LEV circulation remains nearly constant as the vortex propagates downstream in the near wake. This is a manifestation of the fact that the circulation around a closed material contour moving with the fluid must remain constant with time (i.e, Kelvin's circulation theorem). Large variations in magnitude and temporal evolution of the LEV circulation are clearly evident, in particular between the low and high frequency cases, suggesting that the free-stream velocity and chord are not sufficient scaling parameters to characterize the LEV growth under a variety of conditions.

Provided that the vortex growth is dictated by the transport of circulation flux into the vortex core through the feeding shear-layer, as noted by Sattari *et al.* (2012), we explore the possibility of scaling the LEV growth rate and circulation using the characteristic shear-layer feeding velocity at the leading edge. As defined in figure 6(b), we approximate the shear-layer feeding velocity as the vector sum of the local velocity of the leading edge and the component of the free-stream in the direction of the plate motion: $U_{SL} = 4fc\mathit{\Delta}\alpha/2 + U_\infty \sin(\alpha(t))$. By construction, this definition ensures that the shear-layer feeding velocity is approximately aligned with the orientation of the shear layer at the leading edge. Figure 6(b) reveals a good collapse of circulation histories. The efficacy of using the shear-layer feeding velocity as a scaling parameter for the LEV growth and strength has been recently demonstrated by Kriegseis *et al.* (2013) for a rapidly accelerating flat plate undergoing plunging motions at a constant angle of attack. It is worthwhile to mention that the current non-dimensionalization of vortex circulation is analogous to how Dabiri (2009) defined the dimensionless optimal vortex formation number, $\hat{T}$. The premise of a universal formation number is that, for a given vortex generator, the maximum vortex strength is achieved at $\hat{T}{\approx}4$ when the vortex stops entraining additional circulation emanating from the shear layer. We further note that the values of $\max(\Gamma/cU_{SL})$ and corresponding dimensionless time, tU_{SL}/c, are all within a narrow range of 3.5 to 4, conforming very well with the concept of universal vortex formation time (Gharib *et al.* 1998; Milano & Gharib 2005; Dabiri & Gharib 2005; Ringuette *et al.* 2007). Because this scaling yields an approximately constant circulation value with variations in pitching amplitude, frequency, and Reynolds number, it provides a useful bound for predicting the angle of attack, for a given pitching frequency and flow velocity, at which a LEV of maximum circulation is generated. This offers useful insights as to how we can tailor the plate kinematics in order to prolong the LEV residence time, and to leverage the dynamic stall phenomenon to its fullest advantage.

3.4. *Potential flow model*

To clarify the connection between the vortex evolution and the resulting aerodynamic torque on the flat plate, a potential flow model with the addition of external vortices (LEV and TEV) is considered here. The complex potential function can be conveniently derived using the Joukowski transformation, i.e., $z = \zeta + a^2/\zeta$, so that the flat plate of chord c in the physical z-plane is mapped from a circle of radius $a{=}c/4$ in the virtual ζ-plane (Batchelor 2000). The Cartesian frame is defined with the x-axis oriented along the plate's chord and the origin located at the mid-chord point. By applying the circle theorem (Milne-Thomson 2011), an expression for the complex potential that models a stationary flat plate in the presence of a single leading-edge vortex of strength Γ_{LEV} located at ζ_{LEV} and a trailing-edge vortex of strength Γ_{TEV} located at ζ_{TEV} is given by:

$$w(\zeta) = \frac{\Gamma_{\text{LEV}}}{2\pi i} \ln\left(\frac{\zeta - \zeta_{\text{LEV}}}{\zeta - a^2/\zeta^*_{\text{LEV}}}\right) + \frac{\Gamma_{\text{TEV}}}{2\pi i} \ln\left(\frac{\zeta - \zeta_{\text{TEV}}}{\zeta - a^2/\zeta^*_{\text{TEV}}}\right) + \frac{\Gamma_0}{2\pi i}\ln(\zeta), \tag{3.1}$$

where values for Γ_{LEV}, ζ_{LEV}, Γ_{TEV}, and ζ_{TEV} are determined experimentally. In order to satisfy the no-penetration condition on the plate surface, image vortices with circulations $-\Gamma_{\text{LEV}}$ and $-\Gamma_{\text{TEV}}$ are placed at the inverse square points a^2/ζ^*_{LEV} and a^2/ζ^*_{TEV}, respectively. The circulation Γ_0 is placed at the centre of a circle in order to maintain the stagnation point at the trailing edge, whose value is determined by imposing the Kutta-condition, i.e., $dw/d\zeta|_{\zeta=a} = 0$. This term merely serves as a correction to regularize the flow at the rear edge, and it should be distinguished from the bound circulation of the flat plate in a real flow.

The aerodynamic force (per unit span) can be evaluated using the Blasius formula: $F_x - iF_y = \frac{1}{2} i\rho_f \oint_C (\frac{dw}{dz})^2 dz$ (Batchelor 2000), where the contour integration can be performed using the Cauchy residue theorem. The quasi-steady approach to force evaluation can be justified based on the fact that the force term proportional to the time derivative of circulation (i.e., $F \propto d\Gamma/dt$) violates a number of physical principles, as noted by Minotti (2002). For example, the author demonstrated that the temporal change in the bound circulation on a stationary cylinder would result in a finite force that violates isotropy in the two-dimensional plane. Analogously, in the case of a thin flat plate, a similar situation would result in a violation of reflection symmetry. Furthermore, the so-called added-mass effect is expected to play only a minor role, if any, in the force generation owing to the symmetry of rotational acceleration. For this reason, the added-mass term in the potential flow model vanishes naturally. The dependence of the aerodynamic loads on the pitch rate or unsteady wing velocity is indirectly reflected through the values of vortex location and intensity, where, in §3.2 and §3.3, the effects of wing velocity on these quantities are discussed in detail.

An explicit expression of the quasi-steady force imparted on the plate by the external vortices is given by:

$$\begin{aligned} F_x - iF_y = i\rho_f\Gamma_{\text{LEV}} \Bigg\{ & \frac{\zeta_{\text{LEV}}^2}{\zeta_{\text{LEV}}^2 - a^2} \Bigg(\frac{\Gamma_{\text{LEV}}}{2\pi i(\zeta_{\text{LEV}} - a^2/\zeta_{\text{LEV}}^*)} - \frac{\Gamma_{\text{TEV}}}{2\pi i(\zeta_{\text{LEV}} - \zeta_{\text{TEV}})} \\ & + \frac{\Gamma_{\text{TEV}}}{2\pi i(\zeta_{\text{LEV}} - a^2/\zeta_{\text{TEV}}^*)} - \frac{\Gamma_0}{2\pi i\zeta_{\text{LEV}}} \Bigg) + \frac{\Gamma_{\text{LEV}}}{2\pi i}\frac{\zeta_{\text{LEV}}a^2}{(\zeta_{\text{LEV}}^2 - a^2)^2} \Bigg\} \\ + i\rho_f\Gamma_{\text{TEV}} \Bigg\{ & \frac{\zeta_{\text{TEV}}^2}{\zeta_{\text{TEV}}^2 - a^2} \Bigg(\frac{\Gamma_{\text{TEV}}}{2\pi i(\zeta_{\text{TEV}} - a^2/\zeta_{\text{TEV}}^*)} - \frac{\Gamma_{\text{LEV}}}{2\pi i(\zeta_{\text{TEV}} - \zeta_{\text{LEV}})} \\ & + \frac{\Gamma_{\text{LEV}}}{2\pi i(\zeta_{\text{TEV}} - a^2/\zeta_{\text{LEV}}^*)} - \frac{\Gamma_0}{2\pi i\zeta_{\text{TEV}}} \Bigg) + \frac{\Gamma_{\text{TEV}}}{2\pi i}\frac{\zeta_{\text{TEV}}a^2}{(\zeta_{\text{TEV}}^2 - a^2)^2} \Bigg\}, \end{aligned} \tag{3.2}$$

where F_y represents the resultant (normal) force and the corresponding lift and drag are $F_y\cos(\alpha)$ and $F_y\sin(\alpha)$, respectively, which can be appropriately normalized by $0.5\rho_f U_\infty^2 c$. It is worthwhile to mention that the last term in each of the curly brackets captures what is known as Routh's correction (Clements 1973), which rectifies the velocity discrepancy between the mapping and physical planes at the location of the point vortex.

We employed the Bernoulli's equation to calculate the pressure distribution around the circle in the ζ-plane, which is subsequently integrated to determine the average location of the pressure variation (i.e., centre of pressure). The corresponding location on the flat plate in the physical z-plane is obtained via conformal mapping. The aerodynamic torque imparted by the vortex is determined by taking the product of the resultant force and the distance between the centre of pressure and the pitch axis. When the plate is immersed in a real flow, it is subject to an additional torque arising from the friction stress and the pressure accumulation on the front surface as the incoming fluid is slowed down and redirected to turn around the sharp edges. An estimate of this additional torque is obtained directly from the measured steady moment of the flat plate. Therefore, we approximate the *net* aerodynamic torque as the sum of the vortex torque deduced from the potential flow model and the steady moment of the flat plate.

To evaluate the accuracy of this formulation, we first consider a representative case (corresponding to f^*=0.095 in figures 4 $\sim$ 6) to examine how the vortex intensity and stability contribute to the generation of the aerodynamic torque on the plate. Despite a number of simplifications and assumptions, the aerodynamic torque evaluated based on the inviscid theory, when combined with the steady moment of the flat plate, compares remarkably well with that of the experimental measurement, as illustrated in figure 7(a). At large angles of attack, a significant portion of the aerodynamic torque is generated

DISTRIBUTION A: Distribution approved for public release.

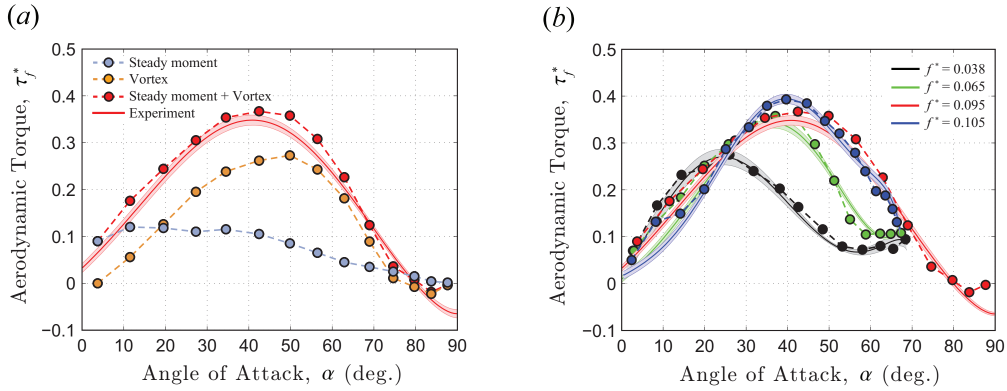

FIGURE 7. (a) A comparison of the aerodynamic torque predicted by the potential flow model with the experimental measurement for the case $f^* = 0.095$ shown in figures 4 $\sim$ 6. Contributions from the vortex torque and the steady moment are plotted separately. (b) Validation of the proposed model over a range of reduced frequencies (f^*=0.038 $\sim$ 0.11): predictions (solid circles) and experiments (solid curves).

due to the presence of a strong LEV in close proximity of the plate. The precipitous decrease in the aerodynamic torque prior to the vortex separation is attributed to the movement of the LEV core on the plate, which in turn brings the centre of pressure closer to the rotational axis. The current analysis suggests that the contribution of the TEV on the aerodynamic loads is relatively small due to the fact that its circulation is no more than 50% of the maximum LEV circulation and that the TEV formation takes place exclusively in the wake. However, it should be noted that the inclusion of the TEV in the potential flow model does seem to yield a better estimation of the centre of pressure, and hence improves the accuracy of the model at large angles of attack. When the LEV is very weak or has not yet developed at small angles (typically less than 15 deg.), the steady moment constitutes a dominant portion of the net aerodynamic torque acting on the plate.

In order to verify the validity of the model over a wide variety of flow conditions, figure 7(b) compares the aerodynamic torque predicted by the model with the experimental measurements corresponding to four sets of data described in §3.2. It can be seen that the net aerodynamic torque estimated using our formulation agrees extremely well with the empirical data across a range of reduced frequencies, suggesting that the superposition of the potential flow model (which estimates the torque induced exclusively by the external vortices) and the steady moment of the flat plate captures the essential features of the flow physics associated with the large-scale oscillations. The significance of the present result lies in that it validates the use of a quasi-steady formulation to characterize the unsteady aerodynamics of the flat plate undergoing large-scale oscillations. The two-dimensional representation of the vortex exploited in the model is justified presumably because the flow topology of the separated flow structure is largely two-dimensional, which is partly ensured in this study by the use of a high aspect ratio rectangular plate. We believe that the current model offers an appealing framework to help us not only elucidate a direct connection between the large amplitude oscillations and the properties of the accompanying large-scale vortical structures, but also aid in the development of a low-order point vortex model for the characterization of the unsteady aerodynamics of a wing.

4. Concluding remarks

By taking advantage of the cyber-physical experimental setup and synchronized PIV, we systematically investigated the formation time and strength of LEVs generated on a rapidly pitching plate. In this paper, we formulated the reduced frequency parameter based on the leading edge excursion during the pitch-up manoeuvre. The velocity measurements over a wide variety of flow conditions suggest that the global behaviour of the separated flow structures is strongly controlled by the reduced frequency for $f^* < 0.09$. Beyond this threshold, however, the LEV characteristics became progressively more independent of f^*, from which we concluded that the reduced frequency is not a sufficient scaling parameter to characterize the LEV evolution across a myriad of flow conditions.

We demonstrated that the LEV growth and circulation scale with the characteristic velocity of the feeding shear-layer over a range of reduced frequencies ($0.038 \sim 0.11$) and pitching amplitudes (42 deg. $\sim$ 100 deg.) at distinct Reynolds numbers. A connection between this scaling and the concept of universal vortex formation time was discussed, and we demonstrated that the scaled LEV circulation and time peak within a narrow band of 3.5 to 4, revealing an excellent agreement with the previous results reported by Gharib *et al.* (1998) and others.

To elucidate the connection between the dynamics of the separated flow structures and the resulting aerodynamic torque acting on the flat plate, we formulated a simple potential flow model with the addition of two-dimensional vortices. This model, when coupled with the steady moment of the flat plate, reproduced the measured aerodynamic torque remarkably well. Most importantly, we demonstrated that the precipitous decrease in the aerodynamic torque occurs before the point of LEV separation or the attainment of maximum vortex circulation due to the movement of the vortex core (or centre of pressure) towards the rotational axis.

In order to gain a deeper understanding of the LEV dynamics, an assessment of three-dimensional effects will be conducted in the future. On a different level, we will attempt to optimize the plate kinematics with the aim of prolonging the LEV residence time and augmenting the vortex strength by implementing appropriate structural nonlinearities in the system and exploring the effects of pivot location.

5. Acknowledgement

This research is funded by the Air Force Office for Scientific Research (AFOSR) grant number FA9550-12-1-0099, monitored by Dr. Douglas Smith.

REFERENCES

Adrian, R. J., Christensen, K. T. & Liu, Z. C 2000 Analysis and interpretation of instantaneous turbulent velocity fields. *Exp. Fluids* **29**, 275–290.

Albrecht, T., del Campo, V., Weier, T. & Gerbeth, G. 2012 16th international symposium on applications of laser techniques to fluid mechanics .

Amandolese, X., Michelin, S. & Choquel, M. 2013 Low speed flutter and limit cycle oscillations of a two-degree-of-freedom flat plate in a wind tunnel. *Journal of Fluids and Structures* **43**, 244–255.

Baik, Y., Bernal, L., Granlund, K. & Ol, M. 2012 Unsteady force generation and vortex dynamics of pitching and plunging aerofoils. *J. Fluid Mech.* **709**.

Batchelor, G. K. 2000 *An Introduction to Fluid Dynamics*. New York, NY: Cambridge University Press.

Buchholz, J. H. J., Green, M. A. & Smits, A. J. 2011 Scaling the circulation shed by a pitching panel. *J. Fluid Mech.* **688**, 591–601.

Clements, R. R. 1973 An inviscid model of two-dimensional vortex shedding. *J. Fluid Mech.* **57(2)**, 321–336.

Dabiri, J. O. 2009 Optimal vortex formation as a unifying principle in biological propulsion. *Ann Rev Fluid Mech* **41**, 17–33.

Dabiri, J. O. & Gharib, M. R. 2005 Starting flow through nozzles with temporally variable exit diameter. *J. Fluid Mech.* **538**.

DeVoria, A. C. & Ringuette, M. J. 2012 Vortex formation and saturation for low-aspect-ratio rotating flat-plate fins. *Exp. Fluids* **52**, 441–462.

Ellington, C. P. 1984 The aerodynamics of insect light i-vi. *Philos. Trans. R. Soc. Lond. B Biol. Sci.* **305**, 1–181.

Ellington, C. P., vandenBerg, C., Willmott, A.P. & Thomas, A. L. R. 1996 Leading-edge vortices in insect flight. *Nature* **384**, 626–630.

Gharib, M. R., E., E. Rambod & Shariff, K. 1998 A universal time scale for vortex ring formation. *J. Fluid Mech.* **360**, 121–140.

Graftieaux, L., Michard, M. & Grosjean, N. 2001 Combining piv, pod and vortex identification algorithms for the study of unsteady turbulent swirling flows. *Meas. Sci. Technol.* **12**, 1422–1429.

Granlund, K. O., Ol, M. V. & Bernal, L. P. 2013 Unsteady pitching flat plates. *J. Fluid Mech.* **733**, R5.1–13.

Gustafson, K. E. & Albert, J. 1991 *Vortex Methods and Vortex Motion*. Philadelphia, Pennsylvania: Society for Industrial and Applied Mathematics.

Hartloper, C. & Rival, D. E. 2013 Vortex development on pitching plates with lunate and truncate planforms. *J. Fluid Mech.* **732**, 332–344.

Hover, F., Miller, S. & Triantafyllou, M. S. 1997 Vortex-induced vibration of marine cables: experiments using force feedback. *J. of Fluids and Structures* **11**, 307–326.

Jantzen, R. T., Taira, K., Granlund, K. O. & Ol, M. V. 2014 Vortex dynamics around pitching plates. *Phys. Fluids* **26**, 053606.

Khalak, A. & Williamson, C. H. K. 1999 Motions, forces and mode transitions in vortex-induced vibrations at low mass-damping. *J. Fluids and Structures.* **13**, 813–851.

Kim, D. & Gharib, M. 2010 Experimental study of three-dimensional vortex structures in translating and rotating plates. *Exp. of Fluids* **49**, 329–339.

Kriegseis, J., Kinzel, M. & Rival, D. E. 2013 On the persistence of memory: do initial conditions impact vortex formation? *J. Fluid Mech.* **736**, 91–106.

Lee, J. & Bernitsas, M. 2011 High-damping, high-reynolds viv tests for energy harnessing using the vivace converter. *Ocean Engineering* **38**, 1697–1712.

Leishman, J. G. 2000 *Principles of helicopter aerodynamics*. Cambridge, New York: Cambridge University Press.

Lentink, D. & Dickinson, M. H. 2009 Biofluiddynamic scaling of flapping, spinning, and translating fins and wings. *J. Exp. Biol.* **212**.

Mackowski, A. W. & Williamson, C. H. K. 2013 An experimental investigation of vortex-induced vibration with nonlinear restoring forces. *Phys. Fluids* **25**, 087101.

McCroskey, W. J. 1982 Unsteady airfoils. *Annual Review of Fluid Mechanics* **14**, 285–311.

Milano, M. & Gharib, M. 2005 Uncovering the physics of flapping flat plates with artificial evolution. *J. Fluid Mech.* **534**, 403–409.

Milne-Thomson, L. M. 2011 *Theoretical Hydrodynamics*. 5th edition, Dover Publications.

Minotti, F. O. 2002 Unsteady two-dimensional theory of a flapping wing. *Physical Review E* **534**, 051907.

Ol, M. V., Altman, A., Eldredge, J., Garmann, D. & Lian, Y. 2010 R*é*sum*é* of the AIAA FDTC low reynolds number discussion groups canonical cases. *AIAA Paper* pp. 2010–1085.

Onoue, K., Song, A., Strom, B. & Breuer, K. 2015 Large amplitude flow-induced oscillations and energy harvesting using a cyber-physical pitching plate. *J. Fluids and Structures* **55** (http://dx.doi.org/10.1016/j.jfluidstructs.2015.03.004i), 262–275.

Ozen, C. A. & Rockwell, D. 2012 Three-dimensional vortex structure on a rotating wing. *J. Fluid Mech.* **707**, 541–550.

Peng, Z. & Zhu, Q. 2009 Energy harvesting through flow-induced oscillations of a foil. *Physics of Fluids* **21**, Issue 12.

POIREL, D. & MENDES, F. 2014 Experimental small-amplitude self-sustained pitch-heave oscillations at transitional reynolds numbers. *AIAA Journal* **52,(8)**, 2577–2596.

RAMESH, K., GOPALARATHNAM, A., EDWARDS, J. R., OL, M. V. & GRANLUND, K. 2013 An unsteady airfoil theory applied to pitching motions validated against experiment and computation. *Theor. Comput. Fluid Dyn.* **27 (6)**, 843–864.

RAMESH, K., MURUA, J. & GOPALARATHNAM, A. 2015 Limit-cycle oscillations in unsteady flows dominated by intermittent leading-edge vortex shedding. *J. Fluids and Structures* **55**, 84–105.

RINGUETTE, M. J., MILANO, M. & GHARIB, M. 2007 Role of tip vortex in the force generation of low-aspect-ratio normal flat plates. *J. Fluid Mech.* **581**, 453–468.

RIVAL, D., PRANGEMEIER, T. & TROPEA, C. 2009 The influence of airfoil kinematics on the formation of leading-edge vortices in bio-inspired flight. *Exp. Fluids* **46**, 823–833.

SATTARI, P., RIVAL, D. E., MARTINUZZI, R. J. & TROPEA, C. 2012 Growth and separation of a start-up vortex from a two dimensional shear layer. *Phys. Fluids* **24**, 107102.

SONG, A., TIAN, X., ISRAELI, E., GALVAO, R., BISHOP, K., SWARTZ, S. & BREUER, K. 2008 Aeromechanics of membrane wings with implications for animal flight. *AIAA Journal* **46**, 2096–2106.

YILMAZ, T. O. & ROCKWELL, D. 2012 Flow structures on finite-span wings due to pitch-up motion. *J. Fluid Mech.* **691**, 518–545.

YU, H. T. & BERNAL, L. P. 2013 Effect of pivot point on aerodynamic force and vortical structure of pitching flat plate wings. *AIAA Paper* pp. 2013–0792.

1.

1. Report Type

Final Report

Primary Contact E-mail
Contact email if there is a problem with the report.

kbreuer@brown.edu

Primary Contact Phone Number
Contact phone number if there is a problem with the report

401-863-2870

Organization / Institution name

Brown University

Grant/Contract Title
The full title of the funded effort.

Cyber-Physical systems to understand the dynamics of nonlinear aeroelastic systems for flexible MAVs and energy-harvesting applications.

Grant/Contract Number
AFOSR assigned control number. It must begin with "FA9550" or "F49620" or "FA2386".

FA9550-12-1-0099

Principal Investigator Name
The full name of the principal investigator on the grant or contract.

Kenneth S Breuer

Program Manager
The AFOSR Program Manager currently assigned to the award

Douglas Smith

Reporting Period Start Date

4/1/2012

Reporting Period End Date

9/30/2015

Abstract

We report on the approach taken and progress made during the three year research program. The goals of the program were to develop parallel experimental and theoretical approaches to study the dynamics of high-amplitude aeroelastic instabilities dominated by unsteady vortex shedding. Current approaches, both experimental and theoretical fall short in their abilities to simulate a wide range of operating conditions and to simulate them in a reasonable time- frame. We demonstrate the successful development of a cyper-physical experimental system, capable of close-to arbitrary definition of the structural characteristics of an aerodynamic structure (stiffness, damping and mass) and demonstrate a complex stability landscape and a complex, but universal vortex formation scaling. We also demonstrate how an asymptotic method based on classical boundary layer theory can be used to develop a feasible numerical model for the rapid simulation of these complex systems.

Distribution Statement
This is block 12 on the SF298 form.

Distribution A - Approved for Public Release

Explanation for Distribution Statement

If this is not approved for public release, please provide a short explanation. E.g., contains proprietary information.

SF298 Form

Please attach your SF298 form. A blank SF298 can be found here. Please do not password protect or secure the PDF The maximum file size for an SF298 is 50MB.

SF298 Cover Page.pdf

Upload the Report Document. File must be a PDF. Please do not password protect or secure the PDF . The maximum file size for the Report Document is 50MB.

AFOSR_Final_Report_complete.pdf

Upload a Report Document, if any. The maximum file size for the Report Document is 50MB.

Archival Publications (published) during reporting period:

K Onoue, A Song, BW Strom and KS Breuer. (2014). Cyber-physical energy har- vesting through flow-induced oscillations of a rectangular plate, in 32nd ASME Wind Energy Symposium. American Institute of Aeronautics and Astronautics.

K Onoue, A Song, B Strom and KS Breuer. (2015). Large amplitude flow-induced oscillations and energy harvesting using a cyber-physical pitching plate. Journal of Fluids and Structures 55, 262-275

Changes in research objectives (if any):

none

Change in AFOSR Program Manager, if any:

Extensions granted or milestones slipped, if any:

Extension was requested, but not awarded

AFOSR LRIR Number

LRIR Title

Reporting Period

Laboratory Task Manager

Program Officer

Research Objectives

Technical Summary

Funding Summary by Cost Category (by FY, $K)

	Starting FY	FY+1	FY+2
Salary			
Equipment/Facilities			
Supplies			
Total			

Report Document

Report Document - Text Analysis

Report Document - Text Analysis

Appendix Documents

2. Thank You

E-mail user

Sep 21, 2015 22:08:43 Success: Email Sent to: kbreuer@brown.edu